NOVEL ARCHITECTURES FOR HIGH-PERFORMANCE SUPERCAPACITORS BASED ON 2D MATERIALS

PhD Dissertation

Wonge Lisheshar IBRAHIM

Eskişehir 2025

NOVEL ARCHITECTURES FOR HIGH-PERFORMANCE SUPERCAPACITORS BASED ON 2D MATERIALS

Wonge Lisheshar IBRAHIM

PhD Dissertation

Department of Electrical and Electronic Engineering

Program in Electronic

Supervisor: Prof. Dr. Nihan KOSKU PERKGÖZ

Eskişehir

Eskişehir Technical University

Institute of Graduate Programs

January 2025

This thesis has been supported by the projects 22DRP292, TÜBİTAK: 118E996, 20AG025, 20AG001, 124E061 which are approved by the SRP Committee.

FINAL APPROVAL FOR THESIS

This thesis titled NOVEL ARCHITECTURES FOR HIGH-PERFORMANCE SUPERCAPACITORS BASED ON 2D MATERIALS has been prepared and submitted by Wonge Lisheshar IBRAHIM in partial fulfillment of the requirements in "Eskişehir Technical University Directive on Graduate Education and Examination" for the Degree of PhD in Electrical and Electronic Engineering Department has been examined and approved on 13/01/2025.

Committee Members		**Title, Name and Surname**	**Signature**
Member	:	Prof. Dr. Nihan KOSKU PERKGÖZ	
Member	:	Prof. Dr. Feridun AY	
Member	:	Prof. Dr. Gökhan ÇINAR	
Member	:	Asst. Prof. Dr. Umut SAVACI	
Member	:	Asst. Prof. Dr. Faruk DİRİSAĞLIK	

Prof. Dr. Semra KURAMA
Director of the Institute of Graduate Programs

13/01/2025

SUPERVISOR APPROVAL

PhD student Wonge Lisheshar IBRAHIM, whom I supervise, has completed this thesis titled NOVEL ARCHITECTURES FOR HIGH-PERFORMANCE SUPERCAPACITORS BASED ON 2D MATERIALS. According to my inspections, the work is scientifically and ethically appropriate for the student to the thesis defense exam.

Supervisor
Prof. Dr. Nihan KOSKU PERKGÖZ

ABSTRACT

NOVEL ARCHITECTURES FOR HIGH-PERFORMANCE SUPERCAPACITORS BASED ON 2D MATERIALS

Wonge Lisheshar IBRAHIM

Department of Electrical and Electronic Engineering

Program in Electronic

Eskişehir Technical University, Institute of Graduate Programs, January 2025

Supervisor: Prof. Dr. Nihan KOSKU PERKGÖZ

The growing demand for efficient energy storage systems in renewable energy and portable electronics highlights the need for advanced technologies. Supercapacitors, with their exceptional power density, rapid charge-discharge capabilities, and superior cycle stability, offer a promising solution but are limited by low energy density. This challenge underscores the transformative potential of 2D materials, such as graphene and MXenes, in bridging this gap. This dissertation investigates high-performance supercapacitors using 2D materials. Graphene-based supercapacitors, fabricated with rotationally stacked bilayer graphene synthesized via CVD, achieved a specific gravimetric capacitance (SGC) of up to 316 F g^{-1} with 100% retention after 10,000 cycles in Na_2SO_4 electrolyte. In addition, nonfunctionalized MXenes synthesized via CVD were studied with both aqueous and ionic liquid (IL) electrolytes. MXenes paired with [BMIM]BF_4 IL electrolyte achieved a specific energy density of 391 Wh kg^{-1}, more than twice the 144 Wh kg^{-1} achieved in aqueous electrolytes. A record SGC of 5160 F g^{-1} was also obtained using the LiTFSI-VC electrolyte, significantly surpassing most state-of-the-art supercapacitors but limited by stability challenges. Separator studies revealed that filter paper enhanced capacitance while Celgard improved cycle stability, emphasizing the importance of device configuration on performance. The comparative analysis suggests that graphene holds potential for long-term stability in portable electronics, while MXenes show promise for high-energy applications like renewable energy stabilization and rapid-charging systems in transportation. This work highlights the immense potential of 2D materials in advancing supercapacitor technologies, emphasizing the need for further research into material stability and electrolyte compatibility.

Keywords: Supercapacitors, 2D materials, Graphene, MXene, Ionic liquid electrolytes.

ÖZET

2B MALZEMELERE DAYALI YÜKSEK PERFORMANSLI SÜPERKAPASITÖRLER IÇIN YENILIKÇI MIMARILER

Wonge Lisheshar IBRAHIM

Elektrik Elektronik Mühendisliği Anabilim Dalı

Elektronik Bilim Dalı

Eskişehir Teknik Üniversitesi, Lisansüstü Eğitim Enstitüsü, Ocak 2025

Danışman: Prof. Dr. Nihan KOSKU PERKGÖZ

Yenilenebilir enerji ve taşınabilir elektronikte verimli enerji depolama sistemlerine yönelik artan talep, ileri teknolojilere olan ihtiyacı vurgulamaktadır. Olağanüstü güç yoğunlukları, hızlı şarj-deşarj yetenekleri ve üstün çevrim kararlılıkları ile süper kapasitörler, umut verici bir çözüm sunar, ancak düşük enerji yoğunluğu ile sınırlıdır. Bu zorluk, grafen ve MXene'ler gibi 2B malzemelerin bu boşluğu doldurmadaki dönüştürücü potansiyelini vurguluyor. Bu tez, 2B malzemeler kullanarak yüksek performanslı süper kapasitörleri araştırıyor. Kimyasal buhar biriktirme (KBB) yoluyla sentezlenen rotasyonel olarak yığılmış çift katmanlı grafen ile üretilen grafen bazlı süper kapasitörler, Na_2SO_4 elektrolitte 10.000 döngüden sonra %100 tutma ile 316 F g^{-1}'ye kadar özgül bir gravimetrik kapasitans (ÖGK) elde etti. Ek olarak, KBB yoluyla sentezlenen işlevselleştirilmemiş MXene'ler, hem sulu hem de iyonik sıvı (İS) elektrolitlerle incelenmiştir. [BMIM]BF_4 İS elektroliti ile eşleştirilen MXene'ler, sulu elektrolitlerde elde edilen 144 Wh kg^{-1}'nin iki katından fazla olan 391 Wh kg^{-1}'lik bir özgül enerji yoğunluğuna ulaştı. LiTFSI-VC elektroliti kullanılarak 5160 F g^{-1}'lik bir rekor ÖGK elde edildi, bu da son teknoloji süper kapasitörlerin çoğunu önemli ölçüde geride bıraktı, ancak kararlılık zorluklarıyla sınırlandı. Separatör çalışmaları, filtre kağıdının kapasitansı artırdığını, Celgard'ın ise döngü stabilitesini iyileştirdiğini ortaya koyarak cihaz konfigürasyonunun performans üzerindeki önemini vurguladı. Karşılaştırmalı analiz, grafenin taşınabilir elektroniklerde uzun vadeli stabilite potansiyeline sahip olduğunu, MXene'lerin ise yenilenebilir enerji stabilizasyonu ve ulaşımda hızlı şarj sistemleri gibi yüksek enerjili uygulamalar için umut vaat ettiğini gösteriyor. Bu çalışma, 2B malzemelerin gelişmiş süper kapasitör teknolojilerindeki muazzam potansiyelini vurgulayarak, malzeme stabilitesi ve elektrolit uyumluluğu konusunda daha fazla araştırmaya duyulan ihtiyacı ortaya koymaktadır.

Anahtar Sözcükler: Süper kapasitörler, 2B malzemeler, Grafen, MXene, İyonik sıvı elektrolitler.

ACKNOWLEDGEMENTS

It is my pleasure to express my most sincere gratitude to Prof. Dr. Nihan KOSKU PERGÖZ, and Prof. Dr. Feridun AY, for their continuous guidance, motivation, moral support, and assistance during this research. I am indebted to them for their efforts and enthusiasm throughout the research period.

I would like to thank the members of my thesis committee: Prof. Dr. Gökhan ÇINAR, Asst. Prof. Dr. Umut SAVACI, and Asst. Prof. Dr. Faruk DIRISAĞLIK for reading and commenting on the thesis.

I would like to thank our current and former members of MIDAS, including Hüseyin ŞAR, Merve ÖPER, Jihad AWARD, Çağatay Nail ŞENGÖR, Dr. Sina ROUHI, Asst. Prof. Dr. Mehmet BAY, Safiye YÜCEL, Mustafa Yiğit ESEN, etc., for providing a working environment that is enjoyable, warm, friendly, and filled with motivation.

I want to thank Prof. Dr. Servet TURAN, for providing the measuring equipment without which this work would not have been possible. I also want to acknowledge all the Seramik processing lab members for their help, support, friendship and collaborative spirit.

I am indebted to my dearest mother, Amshatu KONGNYUY for her continuous support, care, and encouragement.

Wonge Lisheshar IBRAHIM

13/01/2025

STATEMENT OF COMPLIANCE WITH ETHICAL PRINCIPLES AND RULES

I hereby truthfully declare that this thesis is an original work prepared by me; that I have behaved in accordance with the scientific ethical principles and rules throughout the stages of preparation, data collection, analysis, and presentation of my work; that I have cited the sources of all the data and information that could be obtained within the scope of this study, and included these sources in the references section; and that this study has been scanned for plagiarism with "scientific plagiarism detection program" used by Eskişehir Technical University, and that "it does not have any plagiarism" whatsoever. I also declare that, if a case contrary to my declaration is detected in my work at any time, I hereby express my consent to all the ethical and legal consequences that are involved.

Wonge Lisheshar IBRAHIM

CONTENTS

Page

LIST OF TABLES

Page

LIST OF FIGURES

Page

LIST OF IMAGES

Page

GLOSSARY OF SYMBOLS AND ABBREVIATIONS

EDLC	:	Electrochemical double-layer capacitor
2D material	:	Two-dimensional material
MXene	:	A family of 2D transition metal carbides, nitrides, and carbonitrides
TMD	:	Transition metal dichalcogenide
SAC	:	Specific area capacitance
SGC	:	Specific gravimetric capacitance
SVC	:	Specific volumetric capacitance
SED	:	Specific energy density
CE	:	Coulombic efficiency
SPD	:	Specific power density
CVD	:	Chemical vapor deposition
KBB	:	Kimyasal buhar biriktirme
GCD	:	Galvanostatic charge-discharge
EIS	:	Electrochemical impedance spectroscopy
CV	:	Cyclic voltammetry
LSV	:	Linear sweep voltammetry
PAT	:	Photoresist assisted transfer
PAT-graphene	:	Graphene transferred using the PAT method
PPAT	:	PMMA/PDMS assisted transfer
PMMA	:	Polymethyl methacrylate
PDMS	:	Polydimethylsiloxane
IPA	:	Isopropyl alcohol
PET	:	Polyethylene terephthalate
IL	:	Ionic liquid
$[BMIM]BF_4$	:	1-butyl-3-methyl-imidazolium tetrafluoroborate
AN	:	Acetonitrile
STFSI	:	Triethyl sulfonium bis (trifluoromethyl sulfonyl) imide
VC	:	Vinyl
LiTFSI	:	Lithium Bis(Trifluoromethanesulfonyl)Imide
WIS	:	Water in salt

SEM	:	Scanning electron microscope
XRD	:	X-ray diffraction
EDS	:	Energy dispersive spectroscopy
XPS	:	X-ray photoelectron spectroscopy
AFM	:	Atomic force microscopy
CPE	:	Constant phase element
ESR	:	Equivalent series resistance
CS	:	Celgard separator
LGPS	:	Laboratory-grade paper separator
LT-MXene	:	MXenes grown at 1080 °C
MT-MXene	:	MXenes grown at 1120 °C
HT-MXene	:	MXenes grown at 1150 °C

1. INTRODUCTION

According to Our World in Data [1], mankind has experienced a significant evolution over the last few centuries, largely driven by technological advancements that have transformed energy access and consumption. The relentless pursuit of knowledge and innovation has led to the discovery and exploitation of a wide array of energy sources, including fossil fuels, hydropower, nuclear energy, and an increasing emphasis on renewable technologies. This shift towards renewables has become particularly crucial considering the current global warming crisis, which has underscored the environmental repercussions of fossil fuel dependency. As a result, renewable energy technologies, such as solar, wind, and hydroelectric systems, have gained considerable traction as viable alternatives [2,3].

However, the integration of these renewable sources into the energy grid presents a formidable challenge due to the inherent intermittency of solar and wind energy production, which fluctuates with environmental conditions [4,5]. This intermittency necessitates the development of robust energy storage solutions capable of ensuring a continuous energy supply, even during periods of low renewable generation, such as nighttime or calamitous weather events. The escalating demand for effective energy storage systems has catalyzed the innovation and refinement of various storage technologies, which can be broadly categorized into mechanical, electrochemical, chemical, electrical, and thermal energy systems [2,6,7].

Among these diverse technologies, electrochemical systems have emerged as some of the most prominent and extensively researched energy storage solutions. Figure 1.1 [8] provides a comparative analysis of these electrochemical systems in terms of their specific energy and power density-critical metrics that define their operational efficiency and suitability for specific applications. Specific energy pertains to the total energy a device can store per unit area, volume, or mass, while power density indicates the rate at which energy can be released. Notably, as illustrated in Figure 1.1, conventional capacitors exhibit impressive power density yet possess limited energy storage capabilities. Conversely, batteries and fuel cells, while less proficient in power density, excel in energy capacity. Supercapacitors present a unique middle ground, combining moderate energy storage with rapid charge and discharge capabilities, undergoing tens of thousands of cycles with minimal degradation in performance. Although Figure 1.1 highlights just four storage technologies, a comprehensive comparison can be found in

the reviews by Koohi-Fayegh et al. [6], as well as Hall et al. [8], among others. This expansive body of research not only reinforces the importance of energy storage technologies but also paves the way for advancements that will be pivotal in transitioning to a sustainable energy future.

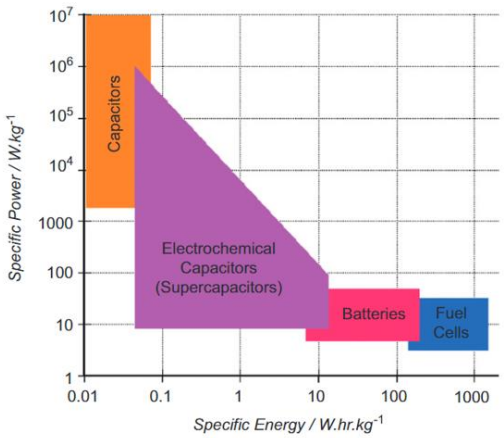

Figure 1.1. *The Ragon curve for energy storage systems (Hall P. 2008).*

1.1. Supercapacitors

A supercapacitor is an energy storage device that stores energy through charge accumulation at the interface between its electrodes and the electrolyte. A simple sandwich supercapacitor constitutes two electrodes sandwiching an electrolyte-soaked separator as shown in Figure 1.2 [9]. The electrode is usually made up of an energy storage material, plastered onto a metallic current collector. The amount of energy that can be stored by a supercapacitor can be calculated using Equation 1.1, where C is its capacitance, and V is the operation potential. Theoretically, the most effective way to improve a supercapacitor's energy density is by expanding its operating potential window. However, this approach is often constrained by the breakdown voltage of the electrolyte. For example, aqueous electrolytes typically have a breakdown voltage slightly above 1 V, whereas ionic liquids can achieve a wider operating potential window of up to 4 V [10,11]. Despite the efficiency of increasing the voltage window, research has largely focused on enhancing capacitance through the development of high-surface-area materials and micromachining techniques. This preference stems from the challenges associated with finding stable electrolytes that can sustain high voltages without degradation. By contrast, increasing capacitance through surface area optimization offers a more accessible and reliable path to improving energy density, as it leverages

advancements in materials science and microfabrication to create electrodes with significantly larger charge storage capabilities.

Supercapacitors are emerging as promising energy storage technology. This is because of the following unique characteristics that make them stand out in the field of energy storage:

i. High power density: Supercapacitors can deliver rapid bursts of energy due to their ability to charge and discharge quickly. This makes them ideal for applications requiring sudden power surges, such as regenerative braking in electric vehicles.

ii. Cycle stability: Unlike traditional batteries, supercapacitors exhibit excellent cycle stability. They can endure many charge-discharge cycles without significant degradation.

iii. Environmentally friendly: Supercapacitors do not rely on toxic materials as some batteries do. Their environmentally friendly nature is a significant advantage.

iv. Energy density trade-off: While supercapacitors excel in power density, their energy density (the amount of energy stored per unit mass or volume) tends to be lower than that of lithium-ion batteries. This limitation has spurred extensive research to enhance supercapacitor energy densities.

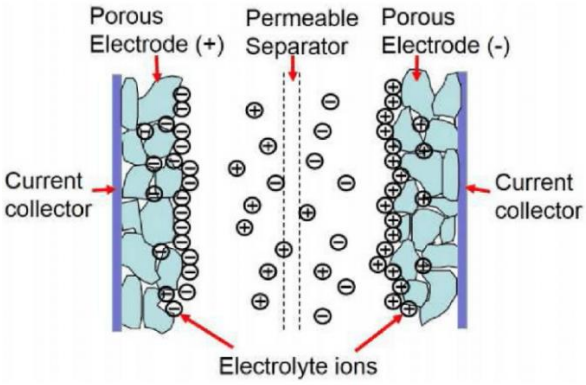

Figure 1.2. *The cross-section of a simple supercapacitor cell (Drummond R. 2019).*

$$E = \frac{1}{2}CV^2 \tag{1.1}$$

1.1.1. Types of supercapacitors

Depending on the mechanism of energy storage or cell configuration, supercapacitors can be classified into three types, electrochemical double-layer capacitors (EDLC), pseudo capacitors, and hybrid supercapacitors.

1.1.1.1. Electrochemical double-layer capacitors (EDLC)

EDLCs store energy via electrostatic adsorption of electrolyte ions on or within the electrode materials upon application of a potential difference, which is then released when connected to a load causing electricity to flow [12]. They use high specific-surface area nanoporous materials (e.g., activated carbon with a specific surface area of 1000 $m^2 g^{-1}$ [13], which can go as high as 3164 $m^2 g^{-1}$ [14]) as active electrode materials, resulting in a much higher capacitance than conventional capacitors. Another salient feature of EDLCs is their durability; they can operate for tens of thousands of charge-discharge cycles, or even millions of cycles, without compromising their initial capacity [15]. Nanoporous carbon materials are the most popular option for EDLC electrodes owing to their high surface area, electrical conductivity, electrochemical stability, availability, existing industrial production, and comparatively low cost [16,17].

1.1.1.2. Pseudo capacitors

Pseudo capacitors on the other hand store energy via electrosorption, intercalation, and fast and reversible redox reactions. These processes allow pseudo-capacitors to store more energy than EDLCs [15]. This high capacity, however, comes with trade-offs, including reduced cycle stability and lower power density. Over time, the reversible redox reactions become increasingly irreversible with each cycle, while the lower conductivity of most pseudo-active materials further limits their power density. Pseudo-capacitor electrodes are usually constructed with active materials such as conducting polymers, metal oxides, as well as occasionally functionalized porous carbons [16].

1.1.1.3. Hybrid supercapacitors

Finally, hybrid capacitors are composed of an EDLC electrode and a pseudocapacitive or battery-type electrode, synergizing the properties of both systems and leading to an increased energy density and cycling stability. Because of the two electrodes, hybrid supercapacitors can store energy through both fast redox and

adsorption processes occurring in the electrodes [12]. Hybrid supercapacitors, which use both faradic and non-faradic charge storage methods, have better power densities than pseudo-capacitors and can store more energy than EDLCs while still being more affordable [15]. There are three different types of hybrid supercapacitors, distinguishable by their electrode design: asymmetric, composite, and battery type.

Asymmetric hybrid supercapacitors store charge by non-faradic methods as well as faradic processes, doping, and un-doping. This broadens the voltage window of the device in addition to increasing the specific capacitance. Most asymmetric supercapacitors use a pseudo-capacitor material as the cathode because creating an efficient negatively charged pseudo-active material is challenging. This difficulty, often seen with conductive polymers, arises from issues like the high resistance encountered during n-doping. [15,18]. Additionally, low equivalent series resistance and cycle stability provided by EDLC material enhance total power density. An example of an asymmetric hybrid setup is demonstrated by Mastragostino et al., where an 80% p-doped poly(3-methyl thiophene) serves as the anode and a 90% activated carbon as the cathode [19,20].

A composite hybrid supercapacitor combines two or more materials into a single electrode, integrating both physical and chemical charge storage processes to mitigate the individual shortcomings of each material. By leveraging the fast charging and discharging capabilities and high conductivity of EDLC materials, alongside the high surface area and redox activity of pseudo-capacitive materials, composite supercapacitors offer enhanced performance [15]. For instance, carbon nanotube/polymer composites (e.g., polyaniline or polypyrrole) exhibit superior electrical, mechanical, and electrochemical properties compared to polymers alone [21,22].

A battery-type hybrid supercapacitor is formed by replacing one of the supercapacitor's electrodes with a battery electrode, leading to a notable increase in energy capacity. This unique configuration represents a specialized form of asymmetric hybrid supercapacitor. Studies in this area have shown that battery-type hybrids effectively bridge the performance gap between batteries and supercapacitors by combining the high energy density of batteries with the superior power density, fast charging capability, extended cycle life, and excellent reversibility of supercapacitors [23]. For instance, pairing an electric double-layer capacitor (EDLC) electrode with a battery-type electrode creates a battery-type hybrid. A notable example is the use of the high-voltage intercalation compound $LiNi_{0.5}Mn_{1.5}O_4$ as the positive electrode in a hybrid

configuration with activated carbon as the negative electrode, yielding a capacity of 25 mAh g^{-1} with 80% retention after 1000 cycles [24]. Alternatively, a battery electrode combined with a pseudo-active material can be employed in such setups. For example, an organic electrolyte-based system featuring an alluaudite $Na_2Fe_2(SO_4)_3$ cathode and Ti_2C-MXene nanosheet anode achieves an impressive specific energy of 260 Wh kg^{-1} [24].

While advancements in supercapacitor configurations have significantly improved performance, achieving the desired balance of high energy density, power density, and long-term stability remains a challenge. Addressing these limitations necessitates the development of advanced electrode materials with exceptional properties. Materials that offer high surface area, superior conductivity, and the ability to support fast ion-transport are essential for pushing the boundaries of current supercapacitor technologies. In this context, 2D materials have emerged as promising candidates. Their unique structural and electrochemical characteristics have the potential to meet these demands, making them a focal point for next-generation energy storage systems.

1.1.2. 2D materials as supercapacitor electrodes

Since the successful exfoliation of graphene in 2004 [25], which marked the beginning of the era of 2D materials, their exceptional properties have continued to attract significant research interest across a wide range of applications, including energy storage, optoelectronics, and sensing [26,27]. With their intrinsically high surface area and unique electrochemical properties, 2D materials have been extensively studied, as evidenced in several reviews [27–30]. Among the most promising 2D materials for energy storage applications are graphene, transition metal dichalcogenides (TMDs), and MXenes, each offering distinct advantages for advancing the performance of next-generation energy storage systems.

1.1.2.1. Graphene

Graphene has attracted a lot of attention for its potential in supercapacitor applications. This is due to its naturally high and adjustable surface area of approximately 2675 $m^2\ g^{-1}$, which can result in a specific area capacitance (SAC) of about 21 to 28 µF cm^{-2} (about 550 F g^{-1}) if fully utilized [31–33]. Graphene is also highly conductive to electricity, with a carrier mobility of 200,000 $cm^2\ v^{-1}\ s^{-1}$ at an electron density of around

2 x 10^{11} cm^{-2} [34], which makes it capable of increasing the power density of supercapacitors. Additionally, graphene exhibits high mechanical strength, with a Young's Modulus of approximately 1 TPa [35], making it ideal for flexible energy storage systems. This exceptional strength also enables the assembly of graphene into free-standing films with excellent mechanical stability. Because graphene is chemically stable [33,36], it can be utilized with a variety of electrolytes without worry of the active material deteriorating, extending the life of the supercapacitor.

1.1.2.2. MXenes

MXenes have piqued the interest of scientists due to their amazing properties, which include their innate conductivity, rich surface chemistry, superior hydrophilicity, and layered structure [37,38]. Nonfunctionalized Mo_2C demonstrates a high quantum capacitance of 3.2 mF cm^{-2}, as calculated using density functional theory [39]. Considering a crystal thickness of 0.36 nm [40], this translates to a remarkable gravimetric capacitance of 9816 F g^{-1}, showcasing its remarkable potential for supercapacitor applications.

1.1.3. Application of supercapacitors

Supercapacitors, with their unique ability to deliver high power density and rapid charge-discharge cycles, are increasingly being integrated into diverse applications across multiple industries.

- Consumer Electronics

  Supercapacitors are utilized in portable devices like smartphones, MP3 players, tablets, and wearable gadgets, providing efficient energy storage for quick charging and extended battery life [41,42]. A demonstration of such a wearable system made possible by flexible supercapacitors is presented in Image 1.2.

Image 1.1. *A demonstration of a wearable supercapacitor-powered gadget, (Zhang, 2021)*

- Transportation

  Supercapacitors play a pivotal role in modern transportation, powering electric vehicles (EVs), hybrid buses, and trains [43]. They are also used in regenerative braking systems and to stabilize energy in wind turbines. An example of a hybrid system with a supercapacitor-integrated regenerative braking system is shown in Image 1.2 [44].

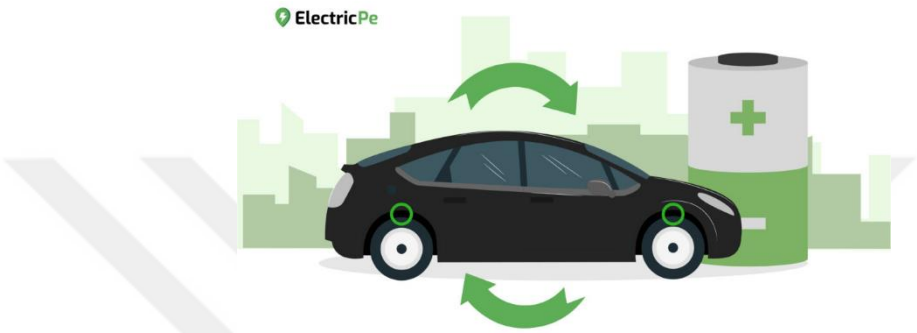

Image 1.2. *A hybrid electric vehicle with a supercapacitor integrated regenerative braking system, (ElectricPe, 2023)*

- Power Backup

  Supercapacitors are employed for power backup in uninterruptible power supplies (UPS) [45] as shown in Image 1.3 and to complement batteries, extending their lifetime by managing high-power demands.

Image 1.3. *A supercapacitor-based uninterruptible power supply (Bicker Elektronik GmbH, n.d.)*

- Biomedical

  Applications in the biomedical field include powering wearable health monitors, implantable sensors, and portable medical devices, ensuring reliability and safety [46–48].

Image 1.4. *An example of a micro supercapacitor-powered healthcare monitoring system, (Lu, 2019)*

- Military and Aerospace

In military and aerospace systems, supercapacitors are used for energy storage in drones, missiles, and satellites, offering high reliability under extreme conditions [49,50]. Image 1.5 presents some examples of supercapacitor-integrated military devices.

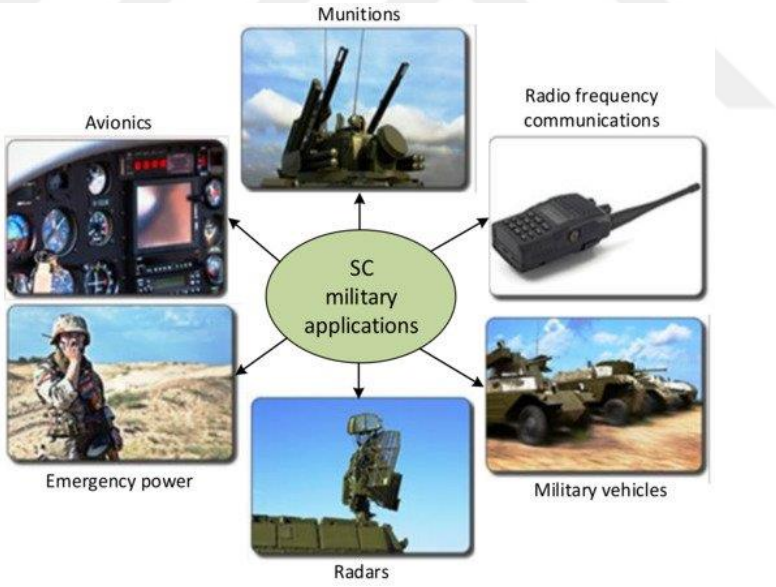

Image 1.5. *Supercapacitor-integrated defense equipment, (Şahin, 2022)*

1.2. Organization of the Dissertation

This dissertation is structured into five chapters, each addressing critical aspects of the research on supercapacitors utilizing graphene and MXene-based electrodes with various electrolytes. The chapters are designed to ensure a logical progression from fundamental concepts to experimental findings and broader implications.

Chapter 1: Introduction

This chapter provides the motivation and context for the research, highlighting the need for advanced energy storage technologies. It discusses the advantages of supercapacitors, the challenges of improving their energy density, and the role of 2D materials, such as graphene and MXenes, in addressing these limitations.

Chapter 2: Graphene-Based Supercapacitors

This chapter explores the synthesis, characterization, and application of graphene as a supercapacitor electrode material.

- Section 2.1 discusses graphene synthesis techniques, including chemical vapor deposition (CVD), and methods for transferring graphene onto various substrates.
- Section 2.2 examines the structural and electrochemical characterization of graphene, emphasizing its relevance to energy storage applications.
- Section 2.3 details the fabrication and performance evaluation of graphene-based supercapacitors in aqueous electrolytes, incorporating techniques such as cyclic voltammetry (CV), galvanostatic charge-discharge (GCD), and electrochemical impedance spectroscopy (EIS).

Chapter 3: MXenes: The 2D Marvels

This chapter investigates MXenes as supercapacitor electrode materials, focusing on their performance in various electrolyte configurations.

- Section 3.1 introduces MXenes, describing their synthesis techniques, structural properties, and suitability for energy storage.
- Section 3.2 outlines the synthesis and characterization of Mo_2C MXenes via CVD.
- Section 3.3 examines the performance of MXenes in aqueous electrolytes, exploring the effects of separator type, mass loading, and electrode coverage.
- Section 3.4 analyzes the behavior of MXenes in ionic liquid electrolytes, such as [BMIM]BF_4, STFSI, and LiTFSI-VC systems, while evaluating the impact of different separators on device performance.

Chapter 4: Comparative Analysis and Discussion

This chapter compares the performance of graphene- and MXene-based supercapacitors, highlighting their respective strengths, challenges, and factors influencing their efficiency.

- Section 4.1 summarizes the key findings from Chapters 2 and 3, including metrics such as specific capacitance, energy density, and stability.
- Section 4.2 contrasts the performance of graphene and MXenes in aqueous and ionic liquid electrolytes, focusing on voltage windows, cycle life, and material stability.
- Section 4.3 discusses the role of device configurations, including separator selection and electrode architecture, in optimizing performance.
- Section 4.4 examines material and device-level trends, emphasizing the impact of electrode materials, electrolyte types, and device configurations on energy density, power density, and stability.
- Section 4.5 highlights challenges encountered during the research and proposes solutions and future research directions.
- Section 4.6 explores the broader implications of the findings, focusing on their potential applications in the energy storage field, portable electronics, and renewable energy systems.
- Section 4.7 provides a summary of comparative insights, highlighting the complementary nature of graphene and MXenes for diverse supercapacitor applications.
- Section 4.8 concludes the chapter with a synthesis of key observations and their implications for supercapacitor technologies.

Chapter 5: Conclusion and Future Perspectives

The final chapter summarizes the overall contributions of the research, emphasizing the potential of graphene and MXenes in advancing supercapacitor technologies. It also proposes future research directions, including the development of novel 2D materials, enhanced stability, and improved electrolyte compatibility for scalable energy storage solutions.

2. GRAPHENE-BASED SUPERCAPACITORS

Due to its extraordinary qualities, graphene, an extraordinary material made up of one layer of closely spaced all-sp^2-hybridized carbon atoms organized in a hexagonal or benzene-ring shape as shown in Figure 2.1, has attracted a lot of attention [51]. Graphene was first effectively exfoliated by Novoselov and associates, [52] opening the door for a wide range of uses in different industries. Supercapacitors' energy storage is one such exciting use and those properties of graphene that have drawn in researchers in this field include:

1. Surface area and charge storage of graphene: The surface area of a single sheet of graphene can be adjusted to a maximum of 2675 $m^2\ g^{-1}$. This enormous surface could store charge with a specific areal capacitance (SAC) of 21 to 28 $\mu F\ cm^{-2}$ [53,54], or roughly 550 Fg^{-1} [51] specific gravimetric capacitance (SGC), if it were fully exploited. Graphene is a fantastic material for energy storage because of its huge surface area, which allows it to absorb a lot of ions.
2. Enhancement of power density and conductivity: At an electron density of 2 x $10^{11}\ cm^{-2}$, graphene has a remarkable carrier mobility of 200,000 $cm^2\ V^{-1}\ s^{-1}$ [55].
3. Mechanical strength and flexibility: Graphene has exceptional mechanical strength, with a Young's Modulus of 1 TPa [56]. Because of its adaptability, it may be integrated into flexible energy storage systems, which makes it appropriate for uses where durability and adaptability are crucial.
4. Chemical stability and durability: The chemical stability of graphene makes it compatible with a wide range of electrolytes [51,57]. Graphene-based supercapacitors have a longer lifespan because graphene does not degrade as some other active materials do.

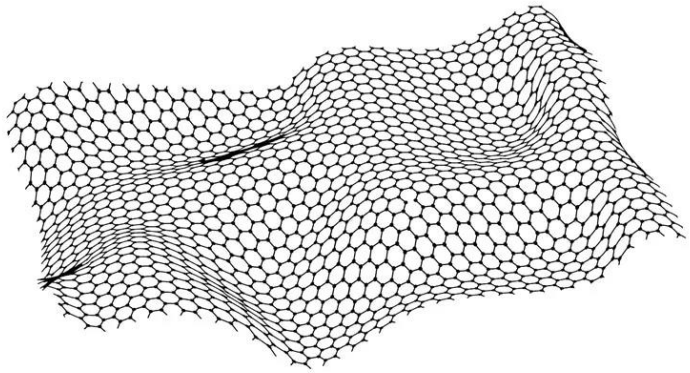

Figure 2.1. *Crystal structure of graphene*

Despite these properties, graphene layers tend to aggregate during growth or application because of van der Waals forces and inter-planar π-π interfacial contact. Lower capacitance values than expected are the result of this aggregation, which prevents the electrolyte ions from intercalating [51]. Agglomeration has, therefore, impeded efforts to fully realize graphene's potential for supercapacitors, despite its numerous benefits. In conclusion, graphene has great potential for supercapacitor applications, however overcoming agglomeration issues is still necessary to realize this material's full potential.

Building on the foundational principles of energy storage and the critical role of 2D materials, this chapter focuses on graphene, a material with exceptional promise for high-performance supercapacitors. The synthesis of graphene through chemical vapor deposition (CVD) is explored, followed by the fabrication of multilayer, rotationally stacked graphene to enhance its intrinsic properties. This rotationally stacked graphene is thoroughly characterized using Raman spectroscopy and atomic force microscopy (AFM), ensuring a detailed understanding of its structural features. The material is then utilized to fabricate supercapacitor electrodes, which are rigorously tested to address challenges related to energy density and stability. Comprehensive electrochemical performance analyses, including galvanostatic charge-discharge (GCD), electrochemical impedance spectroscopy (EIS), and cyclic voltammetry (CV), are conducted to evaluate the potential of these graphene-based supercapacitors for advanced energy storage applications.

2.1. Synthesis and Characterization of Graphene

Understanding the synthesis of graphene is fundamental to tailoring its properties for various applications. The synthesis methods directly influence the structural and electronic characteristics of the material, which in turn affect its performance in supercapacitors and other energy storage devices. In this section, we first explore the various synthesis approaches used to obtain high-quality graphene, followed by a discussion on the techniques used to characterize the synthesized material.

2.1.1. Synthesis

Graphene can be synthesized through a variety of methods, broadly classified into two main categories: top-down and bottom-up. The bottom-up approach involves constructing the desired material from smaller atomic or nanoscale building blocks. This

method typically relies on the chemical reactions of molecular precursors to form covalently bonded two-dimensional networks. In contrast, the top-down approach begins with a bulk material, which is systematically broken down into nanoscale structures, like a subtractive process [58–60]. A classic example of the top-down approach is the production of graphene from its bulk precursor, graphite, achieved through successive exfoliation of its top layers [61,62].

Chemical and mechanical exfoliation are examples of top-down techniques, while chemical vapor deposition and epitaxial growth are examples of bottom-up techniques. The top-down method of producing graphene by mechanical exfoliation of graphite, plus the discovery that graphene can be seen under an optical microscope when placed on top of a Si wafer with an appropriately chosen thickness of SiO_2 was crucial to the global graphene fever that began in 2004 [52]. Chemical vapor deposition (CVD) and epitaxial growth are two bottom-up techniques that can yield high-quality, large-area graphene films with minimal flaws. The most widely used top-down method for producing graphene involves exfoliating graphite oxide, which is obtained by the chemical oxidation of graphite [59].

In this chapter, the CVD technique is employed to synthesize graphene, as earlier studies [63] have demonstrated its ability to produce high-quality graphene with high throughput. Figure 2.2 illustrates a horizontal tube split-furnace setup used for graphene growth on copper substrates. The process begins by ramping the furnace to a growth temperature of 1035 °C under a hydrogen flow of 100 sccm and a pressure of approximately 1.1 Torr. During the growth phase, which lasts between two and a half to five minutes, methane gas (40 sccm), the carbon precursor is introduced onto the copper surface. These precursors undergo catalytic decomposition and self-assembly, resulting in the formation of graphene monolayers. After the growth phase, the methane flow is stopped, the heating is turned off, and the furnace lid is opened to facilitate rapid cooling. This direct growth method offers key advantages, including simplicity, scalability, and cost-effectiveness.

When grown on Cu substrates, graphene can be used directly to create electrodes for supercapacitors. Regrettably, the copper substrate is delicate and prone to mechanical deformation, including twisting or wrinkling, because of annealing during synthesis. Because of this, depending on the intended use, it would need to be transferred to different substrates altogether. Two techniques were used in this study to transfer the as-grown

graphene to the target substrates (Si/SiO_2 and Ti/Au): photoresist assisted transfer (PAT) and polymethyl methacrylate (PMMA)/ polydimethylsiloxane (PDMS) assisted transfer (PPAT).

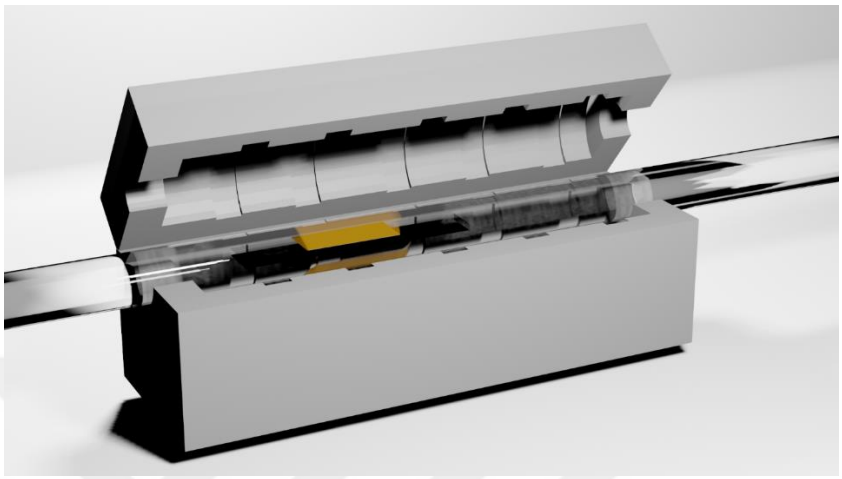

Figure 2.2. *CVD setup used for the synthesis of graphene.*

2.1.1.1. Photoresist-assisted transfer (PAT) method

Figure 2.3 illustrates the process flow of the PAT technique employed to transfer samples grown on Cu substrates. The transfer process involves several distinct stages:

1. **Sample preparation:**

   The first step involves preparing the samples by cutting them into the desired shapes. A layer of photoresist is then applied to the sample surface to provide support during the transfer process. To solidify the photoresist, the sample is baked at 70°C for at least 12 hours.

2. **Etching and film formation:**

   Next, the prepared sample is immersed in a $FeCl_3$ etchant solution to dissolve the underlying Cu substrate. This step results in the formation of a thin graphene-photoresist film. The film is then carefully rinsed with deionized (DI) water to remove any residual etchant, followed by drying with nitrogen (N_2).

3. **Film handling and placement:**

   The fragile graphene-photoresist film is delicately handled to prevent breakage and is gently placed onto the target substrate. Common substrates include Au/Ti, SiO_2, or other desired materials, depending on the intended application.

4. **Adhesion and final steps:**

To ensure strong adhesion between the graphene-photoresist film and the target substrate, the assembly is baked on a hotplate at 70°C for 15 minutes. After adhesion is achieved, the sample is immersed in acetone to dissolve the photoresist layer, leaving behind a clean graphene layer on the new substrate. The final cleaning step involves rinsing the substrate with acetone and isopropyl alcohol (IPA) and drying it with N_2. This process yields a pristine graphene layer on the target substrate, ready for further use or characterization.

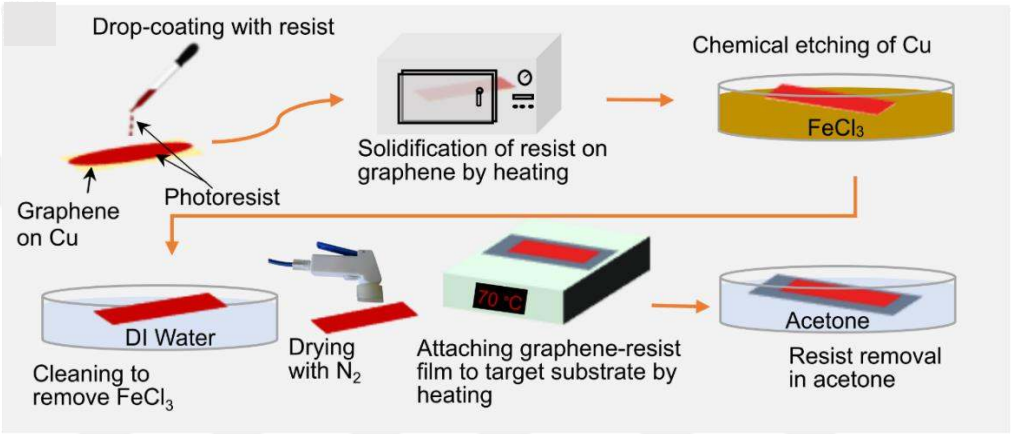

Figure 2.3. *Process flow of the photoresist-assisted transfer method (Ibrahim, 2022)*

2.1.1.2. The PMMA/PDMS assisted transfer (PPAT) method

The PPA method, developed by Suk, et, al. [64], is a method of transferring graphene to arbitrary substrates. In this method, PMMA and PDMS serve as sacrificial layers. Figure 2.4 shows the process flow of this transfer technique, which has been slightly tailored to suit our CVD-grown graphene. This process can be broken down into the following steps.

1. **Sample Preparation:**

Initially, the samples to be transferred are cut into desired shapes. These samples are then prepared for spin coating with PMMA. Since the Cu substrate on which graphene grows tends to twist during spin coating, a support layer is introduced. This is done by laminating the sample with polyethylene terephthalate (PET).

2. **PMMA coating:**

The graphene/copper foil is spun with a PMMA layer.

3. **Sample preparation for etching:**

A PDMS (polydimethylsiloxane) block is attached to the composite. PDMS provides support to the PMMA film, making it easier to handle after metal removal. After this PET is removed to expose the metallic substrate, which can then be etched away.

4. Metal etching:

Next, the copper is etched using a solution of $FeCl_3$, leaving behind only the PDMS/PMMA/graphene block.

5. Composite Cleaning:

The composite is cleaned in DI water and dried with nitrogen (N_2).

6. Application to Target Substrate:

The PDMS/PMMA/graphene composite is then applied to the desired substrate. The composite undergoes heat treatment at 200°C, a temperature higher than the transition temperature of PMMA. This step ensures complete contact between the wavy and rough PMMA/graphene film and the target substrate. Some pressure will inevitably need to be applied to help the composite adhere to the new substrate because it does not do so easily. This results in fissures on the transferred graphene.

7. PMMA removal:

After ensuring PMMA adherence to the new substrate, the PDMS is carefully removed, leaving only the PMMA and graphene. Finally, the PMMA is dissolved in acetone and further annealed at 350°C under a 200 Tors Argon/Hydrogen atmosphere for 2 hours.

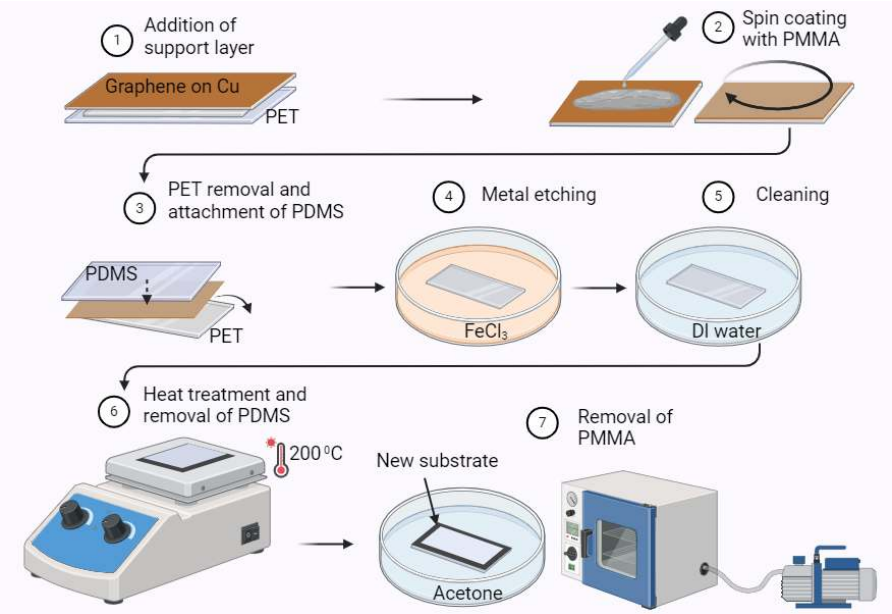

Figure 2.4. *Process flow of the PMMA/PDMS-Assisted Transfer (PPAT) method.*

After implementing the PAT and PPAT methods, the resulting graphene samples were examined, with optical images presented in Figure 2.5. As shown in Figure 2.5(a), the PAT method produces a continuous graphene film on the Si/SiO_2 substrate. In contrast, the PPAT method, as illustrated in Figure 2.5(b), achieves a cleaner transfer but introduces numerous cracks in the graphene. These cracks are attributed to the pressure applied during the attachment of the PMMA layer to the target substrate.

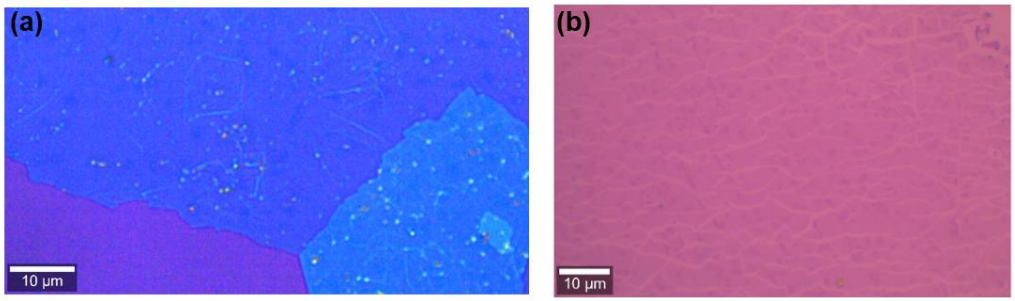

Figure 2.5. *Close-ups of graphene transferred to Si/SiO_2 substrates using: (a) PAT, and (b) PPAT techniques.*

Each of the two approaches to transferring graphene has benefits and drawbacks, and the best option will depend on the desired results. A comparison of the two methods for graphene transfer to arbitrary substrates is presented in Table 2.1.

Table 2.1. *Comparison of the PAT, and the PPAT methods.*

PAT method	PPAT method
Minimal or no fracturing and continuity of the transferred graphene film.	Cracking of the graphene film into multiple microfilms, resulting in a noncontinuous structure.
Easy removal of photoresist removal using acetone only.	The photoresist is only completely removable through 2 hours of annealing in an argon/ hydrogen atmosphere.
Lengthy overall transfer duration (>24 hours).	Relatively shorter duration (<24 hours).
The resist/graphene film is fragile and should be handled carefully	PMMA film is supported by PDMS.
The process is easy and straight to the point.	Relatively more complex procedure.
Broad and intense Raman D band, indicating a high defect density in the transferred sample.	Smaller Raman D band, indicating a lower defect density in the transferred sample.

2.2. Characterization of Graphene

Figures 2.6 show the Raman spectra of graphene that was transferred onto a 300 nm SiO_2 on Si substrates using both PAT and PPAT methods. The spectra were recorded using a WITEC Raman instrument with a 532 nm laser excitation set to 1 mW power. The Raman spectrum of graphene transferred using the PAT method (PAT-graphene), shown in Figure 2.6(a), exhibits a disorder-induced D peak at 1362 cm^{-1}, a G band at 1596 cm^{-1}, a D# band at 2453 cm^{-1}, and a 2D (G') band at 2693 cm^{-1}. In contrast, the Raman spectrum of graphene obtained using the PPAT method (PPAT-graphene), presented in Figure 2.6(b), shows the D, G, D#, and 2D Raman modes at 1347 cm^{-1}, 1592 cm^{-1}, 2452 cm^{-1}, and 2681 cm^{-1}, respectively. These results are in close agreement with previous research [65]. The 2D/G peak intensity ratios (PIRs) for the PAT and PPAT graphene samples were calculated as 1.31 and 1.01, respectively. These ratios, which fall between 1 and 2, along with a 2D band FWHM of 46.1 cm^{-1}, suggest the presence of bilayer graphene, consistent with previous studies [66].

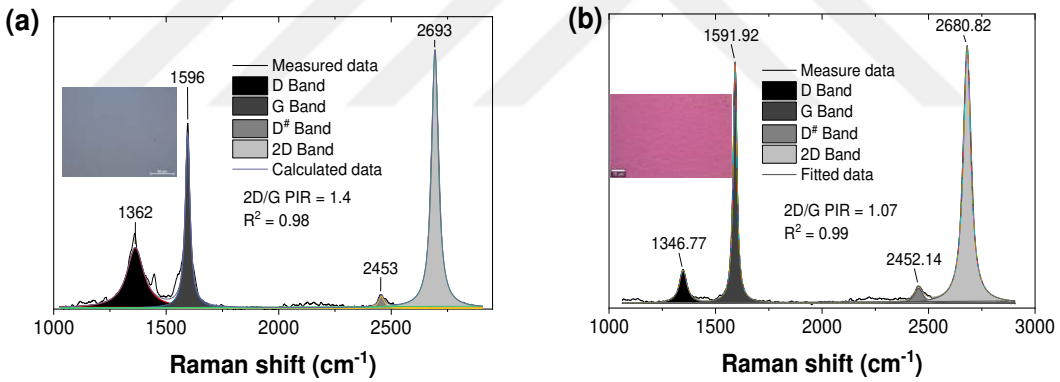

Figure 2.6. *The Raman spectra of the graphene films transferred to Si/SiO_2 substrates using the (a) PAT, and (b) PPAT methods.*

In addition to the Raman analysis, the samples were further characterized using AFM, with the results shown in Figure 2.7, providing additional insights into their morphology. The thickness of our samples, as assessed by line profiles formed on AFM images of several samples, ranged from 1.8 nm to 6 nm, with an average thickness of 3.2 nm. Figures 2.7 (a-b) show the AFM results of PAT and PPAT-graphene samples from which thicknesses of 3.32 and 2.7 nm respectively, were profiled. Although these results deviate from theoretical predictions (i.e., 0.335 nm for monolayer and 0.81 nm for bilayer graphene [67,68]), they do agree with experimental findings. Research has demonstrated

that AFM is unreliable for detecting graphene thickness, particularly for single-layer graphene, with reported values ranging from 0.4 to 1.7 nm, which differs significantly from the value (0.335 nm) published in the literature [69]. This is especially true for CVD graphene, where air bubbles or water molecules get caught between the graphene and the substrate during transfer, making accurate thickness measurement difficult. Figure 2.7(c) shows the 3D AFM image of PAT-graphene with an average roughness of 1.8 nm which is greater than 0.81 nm (the thickness of bilayer graphene), thus leading to inaccurate measurements.

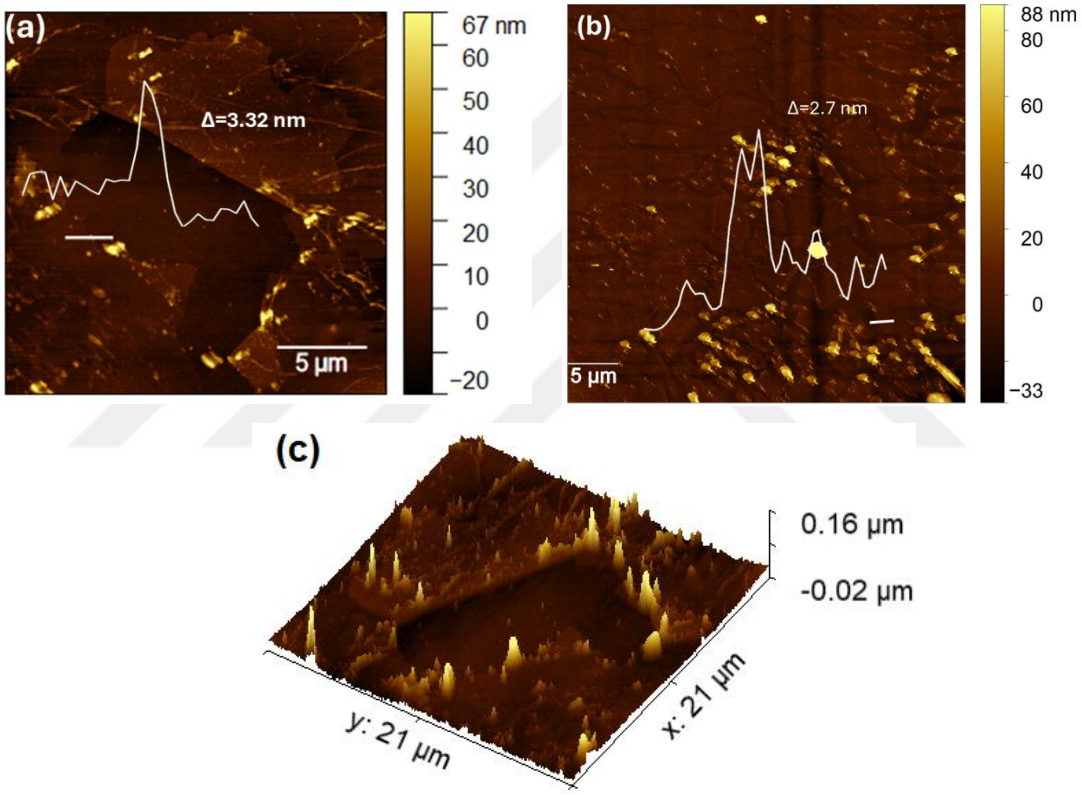

Figure 2.7. *AFM analysis results of graphene grown on Cu substrates and transferred onto Si/SiO_2 substrates using: (a) PAT, (b) PPAT techniques, and (c) the 3D AFM view of PAT graphene.*

After confirming through Raman and AFM analysis that the material synthesized by CVD is bilayer graphene, multiple layers of graphene were formed by repeatedly stacking bilayer graphene using the PAT method. This approach was intended to increase the active surface area for use as supercapacitor electrodes and to investigate the effects of agglomeration. The stacked samples were subsequently analyzed using Raman spectroscopy, with the results shown in Figure 2.8. As the number of layers increased, both the G and 2D bands exhibited blue shifts (Figure 2.8(a)). The 2D/G PIR increased

with the number of layers. This is contradictory to previously reported results [70,71], where the 2D/G PIR of multiple-layer graphene fell as the number of layers increased. The 2D band underwent an upshift, explaining the increase in the 2D/G PIR with the increase in the number of layers. This upshift in the 2D band is an indication of separation (decoupling) according to previous studies [64]. After intensity normalization and baseline subtraction, the Raman spectra of the stacked layers of graphene are almost identical as seen in Figure 2.8(b), indicating that the increase in the 2D/G PIR is largely due to suspension. This increase in 2D/G PIR of the decoupled layers of graphene is a consequence of the etalon effect in the 300 nm SiO_2 cavity and a decrease in doping due to the decoupling of graphene from the substrate or the lower layer. Therefore, the Raman spectra of the graphene samples demonstrate near-intrinsic properties of graphene with a doping concentration less than $1x\ 10^{12}$ cm^2, a strain less than 0.01%, and low disorder as observed by Suk, J.W., et al. [64].

We analyzed Raman spatial maps of three distinct samples—comprising 2-, 4-, and 6-layer graphene—shown in Figures 2.8 (c-e) respectively, to investigate the interactions between the layers and their ability to remain suspended without collapsing. The spatial maps, which illustrate the distribution of the 2D/G PIR within at least a 100 square micron area, revealed no significant differences between the samples, except for a broader range in the 2D/G PIR. Darker regions in the maps, where the 2D/G PIR approached zero, correspond to areas where the graphene layers are coupled, indicating direct contact and serving as connection points between adjacent sheets.

Three-dimensional AFM, shown in Figure 2.7 (c), revealed intriguing structural features such as nanopillars protruding from the graphene surface. These nanopillars likely play a key role in maintaining suspension, acting as structural hinges that physically link the bottom and top graphene layers. They can be thought of as microscopic bridges that prevent complete detachment of the layers. Between these nanopillars, the layers remain suspended or decoupled, preserving their structural integrity while preventing agglomeration. These findings corroborate the Raman spatial map results, with random black dots suggesting areas of decoupled graphene.

This behavior has significant implications for the use of such graphene structures as active materials in supercapacitors. Reducing layer agglomeration offers several advantages:

- **Improved ion intercalation:** Decoupled layers provide greater accessibility for ions, facilitating their movement and enhancing charge storage capacity.
- **Enhanced stability:** The structural integrity provided by the nanopillars prevents layer collapse over time, ensuring the device's long-term reliability.
- **Increased efficiency:** By minimizing energy losses during charge and discharge cycles, decoupled layers optimize the overall performance of the supercapacitor.

In conclusion, the strategic decoupling of graphene layers, supported by structural features such as nanopillars, unlocks immense potential for energy storage applications. Whether in supercapacitors or other advanced technologies, understanding and leveraging these subtle interlayer interactions provide exciting opportunities to push the boundaries of material performance and innovation.

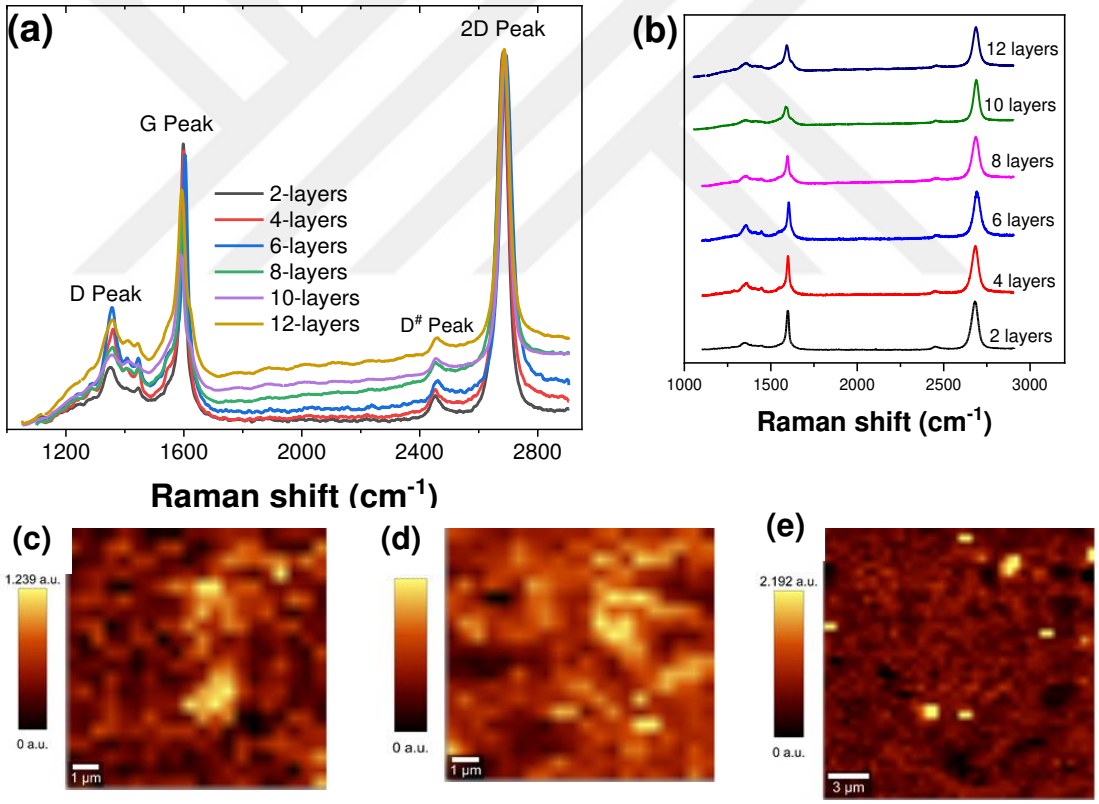

Figure 2.8. *Raman analysis of stacked graphene layers: (a, b) Raman spectra of 2- to 12-layer graphene, with (a) plotted on the same axes and (b) intensity-normalized (0–1) and cascaded. (c-e) 2D/G peak intensity ratio (PIR) spatial maps for 2-, 4-, and 6-layer graphene.*

2.3. Graphene-Based Supercapacitors

2.3.1. Device fabrication

After analyzing the structural properties of the graphene through detailed Raman and AFM analysis, the next step involved translating this graphene into functional supercapacitors. The supercapacitors were fabricated starting with lamella glass, which served as the support substrate. Lamella glass was chosen because it is both cost-effective and provides the necessary support for the titanium (Ti)/gold (Au) layer, which would otherwise lack structural integrity. The lamella glass was first cleaned using acetone, IPA, and DI water. A 10 nm thick layer of titanium was then deposited onto the glass substrate using a NANOVAK thermal evaporator. The Ti layer served as an adhesive layer, bonding the glass to a subsequent 90 nm gold layer.

The graphene was then transferred onto the Au/Ti current collector in the next phase. Given the ease of transfer and the continuity of the resulting graphene layer, the PAT approach was adopted for this step. Following the successful transfer, the devices were ready to be assembled into the structure shown in Figure 2.9. The assembly process involved sandwiching an electrolyte-soaked separator between two electrodes and integrating the components as illustrated in the diagram. Finally, the assembled devices were coated in PET to prevent the electrolyte from evaporating during testing.

After analyzing the structural properties of the graphene using Raman and AFM techniques, the next step was to integrate the graphene into functional supercapacitors. The supercapacitors were fabricated starting with lamella glass, chosen as the support substrate for its cost-effectiveness and ability to provide the necessary support for the Ti/Au layer, which would otherwise lack structural integrity. The lamella glass substrate was first cleaned using acetone, isopropyl alcohol (IPA), and deionized (DI) water. A 10 nm thick layer of titanium was then deposited onto the cleaned glass substrate using a NANOVAK thermal evaporator. This titanium layer acted as an adhesive interface, promoting strong bonding between the glass substrate and the subsequent 90 nm thick gold layer, which was also deposited using the same thermal evaporation technique. The gold layer served as the current collector for the supercapacitor electrodes.

The next phase involved the transfer of graphene onto the gold/titanium (Au/Ti) current collector. To achieve a continuous and high-quality graphene layer with minimal defects, the PAT method was chosen due to its reliability and ease of transfer. This

allowed the graphene to be seamlessly transferred onto the Au/Ti current collector, ensuring uniform coverage across the electrode surface. Once the graphene was successfully transferred, the electrodes were ready to be assembled into supercapacitor devices.

The device assembly was performed by sandwiching an electrolyte-soaked separator between the two graphene-coated electrodes, creating a structure like the one illustrated in Figure 2.9. The electrolyte and separator used were 1M Na_2SO_4 and laboratory-grade paper respectively. To prevent the electrolyte from evaporating during testing, the assembled devices were sealed and coated with a protective PET layer. This encapsulation ensured the stability of the electrolyte, allowing for reliable performance during electrochemical testing.

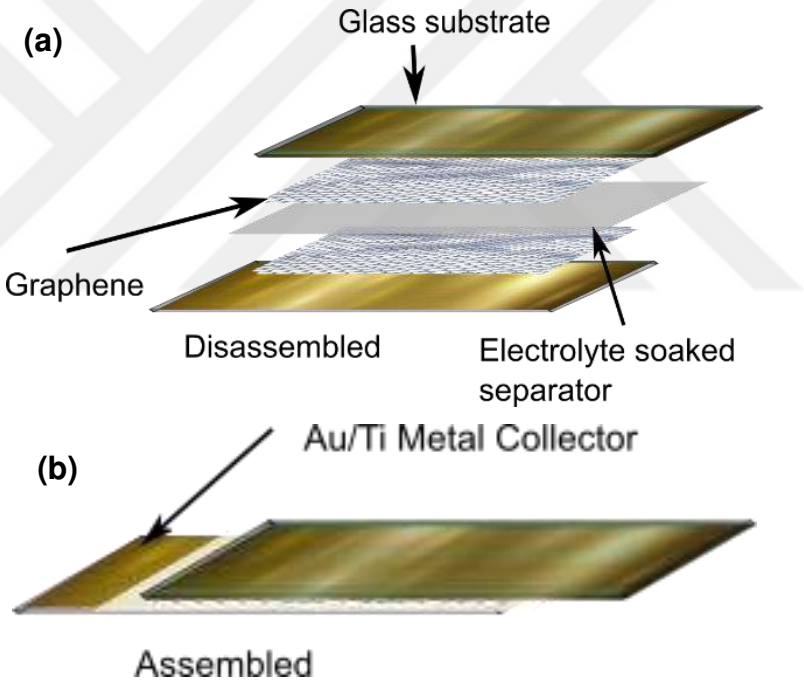

Figure 2.9. *Schematic representation of the graphene-based supercapacitor: (a) Individual components prior to assembly and (b) the completed symmetric sandwich supercapacitor.*

2.3.2. Device characterization and capacitance calculation

The performance of the supercapacitors was assessed using a GAMRY potentiostat/ galvanostat. We used cyclic voltammetry (CV), electrochemical impedance spectroscopy (EIS), and galvanostatic charge-discharge (GCD) studies to determine the capacitance, durability, and internal resistance of the supercapacitors.

Capacitances can be calculated from the CV using equation 2.1 according to prior studies [72,73], where S is the area between the CV curve, υ the scan rate, and V is the operation potential window of the device. The multiplier, 2, is added to compensate for the double-layer capacitance since the electrodes are symmetric. The area S is considered from the part of the CV which is as rectangular as possible as is illustrated in Figure 2.10.

$$C = \frac{2\int_{V_1}^{V_2} i\,dV}{v|V_2 - V_1|} = \frac{2S}{vV} \tag{2.1}$$

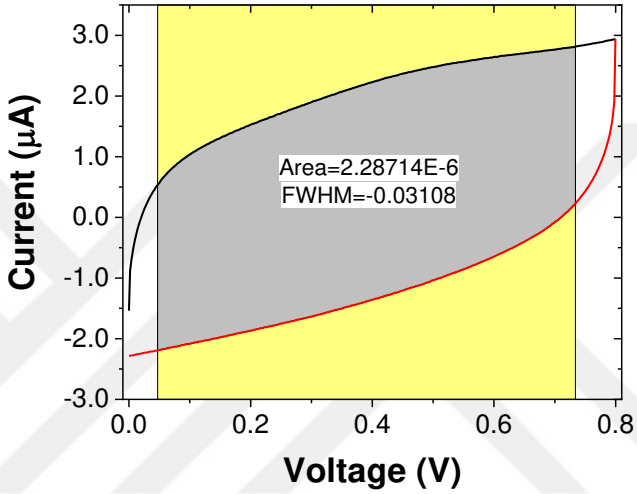

Figure 2.10. *Demonstration of capacitance calculation based on the area enclosed by the CV curve.*

2.3.3. Results and discussion

To investigate the performance of graphene as supercapacitor electrodes in Na_2SO_4 electrolyte, electrodes with varying numbers of graphene layers were fabricated by repeatedly transferring bilayer graphene onto Au/Ti current collectors. The electrochemical performance of these devices assessed through CV analysis are presented in Figure 2.11. CV measurements were conducted at scan rates ranging from 1 to 500 mV s^{-1}, without a specific increment pattern, to evaluate the rate stability of the supercapacitors.

The CV curves of the supercapacitors, based on 2-, 4-, and 8-layer graphene electrodes, are predominantly rectangular across various scan rates, as shown in Figures 2.11 (a-c). This rectangular shape is characteristic of electrochemical double-layer capacitor (EDLC) behavior, suggesting that charge storage primarily occurs through the electrostatic adsorption of ions at the electrode-electrolyte interface, with minimal pseudocapacitive contribution, closely aligning with previous findings [74,75].

The specific areal capacitance (SAC) for the device with a bilayer graphene electrode, calculated using Equation 2.1, was found to be 43.9 F cm^{-2} at a scan rate of 1 mV s^{-1}. This corresponds to a specific gravimetric capacitance (SGC) of 239.3 F g^{-1} and a specific volumetric capacitance (SVC) of 542.4 F cm^{-3}. To better understand the rate-dependent behavior, a logarithmic plot of SAC against scan rate is shown in Figure 2.11 (d) for different graphene-based devices. The devices with 2-, 4-, and 8-layer graphene electrodes exhibited rate stabilities of 9.1%, 6.3%, and 6.3%, respectively, indicating that the devices with fewer layers maintained a higher proportion of capacitance at higher scan rates.

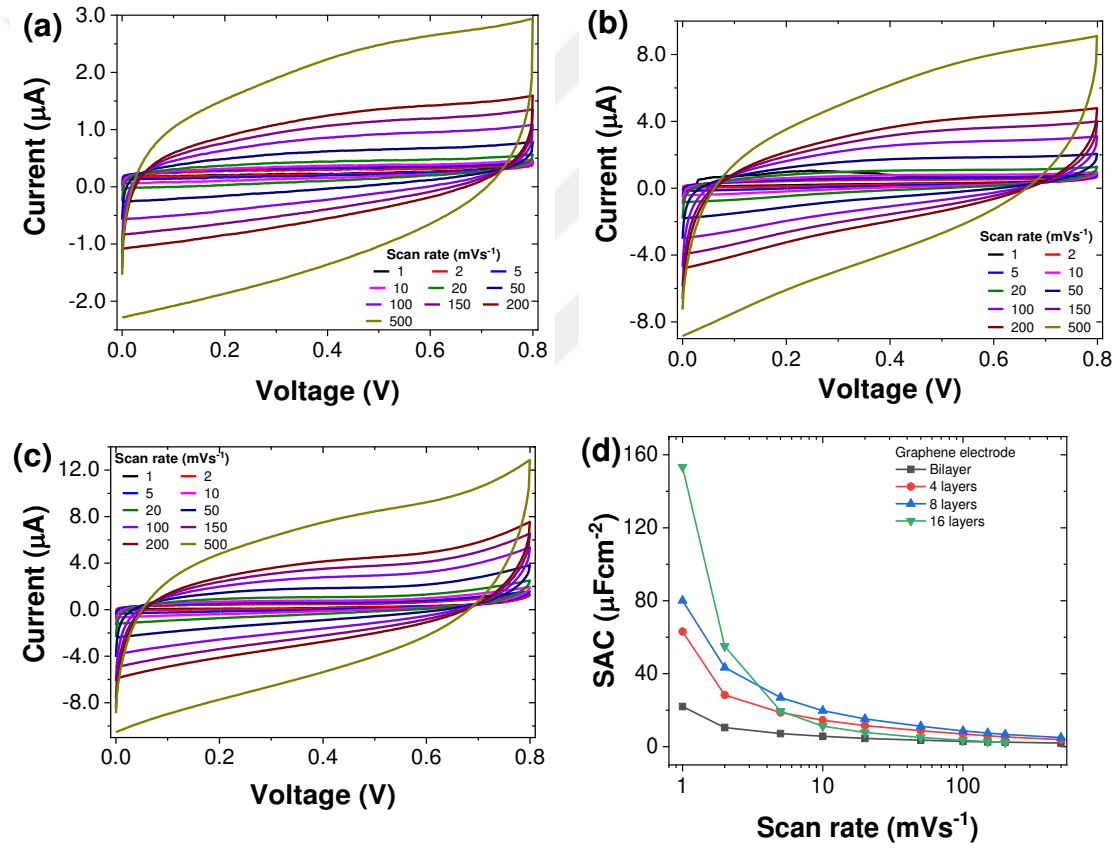

Figure 2.11. *Electrochemical characterization of graphene supercapacitors: (a-c) CV curves for bilayer, four-layer, and eight-layer graphene at various scan rates, and (d) SAC vs. scan rate.*

Capacitance values calculated for various scan rates are summarized in Table 2.2. Notably, the 4-layer graphene electrode exhibited the highest SGC, reaching 316.1 F g^{-1} at a scan rate of 1 mV s^{-1} and 141.8 F g^{-1} at 2 mV s^{-1}, demonstrating its superior charge storage capability compared to the 2- and 8-layer devices. The specific energy densities (SEDs) and specific power densities (SPDs) for the 2-, 4-, and 8-layer graphene electrodes

were also calculated. The 2-layer graphene device achieved SEDs of 16.3 Wh kg^{-1} at 589.5 kW kg^{-1}, the 4-layer device reached 28.1 Wh kg^{-1} at 127.8 kW kg^{-1}, and the 8-layer device had an SED of 16.8 Wh kg^{-1} at 62.5 kW kg^{-1}, highlighting the trade-off between energy density and power density across different layer configurations.

Figures 2.12(a–b) present the impedance response of supercapacitors fabricated using 2-, 4-, and 8-layer graphene electrodes. Typically, the equivalent series resistance (ESR) of a supercapacitor device is determined by extrapolating the intercept of the Nyquist curve with the real (*Z*real) axis. However, a closer examination of the zoomed-in Nyquist plot, shown in the Inset of Figure 2.12(a), reveals the initial formation of a semicircle. This observation suggests that a complete semicircle could potentially be observed at frequencies higher than the 1 MHz limit of the test instrument.

Table 2.2. *Specific capacitance data of supercapacitors with graphene electrodes composed of 2 to 16 layers (2L to 16L) in Na_2SO_4 electrolyte.*

Scan rate	**SAC (μF cm^{-2})**				**SGC (F g^{-1})**				**SVC (F cm^{-3})**			
(mV s^{-1})	**2L**	**4L**	**8L**	**16L**	**2L**	**4L**	**8L**	**16L**	**2L**	**4L**	**8L**	**16L**
1	44	126	160	307	239	316	193	268	542	717	438	608
2	21	57	87	110	114	142	105	96	259	322	237	218
5	14	38	54	39	78	94	65	34	177	213	147	77
10	11	29	39	22	62	73	48	20	140	165	108	45
20	9	23	30	16	49	58	37	14	112	131	83	31
50	7	18	22	10	39	44	27	9	88	99	61	20
100	6	14	17	7	32	35	21	6	72	79	47	14
150	5	12	15	5	28	30	18	5	64	67	41	11
200	5	11	13	5	27	27	16	4	61	60	37	9
500	4	8	10		21	19	12		49	44	27	

As a result, the resistance values extrapolated from the Z_{real} axis intercept-427.2 Ω for the 2-layer graphene electrode, 697.5 Ω for the 4-layer electrode, and 685.8 Ω for the 8-layer electrode—are more representative of the charge transfer resistance (R_{ct}) than the ESR. The presence of the emerging semicircle indicates that charge transfer processes at the electrode-electrolyte interface play a significant role in the overall impedance of these devices, particularly at higher frequencies. This nuanced behavior underscores the importance of considering the limitations of the test equipment when interpreting

impedance data and highlights the interplay between charge transfer dynamics and the structural configuration of the graphene layers in supercapacitor performance.

Figure 2.12(b) presents the Bode plot of the supercapacitors, which includes both the impedance magnitude and the phase angle. The phase angle approaches zero at high frequencies, indicative of resistive behavior dominating at these frequencies. Conversely, the impedance magnitude in the Bode plot exhibits a gradient that trends toward infinity at intermediate frequencies and approaches zero at both low and high frequencies. This characteristic behavior reflects the capacitive nature of the devices, consistent with the performance of electrochemical EDLCs.

Furthermore, Figure 2.12(c) displays the galvanostatic charge-discharge (GCD) curve for a supercapacitor with 2-layer graphene electrodes. Notably, the device demonstrates exceptional durability, retaining 100% of its charge capacity even after 10,000 GCD cycles at a current density of 10 A g^{-1}. This remarkable charge retention underscores the superior cycle stability of the graphene-based electrodes, making them highly suitable for long-term energy storage applications.

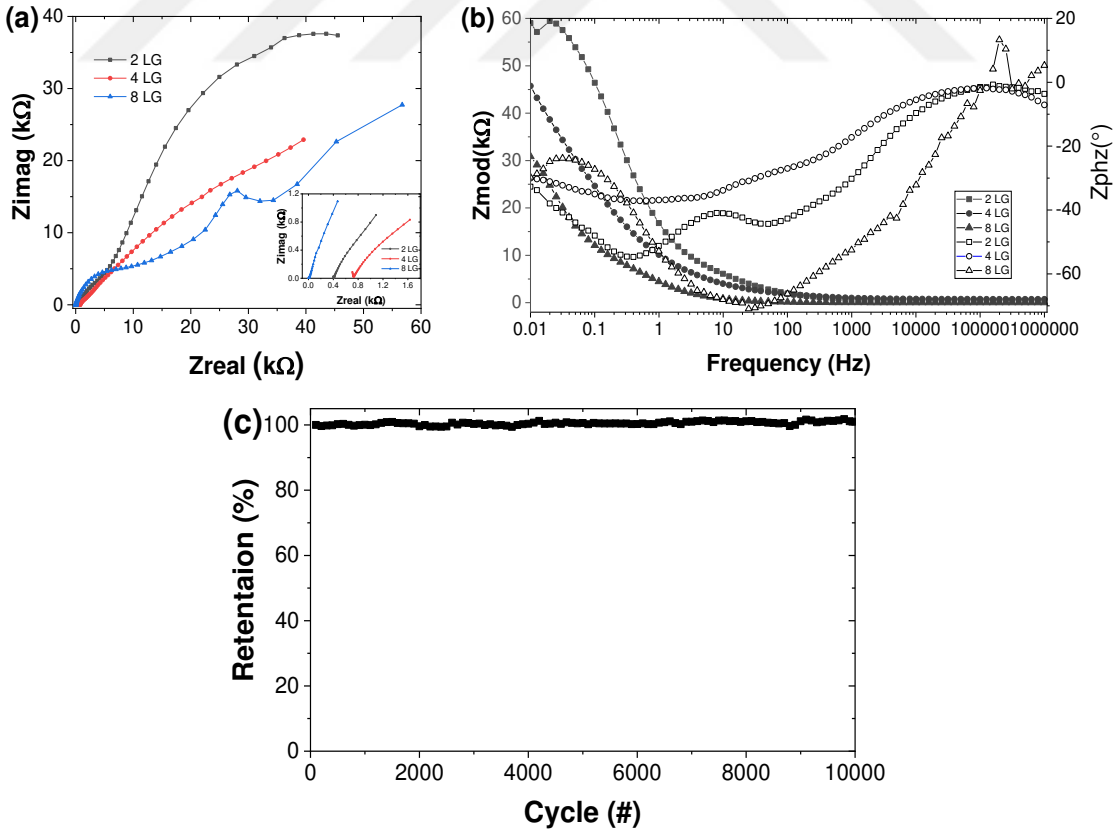

Figure 2.12 *EIS results of 2-, 4-, and 8-layer graphene and GCD of 4-layer graphene: (a) Nyquist plots, (b) Bode plots, and (c) GCD performance over 10,000 cycles. (Ibrahim, 2022).*

At a scan rate of 1 mV s^{-1}, PAT graphene supercapacitors outperform previously reported graphene supercapacitors in terms of gravimetric capacitance (Table 2.3). As previously stated, enhanced electrolyte ion intercalation is responsible for such remarkable electrochemical performance.

Table 2.3. *Comparison of the* results of graphene supercapacitors *with state-of-the-art*.

Active material	Electrolyte	Rate (A g^{-1})	SAC (F g^{-1})	SED (mWh kg^{-1})	SPD (kW kg^{-1})
Curved graphene[45]	$[EMIM]BF_4$	1	154.1	85.6	1.14
a-MEGO [76]	------	1	166	~70	-----
LSG [77]	------	1	276	28.33	-----
EM-CCG film [78]	------	1	167.1	88.24	6.88
HAG[49]	$[EMIM]BF_4$	1	306.03	148.8	30.95
This work	1M Na_2SO_4	1 mV s^{-1}	316.1	101.2	127.8

2.3.4. Summary

In conclusion, bilayer graphene was synthesized using CVD and employed as the electrode material for supercapacitors. Through repeated PAT techniques, rotationally stacked graphene electrodes with 2, 4, 8, and 16 layers were produced. This stacking approach effectively minimizes layer aggregation, and Raman analysis confirmed that the intrinsic properties of single-layer graphene are preserved in the rotationally stacked structure. The electrochemical performance of these graphene electrodes was thoroughly evaluated using CV, EIS, and GCD tests.

This chapter showcases the development of rotationally stacked graphene electrodes through CVD synthesis, achieving specific gravimetric capacitance values of up to 316 F g^{-1} in aqueous electrolytes. Notably, after 10,000 charge-discharge cycles, the supercapacitors retained 100% of their capacitance, underscoring their remarkable cycle stability. The findings emphasize the critical role of reducing aggregation and optimizing the interlayer interfaces to enhance ion-accessibility and long-term electrochemical performance.

3. MXENES: THE 2D MARVELS

3.1. Overview

In 2011, Naguib and colleagues [79] achieved a significant breakthrough by selectively etching aluminum (Al) from the compound Ti_3AlC_2, resulting in the creation of 2D $Ti_3C_2T_x$ nanocrystals. This discovery introduced a novel class of materials known as MXenes. Since then, MXenes have captivated the interest of materials scientists due to their remarkable properties. The term “MXene” can be deconstructed as M, which represents a transition metal, X which can be either carbon, nitrogen, or a carbonitride, and the suffix “-ene”, is added to highlight their structural similarity to graphene [80].

3.1.1. MXene synthesis techniques

The synthesis of 2D MXenes involves two primary approaches: top-down and bottom-up methods. In the top-down approach, large crystal quantities are exfoliated into single-layered MXene sheets using techniques such as HF etching [81], in situ HF etching [82], molten salt etching [83], and electrochemical etching [84]. On the other hand, bottom-up strategies involve growing MXenes from atoms or molecules. While certain MXenes have been created using bottom-up techniques, the majority are made using top-down methods, deriving their structure and composition from bulk-layered predecessors of carbide and nitride [85].

3.1.1.1. Top-down approach

Top-down synthesis methods are widely employed for producing MXenes due to their simplicity and scalability, involving the selective removal of specific elements from layered precursors. The relatively weak M–A bonds in MAX phases make it possible to produce 2D MXenes by selectively etching out the more reactive "A" element, as illustrated in Figure 3.1 [86,87]. The M–X bond in these structures can exhibit ionic, covalent, or metallic characteristics. Etchant solutions containing aqueous fluorides are commonly employed for this selective etching process. The most widely studied precursors for MXenes are stacked ternary carbides and nitrides known as MAX phases [88], which has the general formula $M_{n+1}AX_n$, where n is an integer between 1 and 4. In this formula, "M" represents an early transition metal, "A" corresponds to an element from groups 13 to 15 of the periodic table, and "X" stands for carbon, nitrogen, or a combination of both [89,90].

MAX phases exhibit a unique combination of ceramic and metallic properties, making them versatile for a range of applications. When converted into MXenes via etching, their chemical formula becomes $Mn_{+1}X_nT_x$, where "T" denotes surface termination groups such as F, OH, Cl, or O, and "x" indicates the number of surface terminations [91,92]. MXenes with higher n-values tend to exhibit greater stability [79]. The hydrophilic nature of MXenes arises from chemical etching and the presence of surface termination groups, which also influence their electrical conductivity and transport properties [89,90,93].

To date, over 100 MAX phases have been identified and synthesized by varying the combinations of their components [94,95]. However, only about thirty MXene variants have been experimentally produced and characterized, suggesting significant potential for discovering novel MXenes with unique and useful properties.

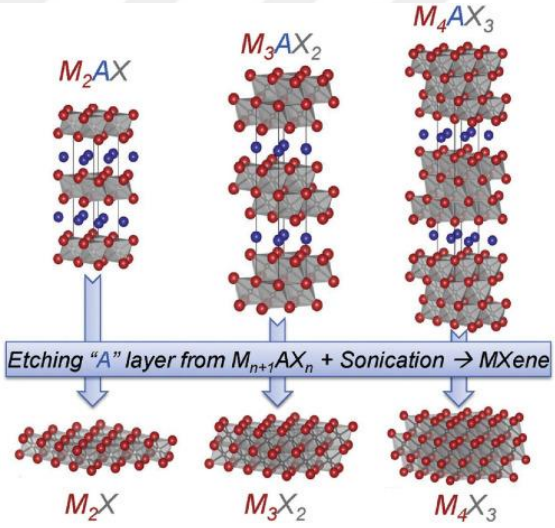

Figure 3.1. *An illustration of selective etching of MXenes from their MAX precursors (Naguib, 2013).*

3.1.1.2. Bottom-up approach

MXenes synthesized by selective etching tend to have some defects, and surface terminations and are limited to a maximum lateral size of about 10 µm. However, research has shown that high-quality, low-defect concentration, ultrathin Mo_2C crystals can be synthesized by CVD processes [96–98]. CVD MXene has lateral sizes up to 100 µm and exhibits low-temperature 2D superconductivity.

The process of synthesizing MXenes by CVD involves using copper foil substrates that usually sit above Molybdenum foils, with methane gas serving as the carbon source, as illustrated in Figure 3.2 [99]. During synthesis Cu, which also plays the

role of a catalyst dissolves and forms a Cu-Mo alloy. A constant stream of H_2 is maintained throughout the synthesis process, primarily serving as the carrier gas. Additionally, H_2 facilitates the breakdown of CH_4 to release reactive carbon species, which subsequently react with Mo atoms that have diffused through the Cu-Mo alloy. Furthermore, H_2 plays a crucial role in lowering the activation energy of the Mo-C reaction, enhancing the efficiency of the synthesis process. This way of synthesis is a modification of the method used for growing high-quality graphene [100,101].

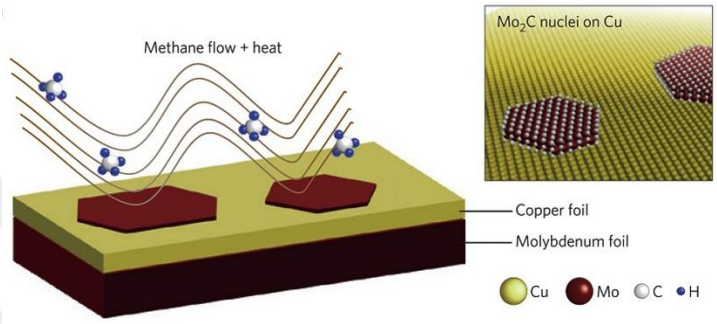

Figure 3.2. *Schematic illustration of the synthesis process of Mo_2C MXene through the reaction of molybdenum and carbon precursors in a CVD system (Gogotsi, 2015).*

The perfect crystals of molybdenum carbide (α-Mo_2C structure) differ from other MXenes in the same way as perfect graphene differs from chemically functionalized and defective reduced graphene oxide. The benefits of using CVD to synthesize MXenes are manyfold as listed below.

- The presence of hexagonal, triangular, or other well-formed carbide crystals, often larger than 100 μm, simplifies the study of their intrinsic properties compared to solution-processed flakes with smaller lateral dimensions (less than 10 μm).
- These well-shaped crystals exhibit excellent structural perfection and a thickness exceeding a single lattice unit, rendering them robust and chemically stable. Furthermore, researchers can explore 2D transport properties and catalytic reactions on specific crystal faces of these pristine specimens.
- The ability to adjust the number of layers in transition metal carbides by modifying growth conditions opens the possibility of creating thicker 2D crystal films with properties like bulk carbides. These films could potentially rival nitrides in applications such as plasmonic.

- While the synthesis of carbide monolayers using this method remains unproven, researchers can already explore some of the unique properties predicted for 2D carbide layers in these thin crystals. For example, Xu and colleagues [96] demonstrated that as the crystal thickness decreases to approximately 3 nm, the superconducting transition is suppressed in this pristine system, providing clear evidence of intrinsic thickness-dependent properties.

3.1.2. Structure of MXenes

Hexagonally close-packed (HCP) crystal structures generally characterize MXenes. MXenes with the general formula M_2X typically exhibit a hexagonal close-packed (HCP) atomic arrangement following an ABABAB sequence, while those with the formulas M_3X_2 and M_4X_3 tend to adopt a face-centered cubic (FCC) arrangement characterized by an ABCABC sequence [102,103]. Computational simulations are frequently employed to explore new stable compounds and analyze MXene structures [104,105]. The first structure of multilayer MXenes was proposed based on density functional theory (DFT) simulations [105].

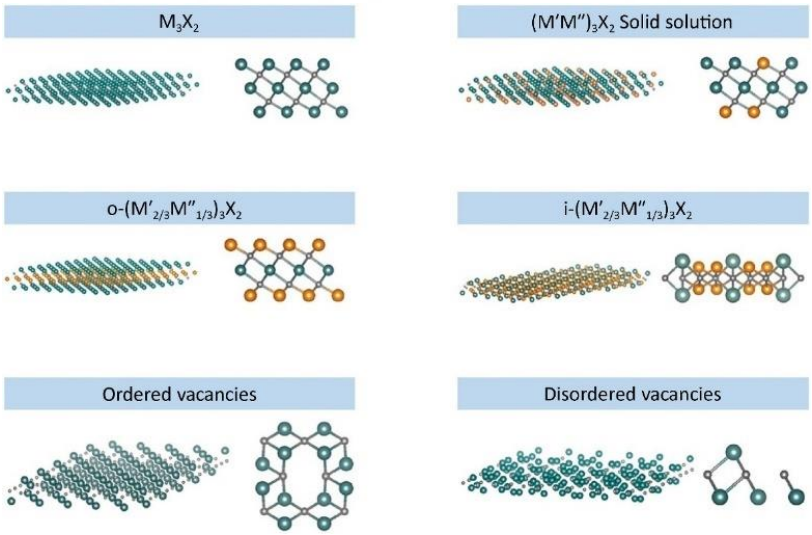

Figure 3.3. *MXene structures and configurations (Ronchi et al., 2019).*

Through theoretical calculations, researchers have identified six different forms of MXene structures, including mono-M elements like Ti_2C and Nb_4C_3, ordered out-of-plane double-M elements such as Mo_2TiC_2 and $Mo_2Ti_2C_3$, and ordered in-plane double-M elements (e.g., $Mo_{2/3}$), where distinct M elements are arranged in the basal plane [106].

Vacancies in these structures can be either randomly distributed, as seen in $Nb_{4/3}CT_x$ [107], or ordered, as in $Mo_{4/3}CT_x$ [108] and $W_{4/3}CT_x$ [109]. These computational investigations provide valuable insights into MXene structural characteristics and support the discovery of novel and stable MXene compounds. A schematic illustration of MXene structures is provided in Figure 3.3 [110].

3.1.3. Properties of MXenes for energy storage applications

Due in large part to their high volumetric capacitance, MXenes have demonstrated a great deal of promise for energy storage applications [38,82]. The method of production, which mainly entails selective etching with HF or fluoride-based chemicals and results in arbitrary functionalization, has a significant impact on the properties of MXenes [89,90]. MXenes created through selective etching have a carbide core that ensures electronic conductivity and a surface resembling a transition metal oxide that can go through redox processes [111]. MXenes have attracted significant interest due to their immense potential in energy storage applications, driven by several compelling factors including:

1. **High surface area:** MXenes possesses a vast surface area, providing ample sites for charge storage. MXenes are capable of intercalated pseudo capacitance due to functional terminations which further increase their surface area [112]. This property directly impacts their energy storage capabilities. The incorporation of MXenes into supercapacitor electrodes has the potential to boost its energy density as they can act as "energy sponges," effectively storing more charge.
2. **Stability:** MXenes are remarkably stable, even in harsh environments. This stability ensures long-term performance. MXenes remain stable across a wide range of temperatures and humidity levels, making them adaptable to various conditions.
3. **Hydrophilicity:** Their affinity for water molecules enhances their electrochemical behavior. This property contributes to efficient charge transfer. The stable hydrophilicity of MXene in aqueous solutions is mostly due to the presence of O and OH groups. Furthermore, the electrochemical outcome of MXene-based electrodes is significantly influenced by the surface terminal groups of MXene [113].
4. **Theoretical capacitance:** Nonfunctionalized V_2C and Mo_2C, as members of the MXene family, exhibit impressive quantum capacitance. Using density functional

theory, they boast values of 3.4, and 3.2 mF cm^{-2} respectively [39]. This underscores their enormous potential for supercapacitor applications.

5. **Volumetric capacitance:** As demonstrated in a study by Ghidiu et al., MXenes exhibit high volumetric capacitance, enabling them to store more energy within a given volume, which is crucial for compact devices [82].
6. **Versatile properties:** MXenes exhibit diverse and tunable surface and bulk chemistry, primarily due to the functional groups that result as by-products of selective etching. These surface modifications can significantly alter their electronic, thermal, optical, and mechanical properties, making MXenes valuable for various components of energy storage devices [114].
7. **Conductivity:** First-principle calculations imply that MXenes without surface terminations are metallic electrical conductors, similar to the MAX phases [115]. Because of MXenes' adaptability, surface termination groups can be adjusted, and M and X elements can be carefully chosen to improve MXene's conductivity. Because of its versatility, MXene can have characteristics that range from metallic to completely insulative or semi-conductive [116,117]. High energy density and fast discharge rates are key characteristics of supercapacitors, making high-conductivity electrodes essential. As such, MXenes are often associated with superior conductivity due to their large lateral dimensions and low defect concentrations, which enhance their ability to conduct electricity [118,119].
8. **Mechanical flexibility:** 2D MXenes possess excellent mechanical strength, elasticity, tractability, and machinability, and their flexibility makes them perfect fits for flexible supercapacitors. Bendable and micro-supercapacitors are examples of compact, portable "micro-electronic" system devices that have become much more necessary in recent years [120].

In summary, MXenes offer a pathway to bridge the gap between high-power supercapacitors and energy-dense Li-ion batteries. As research continues, we may witness breakthroughs that revolutionize energy storage technology.

3.2. Synthesis of Mo_2C MXene via CVD and Subsequent Characterization

This section discusses the synthesis of Mo_2C MXene using chemical vapor deposition (CVD) and provides an overview of the characterization techniques employed to analyze the resulting material.

3.2.1. Synthesis of Mo_2C by CVD

The CVD technique is employed to synthesize Mo_2C MXene crystals on Cu substrates, requiring precise control over temperature and gas flow to achieve the desired material properties. In the setup depicted in Figure 3.4, a two-zone split furnace was utilized to synthesize the Mo_2C samples analyzed in this study. The samples were prepared at three distinct temperatures—1085 °C, 1120 °C, and 1150 °C—while keeping all other conditions constant. A quartz tube furnace with a chamber diameter of 1 inch was employed, operating at a ramp rate of approximately 30 °C/min under ambient pressure. The 0.025 mm thick Cu foil, which serves as both the substrate and catalyst, was meticulously cleaned using deionized (DI) water, acetone, and ethanol. This foil was then placed over a 0.025 mm thick Mo foil (Alfa Aesar, 99.95% purity), which acted as the metallic precursor.

Before ramping to the target temperature, the system was evacuated to a base pressure of ~0 Torr to remove any residual atmospheric gases and then purged with hydrogen (H_2). During the entire process, including the cooling stage, a constant flow of H_2 at 100 sccm was maintained. Once the growth temperature was achieved, methane (CH_4) was introduced at a flow rate of 15 sccm using calibrated mass flow controllers, and the reaction was allowed to proceed for 30 minutes. After the reaction phase, the furnace was opened to facilitate the natural cooling of the sample to room temperature, with H_2 flow sustained throughout.

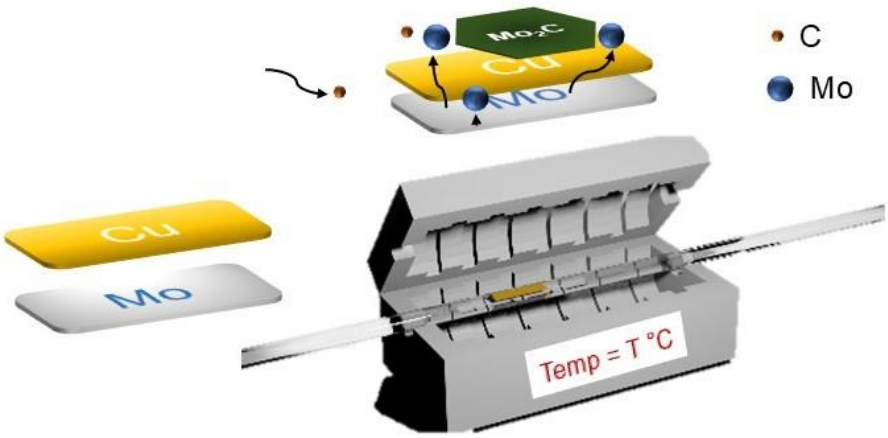

Figure 3.4. *Experimental setup for the synthesis of Mo_2C MXenes using a CVD system.*

3.2.2. Characterization of Mo_2C MXenes

Scanning electron and optical microscopy, X-ray diffraction (XRD), Raman and energy dispersive X-ray (EDX) spectroscopy, X-ray photoelectron spectroscopy (XPS), and atomic force microscopy (AFM) were employed to analyze the produced MXene samples. A Nikon Eclipse LV100NDA microscope was used to examine the samples up close, a WITec alpha-300R device with a 532 nm laser source was utilized to get Raman spectra, and a portable NanoMagnetics-ezAFMTM in tapping mode was utilized to do AFM measurements.

To illustrate the findings, optical images magnified 50 times were captured to showcase the growth of Mo_2C on Cu substrates at varying temperatures of 1085, 1120, and 1150 °C. These images, as presented in Figures 3.5(a-c), provide a detailed view of the Mo_2C formation process under different synthesis conditions. ImageJ calculations, as shown in Figure 3.5(d), reveal that the Mo_2C flakes synthesized at 1085 °C cover 22.9% of the substrate, indicating a moderate extent of growth. In contrast, the flakes produced at higher temperatures of 1120 and 1150 °C exhibit significantly greater coverage, with values of 73.2% and 95.2%, respectively, demonstrating a more extensive growth.

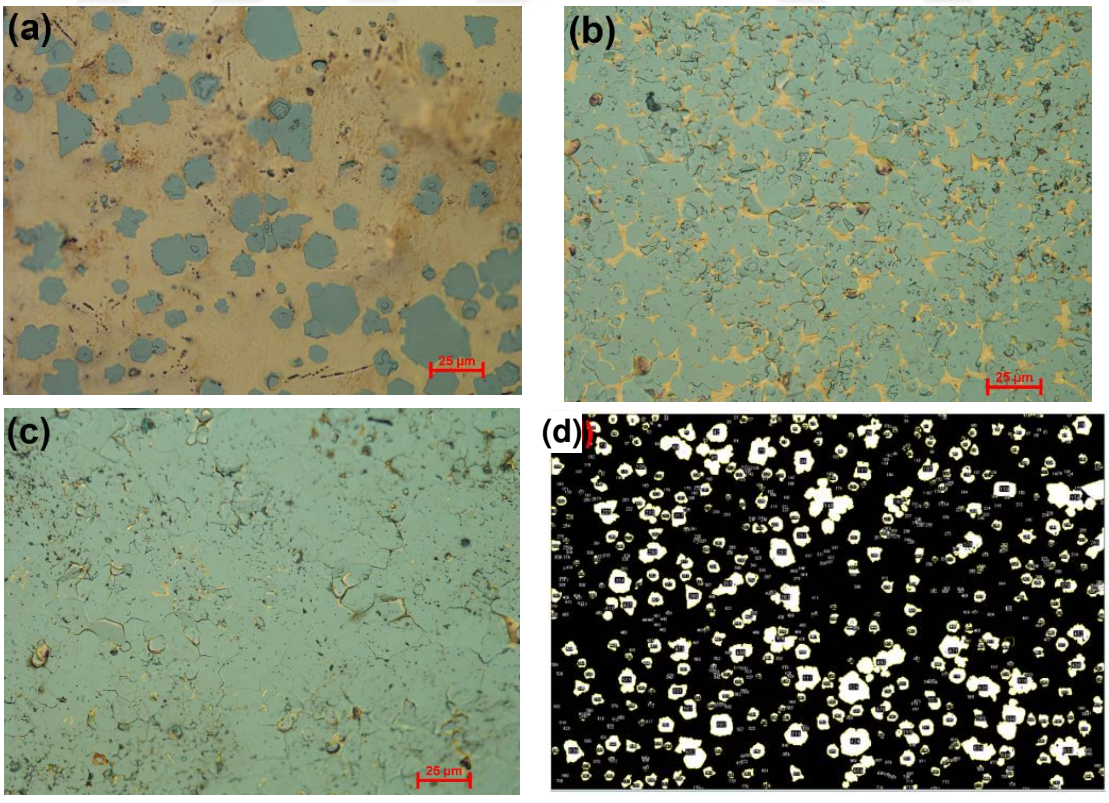

Figure 3.5. *A close-up view of Mo_2C on Copper substrates grown at: (a) 1085 °C, (b) 1120 °C, and (c) 1150 °C, and (d) the ImageJ estimation results from a 20x magnified image of LT-MXene.*

The distinct differences in substrate coverage among the temperature variants underscore the influence of thermal conditions on the growth kinetics and morphology of Mo_2C. Notably, the gradual increase in coverage with rising temperatures suggests a temperature-dependent growth mechanism, where higher temperatures facilitate more extensive flake formation and substrate coverage. This observation aligns with established principles in materials science regarding the role of temperature in influencing crystallinity, surface diffusion, and nucleation processes during thin film deposition.

The Mo_2C samples were also characterized using Raman spectroscopy, a technique widely employed to analyze the structural and vibrational properties of materials. Among the numerous Raman modes associated with the Mo_2C crystal as documented in the literature [98,121,122], a total of six experimental modes were observed and are depicted in Figure 3.6. Specifically, the distinctive A_g modes at 232 and 650.1 cm^{-1}, along with the B_{3g} Raman modes at 166.6 and 209.5 cm^{-1}, were prominently evident, exhibiting a strong correlation with theoretical predictions based on group theory calculations [123]. The observed peak at 166.6 cm^{-1} closely matches the B_{3g} mode at 167.6 cm^{-1} reported in the literature, while the peak at 209.9 cm^{-1} aligns well with the literature value of 213 cm^{-1}. Similarly, the A_g modes at 232 cm^{-1} and 650 cm^{-1} correspond to the peaks at 235 cm^{-1} and 652.6 cm^{-1} in the theoretical spectrum, respectively.

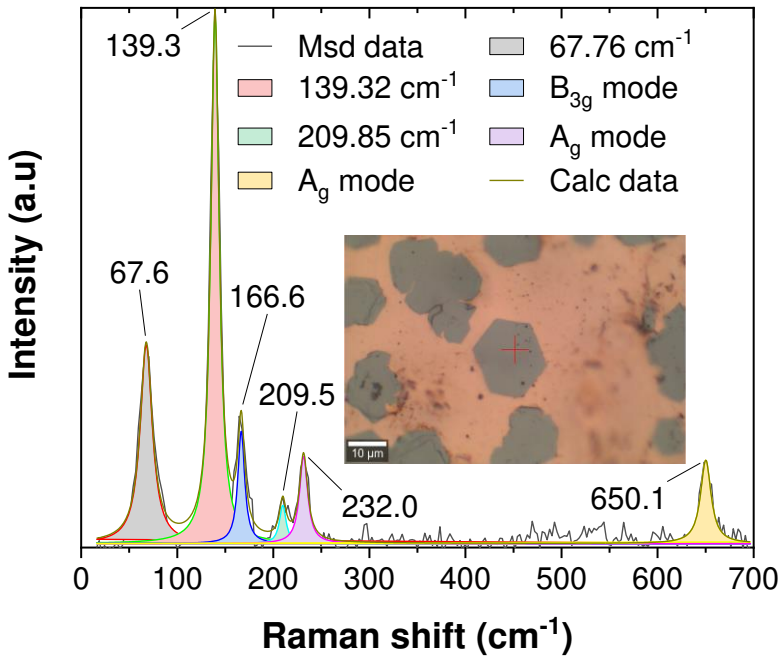

Figure 3.6. *The Raman spectrum of as-grown Mo_2C. Inset: A 100 times magnified view of Mo_2C showing the point from which the Raman spectrum is sampled.*

As established by Li, Tianshu et al. [121], the origin of the B_{3g} mode at 166.6 cm^{-1} can be attributed to the vibrational motion of Mo atoms within the b-c plane, given the orientation of the Mo_2C crystal in the a-c plane. Conversely, the A_g mode at 232 cm^{-1}, as well as the B_{3g} mode at 209.9 cm^{-1}, predominantly stem from the oscillation of Mo atoms situated outside the b-c plane. Additionally, the A_g mode at 650 cm^{-1} signifies the vibrational behavior of C atoms along the b-axis, contributing to a comprehensive understanding of the structural dynamics and vibrational modes within the Mo_2C crystal lattice.

Following the Raman spectroscopy analysis, scanning electron microscopy (SEM) was employed to further investigate the structural and morphological features of the MXene samples deposited on Cu substrates. Utilizing a 10 kV accelerating voltage for imaging, the detailed micrographs are presented in Figure 3.7(a). Within this micrograph, the larger hexagonal flakes, averaging around 12 µm in size, are observed. Smaller flakes can be observed forming over some of the larger flakes which also is an indication of a layered stacking.

Continuing with the characterization of the Mo_2C sample, its X-ray diffraction (XRD) pattern, shown in Figure 3.7(b), provides crucial insights into its crystallographic orientation. The prominent diffraction peaks at 2θ angles of 38° and 43° indicate that the growth of Mo_2C flakes predominantly occurred along the (100) direction, consistent with findings from previous studies [96].

The analysis via XRD and Raman spectroscopy corroborates the orthorhombic nature of the flakes, as evidenced by the distinct peaks at 232 and 650 cm^{-1}, consistent with earlier research outcomes [97,124]. These spectroscopic techniques provide valuable structural information, highlighting the crystalline integrity and phase purity of the Mo_2C flakes.

Energy Dispersive X-ray (EDX) spectroscopy was employed for further analysis of the sample, with the results shown in Figure 3.7(c), providing insights into its elemental composition. Captured at the specific location highlighted in the Inset, the spectrum reveals peaks exclusively corresponding to Mo and C, confirming the absence of functional group terminations in the MXene synthesized via chemical vapor deposition (CVD). These findings highlight the purity and compositional uniformity of the CVD-produced MXenes, aligning with previous reports [122,125].

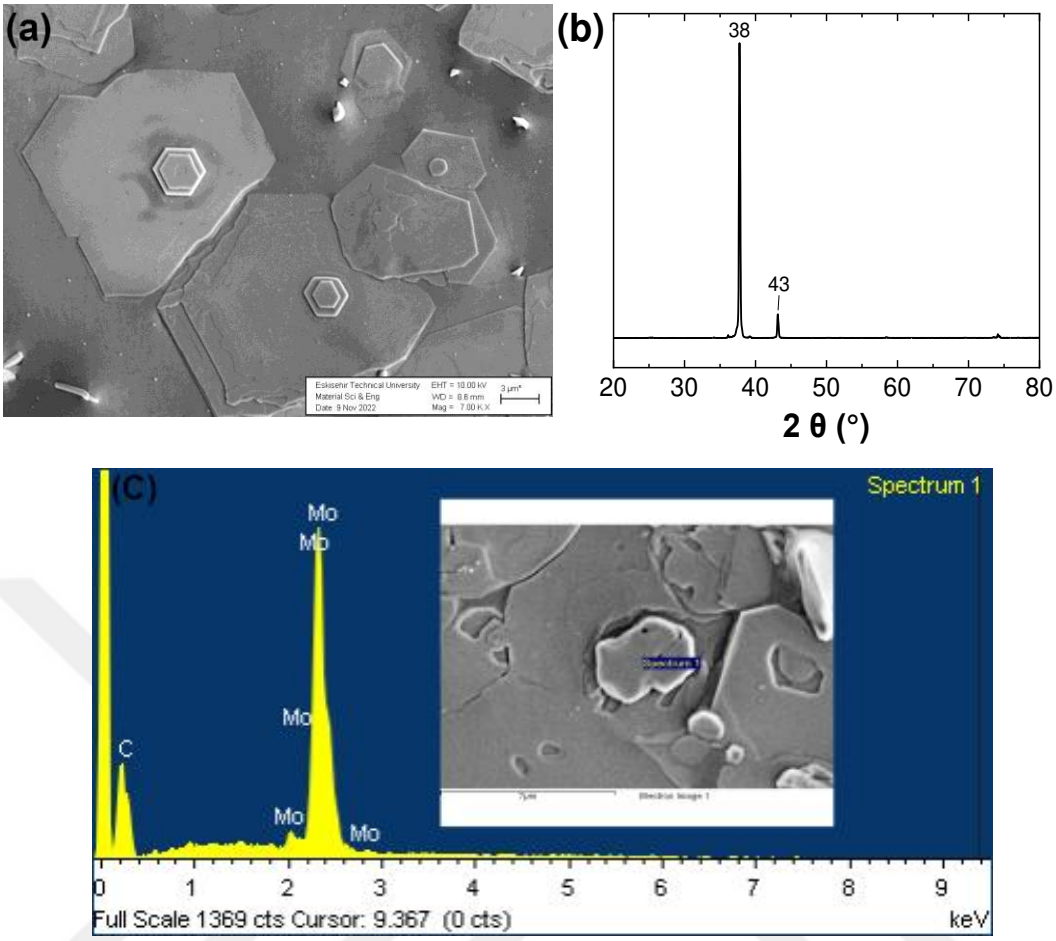

Figure 3.7. *Mo_2C characterization showing: (a) its scanning electron microscope (SEM) image, (b) X-ray diffraction (XRD) pattern, and (c) its Energy Dispersive X-ray (EDX) spectrum with an accompanying SEM image in the Inset indicating the sampling location.*

X-ray photoelectron spectroscopy (XPS) was utilized to investigate the structural and chemical composition of the MXene structures synthesized via CVD, with the findings displayed in Figure 3.8. The Mo 3d spectrum (Figure 3.8(a)), which corresponds to the binding energies of electrons in the 3d orbital of molybdenum atoms, was deconvoluted into four distinct peaks, offering insights into the chemical environment and oxidation states of molybdenum. Peaks at binding energies of 228.7 eV and 231.9 eV are attributed to Mo–C bonds, confirming the successful incorporation of molybdenum carbide in the synthesized material. Additionally, peaks at 229.6 eV and 232.8 eV correspond to Mo^{4+} species, which result from surface oxidation of Mo_2C when exposed to air. This surface oxidation is a common phenomenon observed in transition metal carbides, as the outermost layer interacts with oxygen and forms a protective oxide layer.

The C 1s spectrum (Figure 3.8(b)), representing the binding energy of electrons in the 1s orbital of carbon, was analyzed and fitted with a Lorentzian function. This

analysis identified four distinct peaks, further validating the material's composition. The peak at 283.8 eV corresponds to the Mo–C bond, indicative of strong carbide formation. Meanwhile, the peak at 284.8 eV represents sp^2 hybridized C–C bonds, which are characteristic of graphene.

These XPS results align closely with previously reported data in the literature [97,124], providing strong evidence for the successful synthesis of Mo_2C alongside graphene. This dual-phase structure is advantageous, as the combination of Mo_2C and graphene can enhance the electrochemical performance of the material, leveraging the high conductivity of graphene and the catalytic or capacitive properties of Mo_2C.

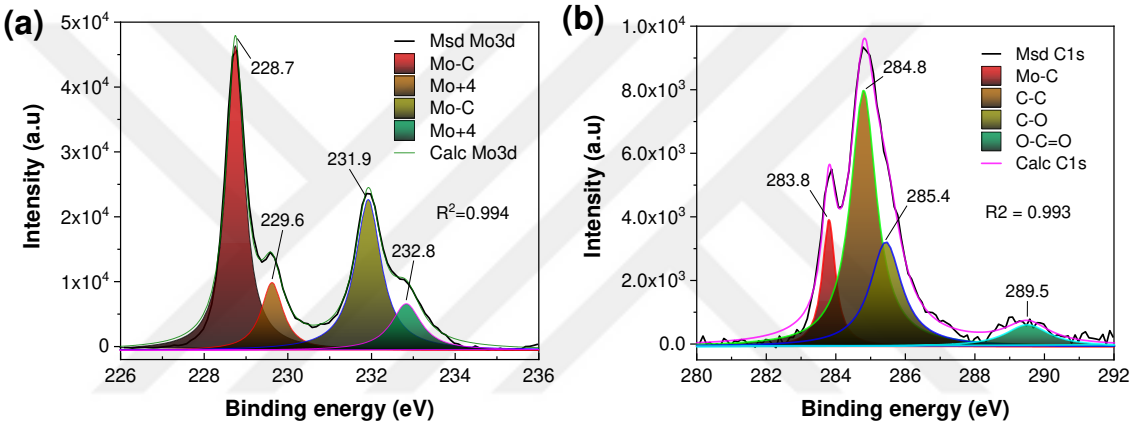

Figure 3.8. *X-ray photoelectron spectra of Mo_2C, showing the fitted spectra for (a) Mo 3d and (d) C 1s.*

Finally, atomic force microscopy (AFM) was employed to examine the morphological details of the Mo_2C MXene, with the results presented in Figure 3.9. The AFM images provide a comprehensive view of the structural characteristics of Mo_2C MXene flakes synthesized at varying temperatures, supplemented by precise step-height measurements to determine their thickness.

In Figure 3.9(a), the AFM image of MXene flakes synthesized at 1085 °C reveals a thickness of approximately 42.4 nm, serving as a baseline for comparison. At a slightly higher synthesis temperature of 1120 °C, as shown in Figure 3.9(b), the MXene flakes exhibit a marginal increase in thickness, measured at approximately 44.8 nm. This trend continues in Figure 3.9(c), where MXene flakes synthesized at 1150 °C display a more pronounced thickness of approximately 48.6 nm.

These findings highlight a clear temperature-dependent growth trend, with the thickness of the MXene flakes progressively increasing as the synthesis temperature rises.

This observed behavior underscores the influence of temperature on the growth kinetics and structural evolution of CVD MXenes. The AFM images, together with the step-height measurements, provide valuable insights into the synthesis parameters that govern the morphological and structural properties of MXene materials, which are crucial for optimizing their performance in energy storage and other applications.

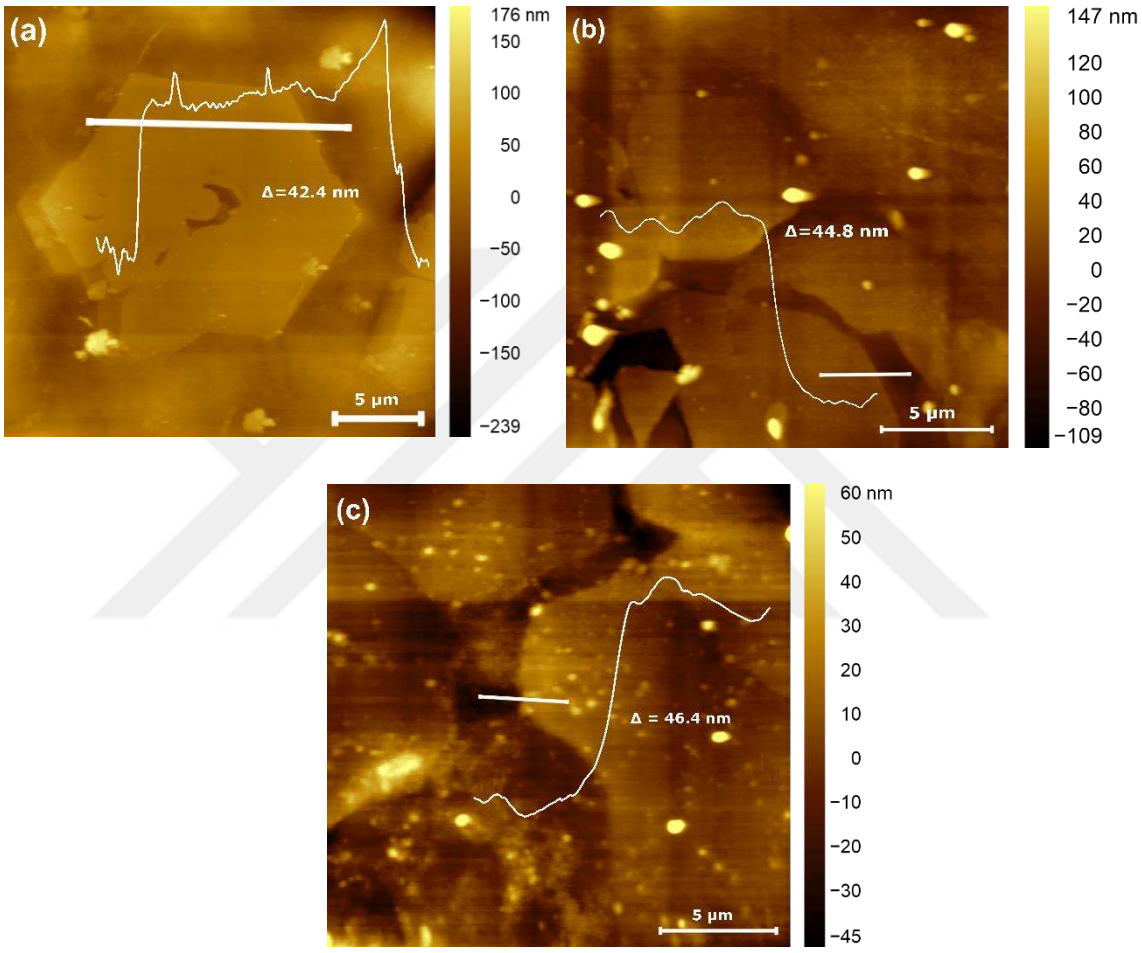

Figure 3.9. *The morphological analysis of Mo_2C flakes using Atomic Force Microscopy (AFM): Topographic views and thickness profiles of samples synthesized at temperatures of (a) 1085 °C, (b) 1120 °C, and (c) 1150 °C.*

3.3. Fabrication of MXene-Based Supercapacitors

Following the successful synthesis of Mo_2C MXene, the next step involves integrating them into functional devices. The fabrication process for MXene-based supercapacitors is straightforward and is outlined in the flow diagram shown in Figure 3.10. Since MXenes are directly deposited onto a metal substrate, the substrate itself can serve as the current collector. The Mo_2C thin film, deposited on a Cu substrate, is

transformed into supercapacitor electrodes by punching it into circular discs with a diameter of 12 mm. Separators are similarly punched into discs with a 16 mm diameter. To enhance the wettability of the Celgard separator, it is pre-soaked in the electrolyte solution for at least 24 hours before use.

The devices are assembled in a symmetric configuration, with an electrolyte-impregnated separator positioned between two identical electrodes as illustrated in Figure 3.10. For rapid analysis and post-test electrode characterization, the assembled configuration is enclosed within a stainless-steel split test cell. For devices utilizing ionic liquid (IL) electrolytes, the assembly process is conducted under an inert atmosphere within a glove box.

The performance of the devices was evaluated using a GAMRY Reference 600 instrument, and comprehensive characterization was conducted employing electrochemical impedance spectroscopy (EIS), cyclic voltammetry (CV), and galvanostatic charge-discharge (GCD) techniques. Following methodologies established in previous studies [101,126,127], the capacitance of the devices was determined either by analyzing the cyclic voltammograms using Equation 2.1 or by evaluating the GCD discharge curve with Equation 3.1. In Equation 3.1, i_ρ represents the current density applied during the test, expressed in A g^{-1}.

$$C = i_\rho \frac{dt}{\bar{d}v} \tag{3.1}$$

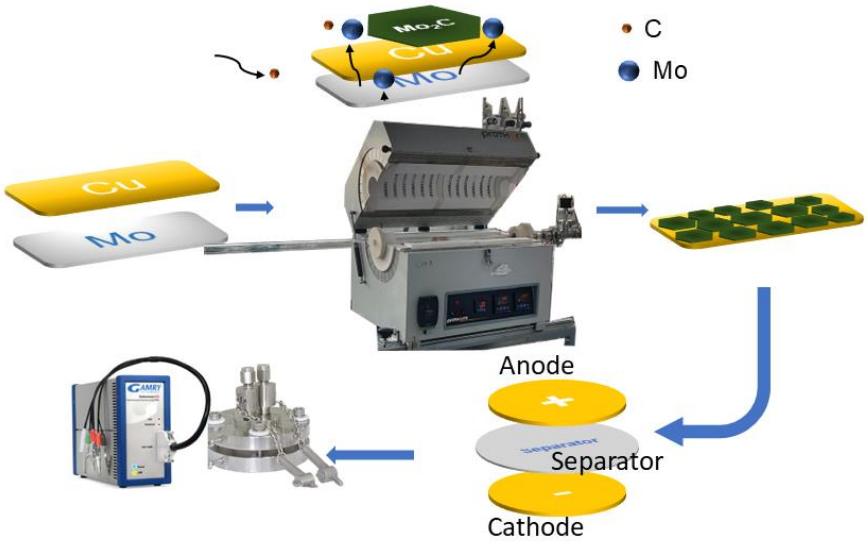

Figure 3.10. *Supercapacitor fabrication process flow, starting with substrate preparation, followed by CVD synthesis of Mo_2C MXenes, and concluding with testing of the grown MXenes as supercapacitor electrodes using a Gamry potentiostat.*

The separator plays a crucial role in supercapacitors, acting as a barrier between the electrodes to prevent electrical short circuits while allowing ion flow. Typically, separators are made from porous polymeric membranes, nonwoven materials, or composite materials [128]. In the context of MXene supercapacitors, two specific separators were utilized: laboratory-grade paper and celgard, each with distinct characteristics. Laboratory-grade paper, made of cellulose, and celgard, a commercially available polyolefin membrane, were compared in this study.

Celgard is widely used in commercial supercapacitors due to its fiber-forming properties, ease of pore formation during spinning, strong chemical stability, high mechanical strength, and cost-effectiveness [129]. These attributes make celgard an ideal choice for separators in supercapacitors. Figure 3.11 presents optical images of the celgard separator (CS) and laboratory-grade paper separator (LGPS). In Figure 3.11(a), the CS shows a fine network of tiny pores, barely visible at 50x magnification.

In contrast, Figure 3.11(b) depicts LGPS with a network of larger interwoven pores. Research has indicated that the size of these pores significantly influences the wetting behavior of supercapacitors, which in turn impacts the rate stability of the devices and their self-discharge rate [130].

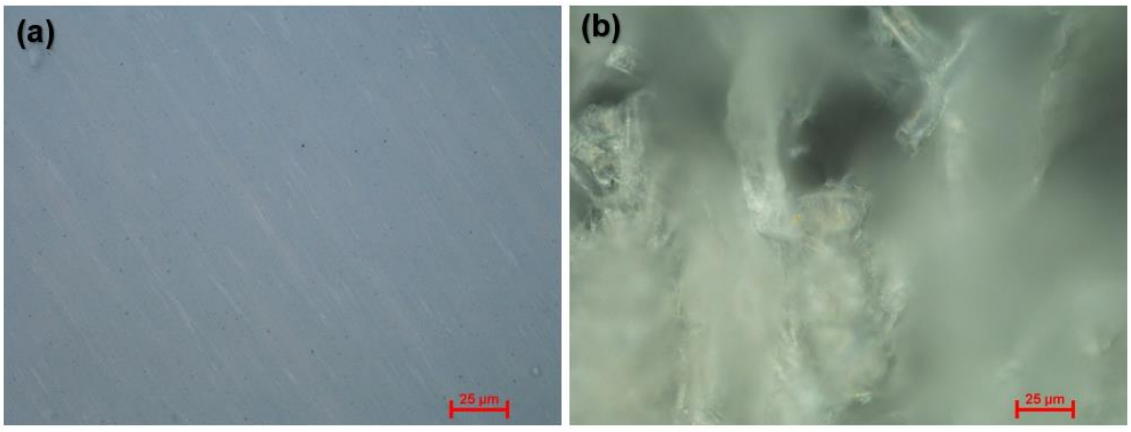

Figure 3.11. *The close-up views of (a) celgard, and (b) laboratory-grade paper separator at 50x magnification.*

3.4. MXenes as Supercapacitor Electrodes in Aqueous Electrolytes

Following the comprehensive characterization of the synthesized Mo_2C MXenes, their integration into electrochemical energy storage devices was explored. Supercapacitors, known for their ecological compatibility, exceptional cycle stability, and high power density, are an attractive platform for investigating the electrochemical

performance of MXenes. However, supercapacitors often face challenges related to their relatively low energy density compared to other energy storage technologies, such as Li-ion batteries. Consequently, current research focuses on enhancing the energy density of supercapacitors without compromising their power density or long-term stability [131–134].

As discussed in section 3.1.3, MXenes have emerged as promising candidates to address this limitation due to their intrinsic properties, including high surface area, excellent electrical conductivity, chemical stability, hydrophilicity, etc. These characteristics render them particularly suited for improving the energy density and volumetric capacitance of electrochemical double-layer capacitors (EDLCs) [37,38]. Additionally, MXenes exhibit remarkable biocompatibility and environmental adaptability, further underscoring their potential for high-performance supercapacitors [82,89,132,135–137]. Density functional theory (DFT) calculations highlight the exceptional quantum capacitances of non-functionalized MXenes, such as Mo_2C (3.2 mF cm^{-2}) and V_2C (3.4 mF cm^{-2}), which surpass the theoretical capacitance of many other materials, including monolayer graphene [39,40,51]. For example, a monolayer Mo_2C sample with a thickness of 0.36 nm exhibits a theoretical capacitance of 9816 F g^{-1}, which is significantly higher than the theoretical value of 550 F g^{-1} for graphene.

Despite their potential, most MXenes employed in supercapacitor applications to date have been synthesized through selective etching processes, resulting in functionalized MXenes. While surface functionalization can enhance surface area, it also reduces electrical conductivity, thereby diminishing overall electrochemical performance [138,139]. A study by Li et al. [140] demonstrated a nearly threefold increase in capacitance (from 245 to 517 F g^{-1}) after the removal of functional groups, highlighting the promise of non-functionalized MXenes for supercapacitor applications.

To further explore this potential, this section investigates non-functionalized Mo_2C MXenes synthesized via chemical vapor deposition (CVD) and evaluates their performance as supercapacitor electrodes. Unlike etched MXenes, CVD-derived MXenes are inherently non-functionalized, offering a unique opportunity to assess their electrochemical behavior without the influence of surface terminations.

This section represents the first study of its kind to examine supercapacitors fabricated using CVD-synthesized non-functionalized MXene electrodes. The fabricated symmetric supercapacitors utilize MXenes as the electrode material and employ a range

of separators, including commercially available Celgard and standard laboratory-grade paper, to investigate their performance. The electrochemical evaluation of these devices was conducted in a 1M Na_2SO_4 aqueous electrolyte using a Gamry potentiostat.

A systematic investigation was performed to evaluate the influence of key factors, such as the type of separator, the mass loading of the active material, and the coverage of the current collector by the MXene material, on the supercapacitor performance. The effects of these parameters on critical performance metrics, including specific capacitance, energy density, and power density, were analyzed to provide insights into optimizing electrode design for enhanced supercapacitor functionality.

3.4.1. Effects of separator on supercapacitor performance

The separator is a critical component in supercapacitor design, playing a pivotal role in maintaining physical isolation between electrodes while enabling ionic transport within the electrolyte. Its properties, such as porosity, thickness, and wettability, significantly influence the overall electrochemical performance of the device. In this section, the impact of different separators on the performance of symmetric supercapacitors fabricated with CVD-synthesized non-functionalized Mo_2C MXene electrodes is systematically examined. By comparing commercially available Celgard separators with alternative materials such as laboratory-grade paper, this analysis aims to provide insights into optimizing separator selection to enhance key performance parameters, including capacitance, energy density, and power density.

Figure 3.12 depicts the results obtained from supercapacitors constructed with MXene electrodes synthesized at 1085 °C, referred to as low-temperature MXenes (LT-MXenes). In Figure 3.12 (a) and (b), the cyclic voltammograms of the supercapacitors with MXene electrodes, coupled with laboratory-grade paper separators (LGPS) and celgard separators (CS), respectively, are showcased. The CV curve in Figure 3.12(a) exhibits a nearly rectangular shape, indicative of predominant electric double-layer capacitance (EDLC) behavior, aligning well with prior research findings [141,142]. A specific areal capacitance (SAC) of 12.7 mF cm^{-2}, corresponding to a specific gravimetric capacitance (SGC) of 326.4 F g^{-1} at a scan rate of 100 mV s^{-1}, was determined by analyzing the CV of the LT-MXene/ LGPS supercapacitor. However, it is noted that the SAC decreased to 5.9 mF cm^{-2} (152.6 F g^{-1}) at a higher scan rate of 1000 mVs^{-1}, indicating a scan rate stability of approximately 47%.

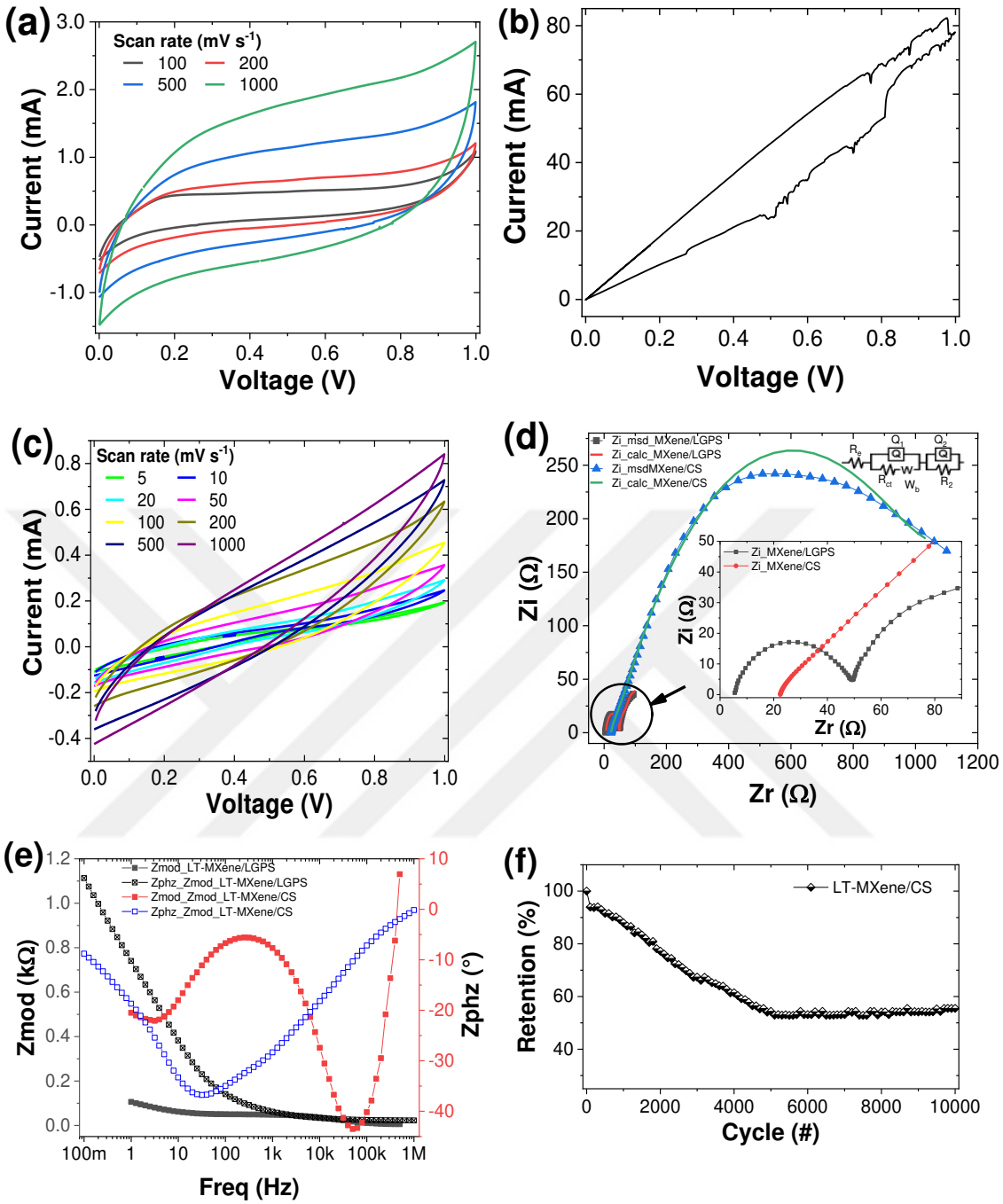

Figure 3.12. *Electrochemical Analysis (ECA) Results of MXene Supercapacitors: (a) CV Curves of LT-MXene/LGPS, (b) an example of an unreliable measurement, (c) CV Curve of LT-MXene/ CS, (d) Nyquist plot of both supercapacitors with inset showing equivalent circuit and zoomed view, (e) Bode plot of the two devices, and (f) outcome of 10,000 GCD cycles for LT-MXene/CS supercapacitor.*

This noteworthy performance can be attributed to the large mesh size of the LGPS according to Zhang and co-authors [143]. Large mesh-sized separators can enhance the device's ionic conductivity. It's worth mentioning that reliable results were typically observed at scan rates exceeding 100 mV s^{-1} for the LT-MXene/ LGPS supercapacitors,

as evident from Figure 3.12(a). Conversely, Figure 3.12(b) highlights an unreliable measurement at 50 mVs^{-1}, likely due to the LGPS 's large mesh size leading to rapid self-discharge, particularly noticeable at slower scan speeds.

The cyclic voltammograms of the LT-MXene/CS supercapacitor, depicted in Figure 3.12(c), exhibit quasi-rectangular shapes, indicating a significant presence of pseudo capacitive activity. This deviation from a perfect rectangular shape is typically observed when contact resistance increases, causing the optimal CV curve shape to transform into a pointed-edged elliptical shape, as documented in prior studies [144,145]. The CS, characterized by a smaller mesh size averaging about ~0.05 µm with a porosity of 30% to 40%, plays a role in reducing the device's ionic conductivity. At a scan rate of 2 mV s^{-1}, the LT-MXene/CS supercapacitor demonstrated a SAC of 26.7 mF cm^{-2} (686 F g^{-1}). However, this SAC decreased to 3.2 mF cm^{-2} (81.4 F g^{-1}) at 100 mV s^{-1} and further dropped to 0.5 mF cm^{-2} (13.2 Fg^{-1}) at 1000 Vs^{-1}, resulting in rate stabilities of 6.5% and 16.2% (or 10.5 ‰), respectively. The specific capacitances at other scan speeds can be found in Table 3.1.

Table 3.1. *Specific capacitances of supercapacitors made with LT-MXene electrodes*

Scan rate (mV s^{-1})	SAC (mF cm^{-2}) of		SGC (F g^{-1}) of	
	LT-MXene/LGPS	LT-MXene/CS	LT-MXene/LGPS	LT-MXene/CS
5	___	23.83	___	631.60
10	___	17.63	___	467.30
20	___	10.99	___	291.24
50	___	8.44	___	223.71
100	25.39	6.33	672.73	167.76
200	20.53	4.44	544.07	117.68
500	15.03	1.96	398.23	52.00
1000	11.87	1.03	314.55	27.19

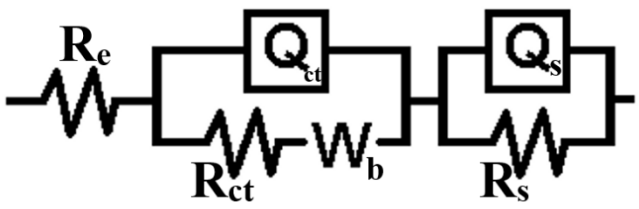

Figure 3.13. *A modified Randles equivalent circuit.*

Figures 3.12(d-e) present the Electrochemical Impedance Spectroscopy (EIS) results for the two devices across the frequency range of 100 mHz to 1 MHz. To analyze these results, a modified Randles equivalent circuit shown in Figure 3.13 and the Inset of Figure 3.12(d) [146] is employed. The equivalent circuit is utilized to fit the Nyquist curves of the two devices, and Table 3.2 provides details of the parameters constituting this equivalent circuit.

Table 3.2. *The modified-Randles equivalent circuit parameter and their meaning*

Parameter	Meaning
R_e	Equivalent series resistance (Re), is a bulk resistance that represents the total of the ohmic resistances (electrolyte, current collector, and cell connector resistances).
Q_{ct}	Constant phase element, which symbolizes the double layer's faulty capacitance.
R_{ct}	Charge transfer resistance which measures the passive film's resistance to charge transfer.
W_b	The semi-infinite Warburg diffusion element illustrates the mass transfer of ions at the interface between metal and substance.
R_s	Surface resistance
Q_s	The surface constant phase element represents pseudo capacitive processes.

The LT-MXene/LGPS and LT-MXene/CS configurations yielded Equivalent Series Resistances (ESRs) of 22.18 Ω and 5.68 Ω, respectively, indicating the higher ionic conductivity of the LGPS. Additional parameters of the equivalent circuit are presented in Table 3.3 for reference. Figure 3.12(e) illustrates the Bode plot of both devices, showing that at high frequencies, both the phase angle and impedance approach zero. This behavior is consistent with earlier studies indicating a phase angle approaching -45 ° at lower frequencies, confirming the presence of pseudo capacitance [147]. Earlier research findings [148,149] have indicated that the presence of multiple peaks on the Bode angle plot serves as evidence for electrode materials with a layered structure. Hence, the presence of multiple peaks in the Bode curve indicates the layered structure of MXene samples, consistent with findings from a prior study [150]. The slopes of the Bode magnitude curves suggest capacitive behavior, closer to 0 at higher frequencies and -1 at lower frequencies, in close agreement with earlier findings [148,149].

Furthermore, Figure 3.12(f) presents the Galvanostatic Charge-Discharge (GCD) response of the LT-MXene/CS supercapacitor at a current density of 1 A g^{-1}, revealing

the performance over 10,000 charge-discharge cycles. Remarkably, the device retained 55.5% of its capacity after this extensive cycling, indicating good cycling stability.

Table 3.3. *Values of the modified-Randles equivalent circuit parameters obtained by fitting the Nyquist curves of LT-MXene supercapacitors fabricated with different separators.*

Electrode material	Randle equivalent circuit parameter					
	R_e (Ω)	Q_{ct} (S s^n)	R_{ct} (Ω)	W_b (S $s^{1/2}$)	R_s (Ω)	Q_s (S s^n)
LT-MXene/LGPS	22.18	1.51×10^{-5}	90	5.66×10^{-4}	108.3	1.39×10^{-6}
LT-MXene/CS	5.68	5.54×10^{-3}	1.07×10^{6}	0.16	39.52	7.16×10^{-7}

CV measurements were performed at various scan rates to thoroughly investigate the electrochemical behavior of the LT-MXene-based electrodes, in alignment with established methodologies from previous studies [151–154]. The results, illustrated in Figure 3.14, reveal distinct charge storage mechanisms for the two configurations. For LT-MXene/CS supercapacitors, the analysis indicates that charge storage is predominantly governed by surface-controlled processes, as suggested by the proportionality between peak current and scan rate. In contrast, LT-MXene/LGPS electrodes exhibit charge storage dominated by diffusion-controlled mechanisms, evident from the linear relationship observed in the plot of peak current versus the square root of the scan rate. These observations indicate a hybrid charge storage behavior, combining surface- and diffusion-controlled processes, highlighting the versatility and potential of LT-MXene electrodes for energy storage.

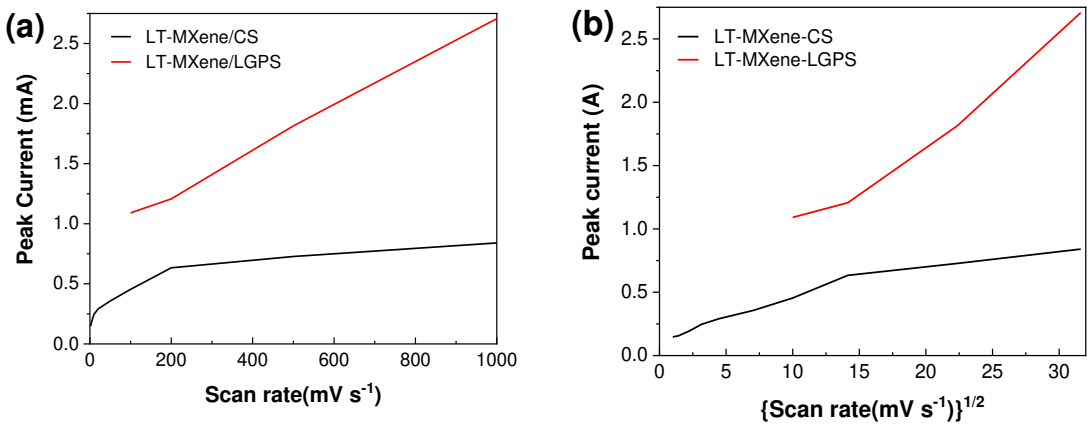

Figure 3.14. *Evaluation of peak current versus scan rate derived from CV curves at different scan rates for LT-MXene supercapacitors: (a) peak current vs. scan rate and (b) peak current vs. the square root of the scan rate for supercapacitors made with LT-MXene using LGPS and CS.*

3.4.2. Effects of mass loading on device performance

MXene samples with different thicknesses were generated to evaluate their performance as supercapacitor electrodes. For these evaluations, CS was chosen as the separator due to its wider scan range and stability. Figure 3.15 illustrates the outcomes of this assessment. As mentioned earlier, MXenes grown at 1150 °C (referred to as HT-MXenes) have an average thickness of 46.4 nm (mass loading of 0.043 mg cm^{-2}), which is thicker compared to MXenes grown at 1120 °C (known as MT-MXenes), with an average thickness of 44.8 nm (mass loading of 0.041 mg cm^{-2}).

Supercapacitors made with MT- and HT-MXene electrodes both exhibited CV curves with a quasi-rectangular shape, indicating predominant pseudo activity. Specifically, Figure 3.15(a) showcases the CV curve of supercapacitors using MT-MXene/CS electrodes. At a scan rate of 2 mV s^{-1}, the Specific Areal Capacitance (SAC) was measured at 22.9 mF cm^{-2} (556.7 F g^{-1}), which decreased to 1.1 mF cm^{-2} (27.8 F g^{-1}) at a scan rate of 1000 mV s^{-1}, providing a rate-stability of 29‰. In Figure 3.15(b), the CV curve of high-temperature MXene (HT-MXene) electrodes are depicted. Analysis of the CV data showed that these HT-MXene/CS electrodes at a scan rate of 2 mV s^{-1} exhibited an SAC of 39.5 mF cm^{-2} or 928.4 F g^{-1} Specific Gravimetric Capacitance (SGC). However, this value dropped to 1 mF cm^{-2} (23.6 F g^{-1}) with a rate capacity of 15‰ at higher scan rates. Table 3.4 presents detailed information on the capacitance values measured at various scan rates.

Figures 3.15(c-d) provide a detailed analysis of the EIS results obtained from MXene supercapacitors. Specifically, the MT-MXene/CS and HT-MXene/CS supercapacitors demonstrated distinct ESR values, measuring at 8.7 Ω and 5.1 Ω, respectively. For a comprehensive understanding of the circuit parameters, interested readers can refer to Table 3.5, which presents a comprehensive overview of other critical parameters associated with the equivalent circuits.

Delving deeper into the Bode plots displayed in Figure 3.15(d), it is evident that both devices' curves tend to zero impedance at higher frequencies, indicating a notable capacitive response. This observation aligns seamlessly with established literature [147], where the phase angle plots for these devices approach -45° at lower frequencies, further solidifying the presence of pseudo capacitance within the system. The intricate layered structure inherent in MXene samples is depicted through the multitude of peaks observed in the Bode curve in close agreement with earlier studies [150]. This signifies the complex

interplay of structural elements influencing the electrical behavior of these supercapacitors.

Moreover, the determination of a relaxation time constant ($\tau_0 = \frac{1}{2\pi f_0}$, with f_0 representing the frequency corresponding to a phase angle of -45°) of 0.95 seconds from the Bode plots adds a nuanced perspective to the capacitive behavior exhibited by the electrodes. This analytical approach follows a well-established methodology outlined in previous research [148,155,156], contributing to a deeper understanding of the dynamic response characteristics of supercapacitor devices. In essence, the devices under investigation showcase clear signs of capacitive behavior according to prior research [148,149], as evidenced by the distinct slopes of their Bode magnitude curves, which tend towards -1 at lower frequencies and 0 at higher frequencies. These nuanced insights gleaned from the EIS analysis offer valuable contributions to the ongoing research and development efforts in the field of energy storage and electrochemical devices.

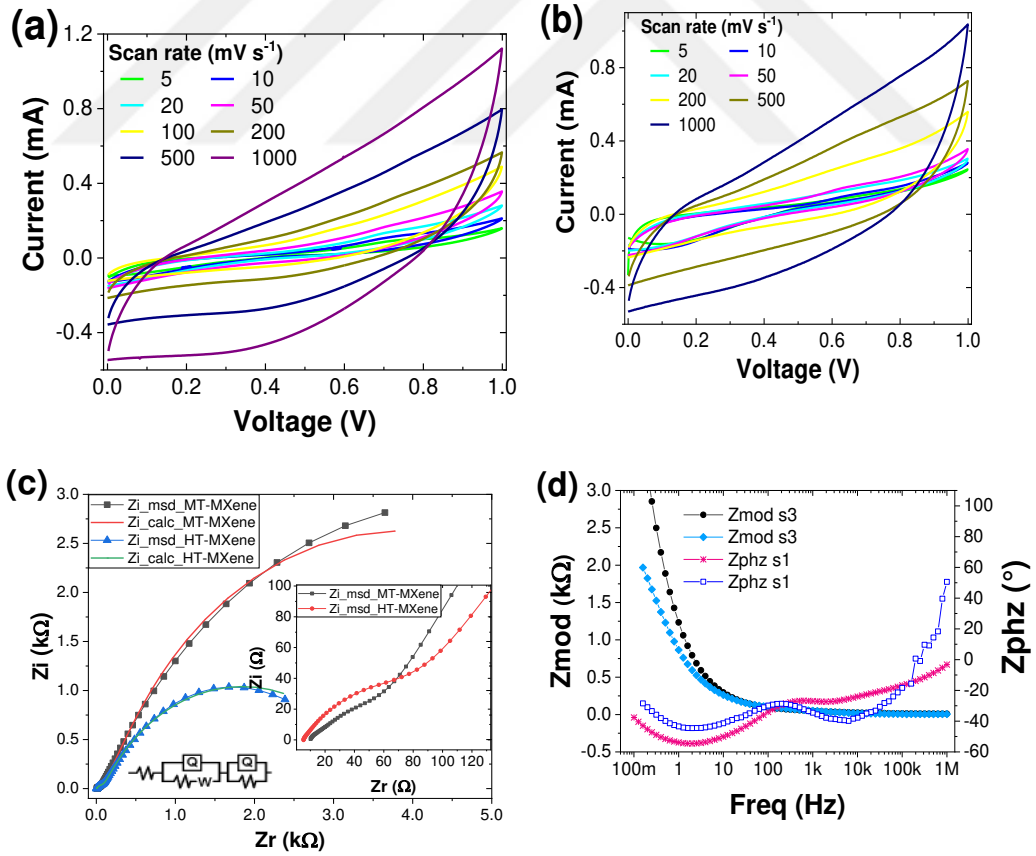

Figure 3.15. *Performance analysis showing (a) the CV curves of MT-MXene, (b) the CV curves of HT-MXene, (c) the Nyquist plot, and (d) the Bode plot from the EIS response of both devices.*

Table 3.4. *Specific capacitances of supercapacitors made with MT- and HT-MXene electrodes and CS.*

Scan rate	SAC (mF cm^{-2})		SGC (F g^{-1})	
(mV s^{-1})	MT-MXene	HT-MXene	MT-MXene	HT-MXene
5	22.42	37.03	545.12	872.43
10	14.13	19.12	343.58	450.56
20	8.86	13.49	215.49	317.75
50	5.46	5.96	132.84	140.49
100	4.33	----	105.27	----
200	3.68	3.42	89.42	80.60
500	2.89	2.63	70.32	62.06
1000	2.28	2.01	55.52	47.37

Table 3.5. *Results of fitting the Nyquist curves of MT- and HT-MXene supercapacitors with a modified Randles equivalent circuit.*

Electrode material	Randle equivalent circuit parameter					
	R_e (Ω)	Q_{ct} (S s^n)	R_{ct} (Ω)	W_b (S $s^{1/2}$)	R_s (Ω)	Q_s (S s^n)
MT-MXene	8.70	4.06 x 10^{-5}	0.17	2.59 x 10^{-4}	3.25 x 10^{-4}	115.1
HT-MXene	5.10	2.47 x 10^{-4}	3511	437.2	5.6 9x 10^{-5}	84.93

Figures 3.16(a-b) provide a comprehensive overview of the GCD results obtained from the supercapacitors under investigation. Specifically, Figure 3.16(a) presents the GCD performance of the HT-MXene/CS supercapacitor across various current densities. Notably, the device exhibited an impressive SGC of 442.6 F g^{-1} at a current density of 0.5 A g^{-1}. However, this SGC decreased significantly to 13.4 F g^{-1} at a higher current density of 10 A g^{-1}, indicating a notable reduction in capacitance under increased load conditions. Conversely, the GCD results of the MT-MXene/CS device are illustrated in Figure 3.16(b), revealing an SGC value of 252.4 F g^{-1}.

Figure 3.16(c) illustrates the GCD findings over 10,000 cycles for the MXene supercapacitors. Remarkably, both the LT-MXene/CS and HT-MXene/CS devices demonstrated considerable capacitance retention rates, measuring 55.8% and 85%, respectively, after the extensive cycling regimen. These retention rates provide valuable insights into the long-term stability and performance durability of the supercapacitors.

The reason why the observed retention is lower than 100%, can probably be rooted in the redox activity and MXenes' tendency to oxidize within aqueous electrolytes as

pointed out by prior research [38,89]. This oxidation process can lead to increased resistance and subsequent capacitance loss during cyclic operation.

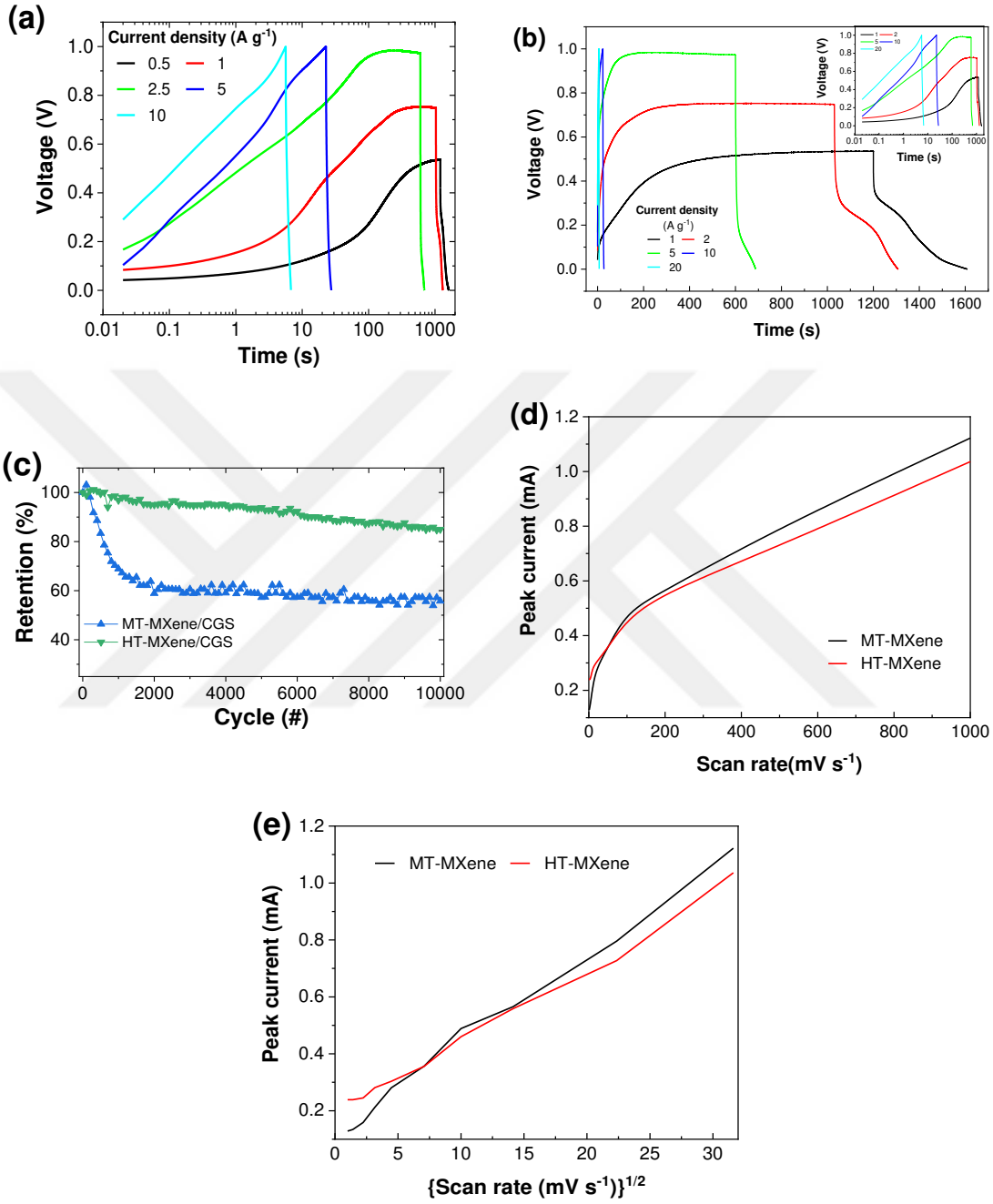

Figure 3.16. *GCD curves of (a) MT-MXene and (b) HT-MXene supercapacitors at various current densities, and (c) after 10,000 charge-discharge cycles. Results of CV analysis include (d) the plot of peak current versus scan rate and (e) the plot of peak current versus the square root of the scan rate for MT-MXene and HT-MXene supercapacitors.*

Furthermore, the substrate coverage of the two devices plays a pivotal role in their retention rates. MXenes with lower substrate coverage tend to expose more of the metallic

substrate to the aqueous electrolyte, facilitating irreversible reactions that degrade the device's performance over time. Essentially, the GCD results presented in Figures 3.16(a-b) offer valuable insights into the dynamic behavior, cycling stability, and performance attributes of MXene-based supercapacitors, providing a foundation for further exploration and optimization in energy storage technologies.

A comprehensive analysis of the CV results at varying scan rates was conducted to further examine the electrochemical behavior of MT- and HT-MXene-based electrodes, adhering to established methodologies from previous studies [151–154]. The findings, depicted in Figures 3.16(d-e), indicate that both configurations exhibit identical charge storage mechanisms. Specifically, the MT- and HT-MXene-based electrodes demonstrate charge storage predominantly governed by diffusion-controlled processes, as evidenced by the linearity in the plot of peak current versus the square root of the scan rate shown in Figure 3.16(e). These results suggest a hybrid charge storage mechanism that integrates both surface-controlled and diffusion-controlled processes, which are hallmarks of pseudo capacitive materials. This dual mechanism highlights the adaptability and promise of these MXene electrodes for advanced energy storage systems, offering a balance of rapid charge storage and robust capacity retention.

3.4.3. Effects of electrode coverage

In addition to evaluating the effects of separator and electrode mass loading on supercapacitor electrodes made with CVD MXenes, we also investigated the influence of substrate coverage on their performance. This exploration was motivated by the fact that MXenes typically do not exhibit 100% substrate coverage, and understanding this aspect can provide valuable insights into their electrochemical behavior. The results of this investigation are detailed in Figure 3.17, showcasing the impact of varying substrate coverage on the performance of MXene-based supercapacitors.

Figures 3.17(a-c) present the CV curves of the supercapacitors fabricated using MXenes with average substrate coverages of 70.2% and 71.4%, denoted as 70pcM and 71pcM devices, respectively. The estimation of MXene coverage was achieved by analyzing optical images obtained from more than nine distinct electrode sites, with the assistance of ImageJ software for accurate quantification. The distinctive duck-shaped CV curves of these devices reveal pronounced redox activity, particularly evident within the voltage range of 0.6 to 0.8 V.

At a scan rate of 2 mV s^{-1}, the SACs of the 70pcM and 71pcM devices were measured at 42.8 mF cm^{-2} (941.3 F g^{-1}) and 46.9 mF cm^{-2} (1040.7 F g^{-1}), respectively. Notably, the higher substrate coverage in the 71pcM device resulted in a slightly higher SAC, highlighting the impact of substrate coverage on capacitance performance. Moreover, the devices exhibited rate stabilities of 7.2% and 5.1% for the 70pcM and 71pcM configurations, respectively, indicating their ability to maintain capacitance levels across varying scan rates. An in-depth analysis of the electrochemical performance characteristics of the 70pcM and 71pcM supercapacitors under various experimental settings is provided in Table 3.6, which interested readers can consult for a more thorough understanding of the SACs at various scan speeds.

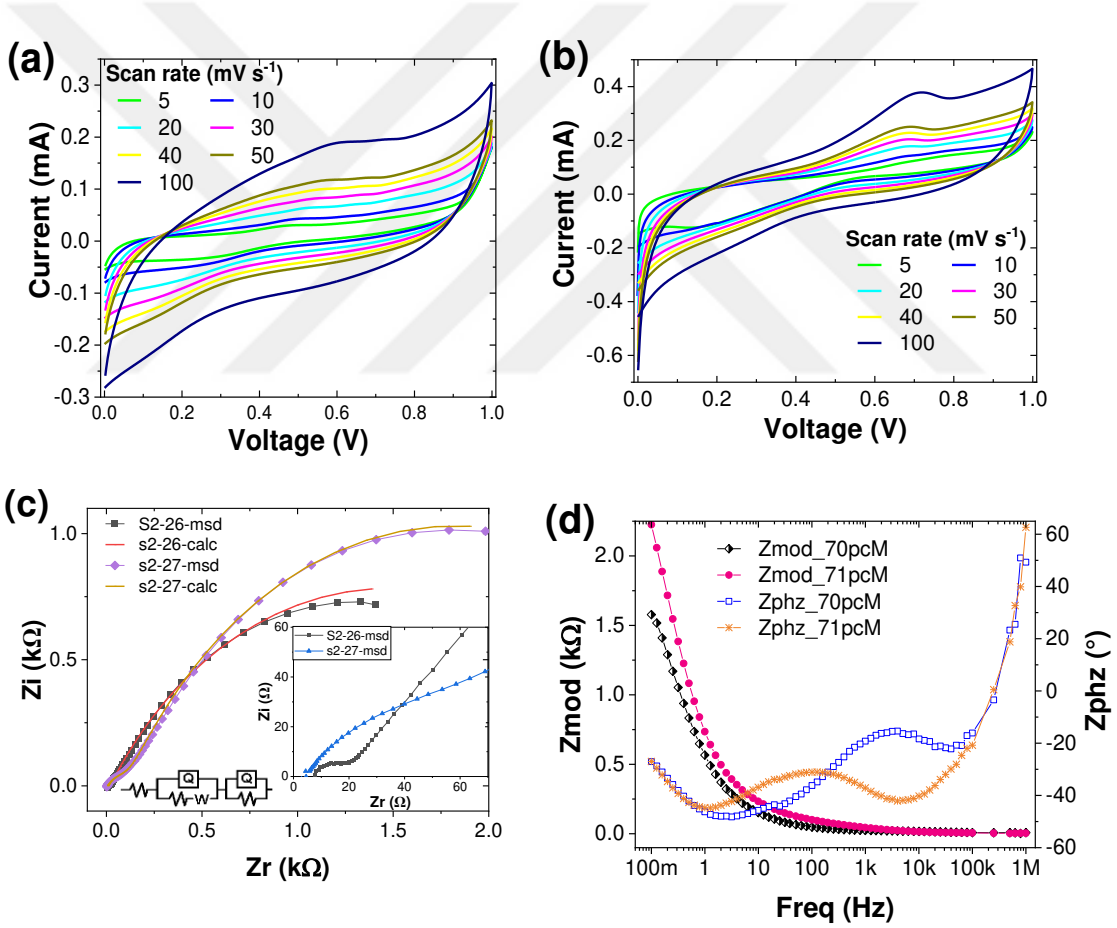

Figure 3.17. *Performance analysis of supercapacitors with different MXene coverages: CV curves of (a) 70% coverage and (b) 71% coverage supercapacitor electrodes, and EIS analysis showing (c) Nyquist and (d) Bode plots for the two devices.*

The EIS data from MXene-based supercapacitors are thoroughly analyzed in Figures 3.17(c-d). The Nyquist curves of the two devices, which highlight their impedance features, are shown in Figure 3.17(c). The Insets display the modified Randle

equivalent circuit and a close-up view of the Nyquist curve near the y = 0 axis. The devices demonstrated varying internal resistances, reflected in their Equivalent Series Resistances (ESRs) of 4.6 Ω and 12.0 Ω for substrate coverages of 70pcM and 71pcM, respectively. A detailed summary of additional fitting parameters, highlighting the electrochemical properties of these devices, is provided in Table 3.7.

The Bode graphs of the supercapacitors are shown in Figure 3.17(d), which spans a frequency range of 100 mHz to 1 MHz. Both devices' Bode phase angle plots show a phase angle that approaches -45 ° at lower frequencies, which is consistent with earlier research, [147] and supports the existence of pseudo capacitance in the system. Furthermore, the several peaks shown on the Bode curve, according to prior research [150] illustrate the intricate electrochemical behavior of MXene samples by indicating the layered structure that is intrinsic to the samples.

Table 3.6. *Specific capacitance data for MXene electrodes with varying coverage levels.*

Scan rate (mV s^{-1})	SAC (mF cm^{-2})		SGC (Fg^{-1})	
	70pcM	**71pcM**	**70pcM**	**71pcM**
2	40.09	42.80	941.26	1040.68
5	22.02	23.45	517.08	570.21
10	13.73	14.15	322.32	344.15
20	9.01	8.51	211.50	206.88
30	7.36	6.35	172.88	154.50
40	6.46	5.33	151.56	129.67
50	5.86	4.64	137.54	112.84
100	4.39	3.54	103.08	86.02

Table 3.7. *Modified Randles equivalent circuit parameters obtained by fitting the Nyquist curves of supercapacitors with MXene electrodes of varying coverage.*

Electrode material	Modified Randle equivalent circuit parameter					
	R_e (Ω)	Q_{ct} (S s^n)	R_{ct} (Ω)	W_b (S $s^{1/2}$)	R_s (Ω)	Q_s (S s^n)
70pcM	4.58	1.56×10^{-3}	1.59×10^{-3}	5.52×10^{-4}	7.25×10^{-4}	1.48×10^{4}
71pcM	12.04	5.01×10^{-4}	2839	1.07×10^{-2}	1.96×10^{-6}	7.07

The relaxation time constants, which measure 0.42 seconds for the 70pcM device and 0.56 seconds for the 71pcM device from their respective Bode graphs, provide more

information. This discrepancy highlights how substrate coverage affects the dynamic response properties of the supercapacitors by indicating a quicker rate of adsorption and desorption for the 70pcM configuration. The slopes of these devices' Bode magnitude curves, which approach 0 at higher frequencies and -1 at lower frequencies, further suggest the capacitive behavior of these devices following previous findings [148,149]. All things considered, the thorough examination given by Figures 3.17(c-d) provides insightful information about the dynamic behavior, impedance properties, and electrochemical performance of MXene-based supercapacitors, which furthers the continuous progress of energy storage technologies.

3.4.4. Comparison of results with the state-of-the-art

Given the significant interest in MXenes for their energy storage capabilities, extensive research has been dedicated to exploring their potential application in supercapacitors. Notably, Ghidiu et al. [82] conducted a study using $Ti_3C_2T_x$ as free-standing electrodes in a 1M H_2SO_4 electrolyte, achieving a SGC of 246 F g^{-1} at a scan rate of 2 mV s^{-1}, along with an impressive SVC of 910 F cm^{-3}. Similarly, another research group investigated free-standing V_2CT_x, achieving an outstanding SGC of 487 F g^{-1} at the same scan rate [157]. Tao et al. [158] reported an SGC performance of 339 F g^{-1} (equivalent to 1153 F cm^{-3}) using $Mo_{4/3}CT_x$ as supercapacitor electrodes at a scan rate of 2 mV s^{-1}. A comparative analysis of these previous results reveals that our devices exhibited superior performance. The remarkable outcomes of our investigation underscored the extraordinary performance of Mo_2C MXene, not only demonstrating its robust functionality but also showcasing its versatility in optimizing energy storage systems.

Furthermore, our research aligns with theoretical findings [39], confirming pristine MXenes as groundbreaking materials with the potential to revolutionize the supercapacitor technology landscape due to their unparalleled capabilities. This study contributes valuable insights into the ongoing advancements in MXene-based supercapacitors, paving the way for innovative developments in energy storage technologies.

3.4.5. Discussion and summary

Our study represents a journey into the realm of cutting-edge materials science, showcasing the synthesis of nonfunctional-group-terminated MXenes through advanced CVD techniques. We embarked on an extensive characterization adventure, employing a diverse array of spectroscopic and microscopic methods to unravel the mysteries of MXene's electrochemical prowess.

The fruits of our labor revealed intriguing patterns: as the synthesis temperature rose, both MXene coverage on the substrate and the thickness of MXene flakes experienced a proportional increase. Delving deeper, we subjected our MXene electrodes to rigorous testing as supercapacitors, immersing them in an aqueous electrolyte solution alongside the choice of separators, be it LGPS or CS.

The results? Nothing short of astonishing. Although still far from theoretical predictions, our devices showcased an exceptional SGC performance, especially when we explored the impact of increasing MXene's mass loading on its supercapacitor electrode functionality. Notably, our findings highlighted the superiority of higher coverage samples, echoing the sentiment that the MXene coverage area plays a pivotal role in enhancing performance.

Essentially, our research serves as a lighthouse highlighting the enormous potential of pure MXenes as competitive candidates for high-performance supercapacitor electrode materials. It creates opportunities for a day when cutting-edge materials research will support energy storage technology, leading to the development of effective and sustainable energy solutions.

3.5. Pristine MXenes as Supercapacitor Electrodes in Ionic Liquid Electrolytes

In the previous section, we discussed the performance of MXenes in aqueous electrolytes, where the operational voltage of supercapacitors is typically limited to ≤1 V. The equations $E = 1/2\ CV^2$ and $P = V^2/4R_{ES}$, respectively, define the specific energy (E) and power (P) of supercapacitors. The terms C, V, and R_{ES} stand for capacitance, voltage, and equivalent series resistance respectively. The internal resistance, R_{ES}, restricts how much power the capacitor can store and, consequently, how it can be used. These equations make it clear that the best way to increase the energy and power of supercapacitors is through the improvement of the operative voltage [159]. Ionic liquids

(ILs) may be able to improve the typical operation voltage of EDLCs in aqueous electrolytes, which is <= 1V.

ILs are a class of salts that exist in a liquid state at relatively low temperatures, often below 100 degrees Celsius. Unlike traditional salts that are typically composed of discrete ions, ionic liquids consist of large organic cations and organic or inorganic anions. This unique molecular structure gives them several interesting properties. ILs typically exhibit strong chemical and thermal stabilities, minimal vapor pressure, and are nonflammable [160,161]. ILs have drawn significant interest as "green" solvents due to these qualities, and they have most recently been thoroughly researched as electrolytes and/or electrolyte components in many electrochemical devices. Numerous investigations demonstrate that EDLCs with operative voltages significantly greater than 3 V can be realized by using electrolytes that contain ILs [162].

1-butyl-3-methyl-imidazolium tetrafluoroborate ([BMIM]BF_4) is one of the most used and commercially available IL electrolytes with an operating voltage >= 4V [163]. Triethyl sulfonium bis(trifluoromethyl sulfonyl)imide ((STFSI) ILs are relatively less viscous and have a lower melting point [164]. This study will be one of the first on the use of STFSI, a less-researched IL electrolyte, in supercapacitors.

3.5.1. Overview

The escalating demand for efficient and sustainable energy storage systems has propelled significant advancements in the development of next-generation supercapacitors. Distinguished by their superior power density, rapid charge-discharge cycles, and long operational lifetimes, supercapacitors have emerged as critical components in applications ranging from portable electronics to electric vehicles and grid stabilization systems [165–167]. However, their energy density remains a limiting factor compared to batteries, necessitating innovative strategies to bridge this gap.

Among the various approaches explored, two-dimensional (2D) transition metal carbides and nitrides, collectively known as MXenes, have garnered substantial interest as promising electrode materials [168–171]. As we have already seen, MXenes exhibit a unique combination of high electrical conductivity, tunable surface chemistry, and excellent mechanical properties, which collectively contribute to their exceptional electrochemical performance. Density functional theory calculations [39] have demonstrated that MXenes such as V_2C and Mo_2C possess staggering theoretical

capacitances of 3.4 mF cm^{-2} and 3.2 mF cm^{-2} respectively, demonstrating their enormous potential for supercapacitor applications.

MXenes are highly susceptible to oxidation in aqueous electrolytes, which increases resistance and causes significant capacitance decay during GCD analyses [38,89]. Consequently, selecting a suitable electrolyte is crucial for optimizing supercapacitor performance. Ionic liquids (ILs) have gained attention as promising alternatives to conventional aqueous and organic electrolytes due to their wide electrochemical stability window, low volatility, and tunable physicochemical properties [172,173]. These features enable IL-based supercapacitors to operate at higher voltages, directly enhancing energy densities, as the energy and power densities of a supercapacitor scale with the square of its operating potential [174]. Additionally, the interaction between MXenes and ILs offers exciting opportunities to refine the electrode-electrolyte interface, a key factor in realizing high-performance supercapacitors.

Optimizing the voltage window is a highly effective strategy for enhancing the energy density of supercapacitors. Consequently, extensive research has been conducted on the use of ionic liquids (ILs) in MXene-based supercapacitors due to their wide electrochemical stability and compatibility with advanced materials. For instance, Zifeng Lin et al. [175] reported that a $Ti_3C_2T_x$ ionogel film combined with the neat ionic liquid electrolyte 1-ethyl-3-methylimidazolium bis(trifluoromethyl sulfonyl)imide (EMI-TFSI) achieved a capacitance of 70 F g^{-1} within an impressive voltage window of 3 V at a scan rate of 20 mV s^{-1}. Similarly, another study [176] using $Ti_3C_2T_x$/graphene electrodes and the ionic liquid electrolyte 1-ethyl-3-methylimidazolium tetrafluoroborate ($EmimBF_4$) reported a specific capacitance (SCG) of 226 F g^{-1} at 1 A g^{-1} and an extended potential window of 3.2 V. Furthermore, Osti et al. [177] employed $Ti_3C_2T_x$ with a protic ionic liquid, 1-butyl-3-H-imidazolium bis(trifluoromethane sulfonyl)imide (BuIMH-NTf_2), and achieved a specific capacitance of approximately 154 F g^{-1} at a scan rate of 1 mV s^{-1}. A recent study by Dayakar and co-authors [178] highlighted the superior performance of a free-standing $Mo_2Ti_2C_3$ MXene electrode in 1 M 1-ethyl-3-methylimidazolium bis(trifluoromethyl sulfonyl)imide (EMIM-TFSI) in acetonitrile, demonstrating remarkable specific energy of 188 Wh kg^{-1}, specific power of 22 kW kg^{-1}, and a high specific capacitance of 152 F g^{-1}. These findings collectively underscore the potential of MXenes as highly promising electrode materials for supercapacitors, offering exceptional

capacitance, energy density, and voltage stability, particularly when paired with ionic liquid electrolytes.

This section explores the synergistic integration of nonfunctionalized MXene electrodes with various ionic liquid electrolytes to address the dual challenges of enhancing energy density and maintaining cycle stability. We focus on the synthesis and structural optimization of MXene electrodes, tailoring their physicochemical properties to maximize compatibility with ILs. By leveraging advanced characterization techniques and electrochemical analyses, we aim to provide insights into the underlying mechanisms driving performance improvements.

3.5.2. MXenes in [BMIM]BF_4 /AN electrolyte

To demonstrate the practical application of MXene electrodes in ionic liquid systems, we investigated their performance in a [BMIM]BF_4/acetonitrile (AN) electrolyte. The ionic liquid [BMIM]BF_4 was diluted with acetonitrile to prepare a 1M solution, which was then tested as the electrolyte with MXene-based electrodes. The resulting data are presented in Figure 3.18. The primary reason for using acetonitrile as a diluent was to reduce the viscosity of [BMIM]BF_4, enabling better ion mobility and improved electrochemical performance. Figure 3.18(a) shows the CV curves recorded for these MXene supercapacitors in [BMIM]BF_4/AN. Notably, the voltage window was confined to just 0.6 V, which is quite limited for an ionic liquid electrolyte. Such a narrow operational range undermines one of the key advantages of ionic liquids—namely, their ability to support wide electrochemical stability windows. This limitation strongly suggests potential issues, either with the electrolyte-electrode interface, the composition of the solution, or the stability of the MXene electrodes in the specific electrolyte environment. Further investigation is required to identify the exact cause.

The CV curves exhibit a characteristic duck shape, typically indicative of a redox-dominated charge storage mechanism. The symmetry observed in the curves reflects the structural and electrochemical uniformity of the electrodes, an important feature for energy storage systems. A specific capacitance of 54.7 mF cm^{-2} was calculated at a scan rate of 50 mV s^{-1}, demonstrating moderate performance. However, the CV profiles also show steep slopes, indicative of significant resistance within the system. This is a surprising observation, given the inherently high electrical conductivity of MXene materials, which should have minimized resistive losses. The presence of high resistance

in the system could arise from several factors. One possibility is insufficient ion-transport due to incomplete infiltration of the electrolyte into the porous MXene structure. Another potential issue could be surface passivation or the formation of resistive interfacial layers during cycling. Additionally, the dilution of [BMIM]BF_4 with acetonitrile may have altered the electrolyte's ionic strength or conductivity, contributing to the observed performance discrepancies.

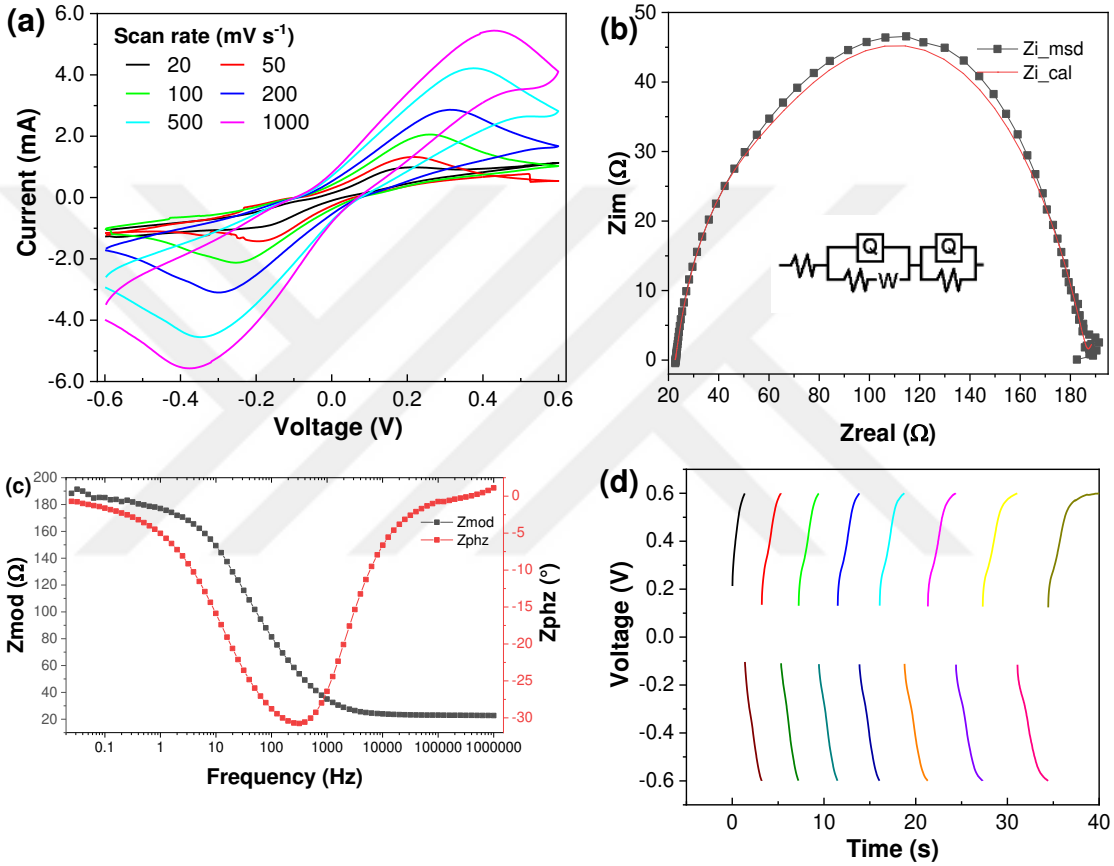

Figure 3.18. *Electrochemical analysis results showing: (a) the cyclic voltammetry, (b) the Nyquist response, (c) the Bode response, and (d) the GCD response of the MXene supercapacitors in [BMIM]BF_4-AN ionic liquid electrolyte.*

3.5.3. MXene supercapacitors in STFSI /AN IL electrolyte

Another electrolyte that was examined with MXene electrodes was 1M STFSI/AN. The electrochemical performance of MXene-based supercapacitors in a 1M STFSI/AN ionic liquid electrolyte is presented in Figure 3.19. The cyclic voltammograms in Figure 3.19(a) exhibit characteristic duck shapes, indicative of a redox-dominated energy storage mechanism. The symmetry of the CV curves reflects the structural uniformity and electrochemical balance of the electrodes. At a scan rate of 50 mV s^{-1}, the

device achieves a specific capacitance of 51.6 F cm^{-2}, showcasing its moderate energy storage capability.

However, similar to the observations with the [BMIM]BF_4 electrolyte, the CV curves exhibit steep slopes, indicative of high resistance within the active materials. This is inconsistent with the inherent high electrical conductivity of MXenes, suggesting potential issues such as suboptimal electrode architecture, incomplete ion penetration into the MXene layers, or interfacial resistance at the electrode-electrolyte boundary. Additionally, the operating voltage window is restricted to just 0.6 V, which limits the full potential of the ionic liquid electrolyte and warrants further investigation to identify the cause of this constraint.

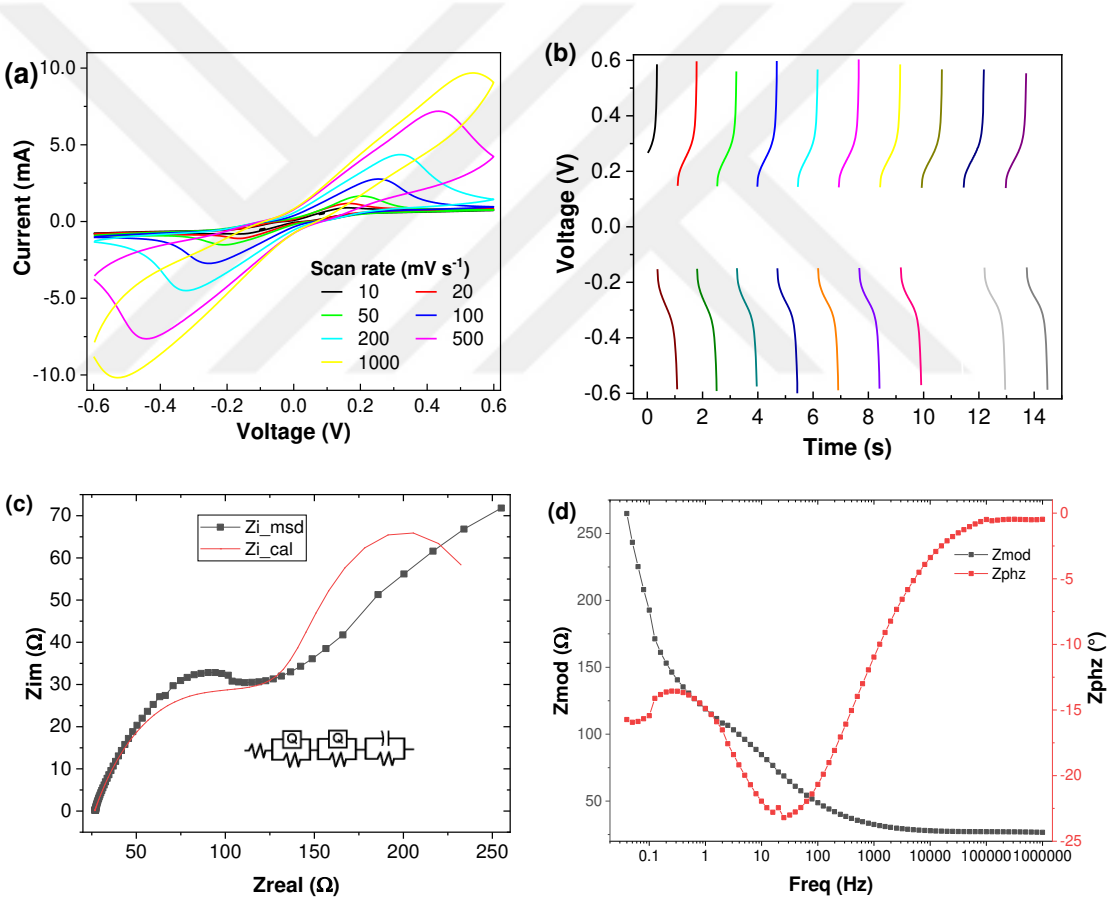

Figure 3.19. *Electrochemical analysis results showing: (a) the cyclic voltammetry, (b) the Nyquist response, (c) the Bode response, and (d) the GCD response of the MXene supercapacitors in STSFI-AN ionic liquid electrolyte.*

The Nyquist plot in Figure 3.19(b) provides additional insights into the impedance characteristics, yielding an ESR of 25 Ω. This relatively high ESR may further contribute to the observed limitations in the device's electrochemical performance. The GCD

response at a constant current of 5 mA is shown in Figure 3.19(d). Similar to the behavior observed with the [BMIM]BF_4 electrolyte, the discharge curves reveal significant self-discharge, with the voltage dropping abruptly from 0.6 V to 0 V. This indicates significant energy losses and further highlights the need for optimization in the electrolyte composition, device fabrication, or testing conditions to address these issues.

3.5.4. MXene supercapacitors in [BMIM]BF_4 IL electrolyte

The results discussed earlier revealed a significant limitation in the voltage window, failing to meet the expected performance benchmarks for ionic liquid electrolytes. This issue observed consistently across both tested electrolytes, suggests that the underlying problem may not lie with the ionic liquids themselves but rather with a shared component-acetonitrile. Its use as a solvent in both cases raises concerns about its impact on the operational voltage window. To investigate this hypothesis, MXene electrodes were tested in [BMIM]BF_4 without acetonitrile, using a filter paper and celgard separator.

3.5.4.1. Using filter paper separator

Recognizing the critical role of the separator in determining supercapacitor performance, this section examines the behavior of MXene electrodes paired with filter paper soaked in [BMIM]BF_4 IL electrolyte. To simulate real-world application conditions, the devices were tested both immediately after assembly and following a rest period.

Allowing supercapacitors to rest before testing is essential for achieving reliable and optimal performance. During this period, the electrolyte fully permeates and saturates the porous electrodes, enhancing ionic contact and mitigating the risk of incomplete wetting. This resting phase also stabilizes the interfaces between the electrolyte and electrodes, reducing transient effects from the fabrication process. Additionally, it dissipates mechanical stresses introduced during assembly and allows residual solvents or gases to evaporate, minimizing their influence on performance. Moreover, the resting period enables ions within the electrolyte to diffuse and settle into equilibrium positions within the electrode material, improving charge transport and electrochemical kinetics. By mimicking practical storage conditions, this approach provides valuable insights into

the long-term stability of the supercapacitor, ensuring more consistent and representative performance metrics.

Performance analysis of the device tested immediately after fabrication

Figure 3.20(a) presents the linear sweep voltammetry (LSV) results for the MXene supercapacitors using [BMIM]BF_4 IL electrolyte, with the voltage sweep ranging from -2 to 3 V. The LSV data demonstrates that these devices can achieve a wide voltage window of up to 4 V. Figure 3.20(b) illustrates the CV results obtained by progressively increasing the voltage window from 0.5 to 2.5 V. These measurements indicate that the voltage window can only be extended to a maximum of 2.2 V, beyond which electrolyte degradation occurs, evidenced by a sharp cusp in the CV curve beyond this threshold. This improved voltage window suggests that AN could have been the cause of the decrease seen in the previous sections.

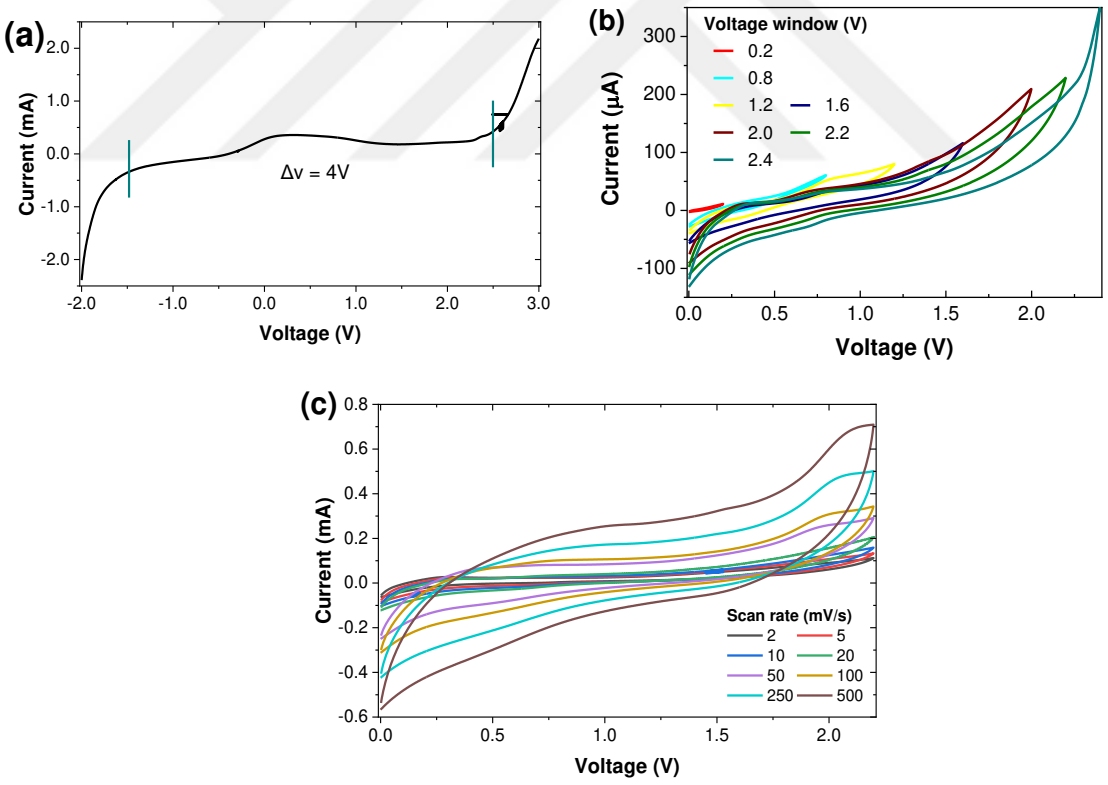

Figure 3.20. *Electrochemical analysis of MXene supercapacitors in [BMIM]BF_4, including (a) Linear sweep voltammetry, (b) Cyclic voltammetry with varying potential windows, and (c) Cyclic voltammetry at different scan rates.*

Figure 3.20(c) shows the CV profiles at varying scan rates. The curves exhibit near-rectangular or leaf-like shapes, characteristic of a predominantly non-faradaic

energy storage mechanism. From these CV curves, the SAC and SGC values were calculated, with the results summarized in Table 3.8. At a scan rate of 2 mV s^{-1}, the devices exhibit a SAC of 23.4 mF cm^{-2}, corresponding to an SGC of 549.6 F g^{-1}. When the scan rate is increased to 100 mV s^{-1}, the SGC decreases to 66.5 F g^{-1}, indicating a rate stability of 12.1%. These findings highlight the trade-off between capacitance retention and scan rate, a critical consideration for optimizing supercapacitor performance.

The EIS and GCD analyses of the MXene-based supercapacitors are presented in Figure 3.21, providing valuable insights into their electrochemical properties. Figure 3.21(a) shows the Nyquist curve, which has been fitted using a Randles equivalent circuit model. From this fitting, the ESR is determined to be 12.8 Ω, highlighting the low resistance of the device. Additionally, the Warburg diffusion element, indicative of ion-transport resistance within the electrolyte and electrode interface, is calculated as 1.9×10^{-4} S $s^{1/2}$. The charge transfer resistance, which represents the resistance to faradaic reactions at the electrode-electrolyte interface, is found to be 52.1 Ω. Furthermore, the constant phase element (CPE), reflecting the capacitive behavior of the device, is measured at $5.2x10^{-5}$ S s^{n}.

Figure 3.21(b) presents the Bode plot of the device, recorded across a frequency range from 10 mHz to 1 MHz. The Bode phase plot reveals a relaxation time of 0.002 s, calculated as the inverse of the frequency at which the phase angle reaches −45°. This short relaxation time signifies rapid charge-discharge kinetics, underscoring the supercapacitor's ability to deliver energy efficiently at high frequencies. Together, these results confirm the excellent electrochemical properties of the MXene supercapacitors, including their low resistance, efficient ion-transport, and fast electrochemical response, making them highly suitable for high-performance energy storage applications.

Figure 3.21(c) presents the GCD results of the device measured at current densities ranging from 1 A g^{-1} to 10 A g^{-1}. The data reveal a noticeably longer charging time compared to the discharge time, indicating lower coulombic efficiency at lower current densities. This discrepancy diminishes progressively as the current density increases. From the discharge curve at 1 A g^{-1}, an SGC of 111 F g^{-1} is calculated. The SGC values at other current densities are summarized in Table 3.8, highlighting the device's rate performance.

Figure 3.21(d) illustrates five consecutive GCD cycles performed at a current density of 10 A g^{-1}. A sudden voltage drop of approximately 0.5 V is observed during the

discharge process, attributed to the self-discharge behavior of the device. Additionally, it is noteworthy that the device exhibits an intrinsic potential of ~0.6 V, as evidenced by the charging curves starting from this voltage. This intrinsic potential underscores the unique electrochemical properties of the device, contributing to its overall performance.

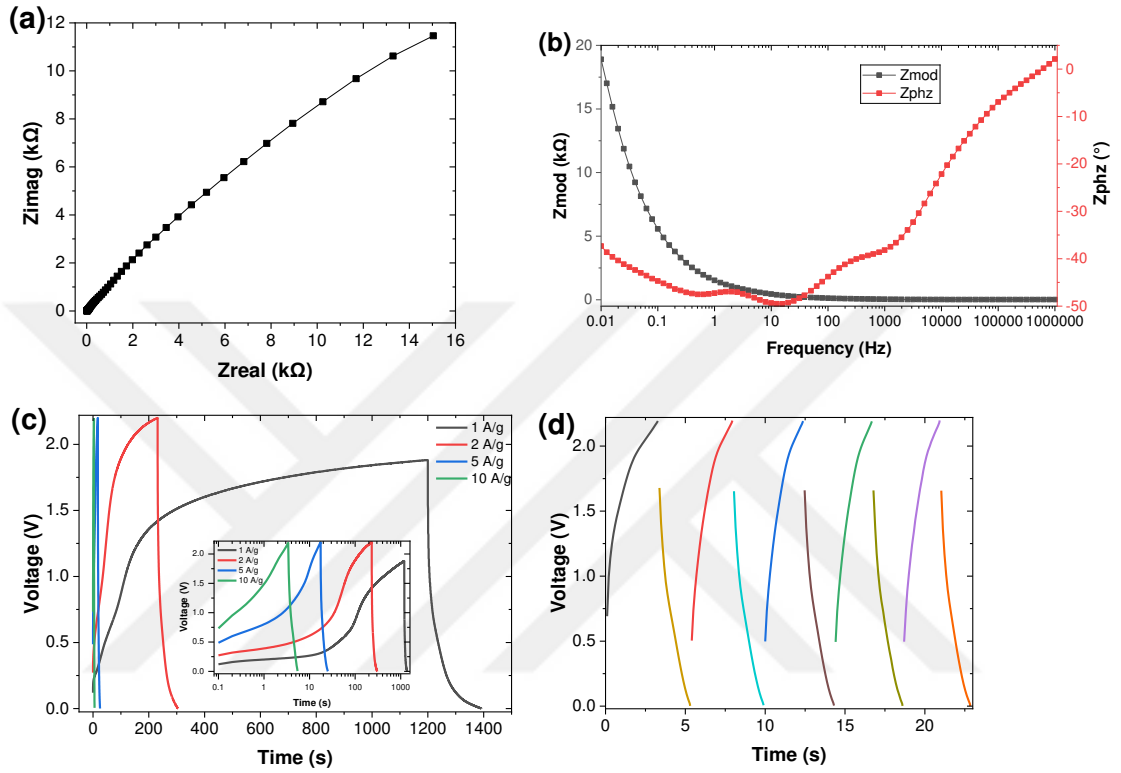

Figure 3.21. *The electrochemical analysis of MXene in BMIMBF$_4$ electrolyte including (a) the Nyquist curve (b) the Bode plot, (c) the GCD results at varying current density, and (d) the GCD results showing 5 consecutive charge-discharge cycles at a current density of 10 A g^{-1}.*

Table 3.8. *Capacitances of the supercapacitors made with MXene electrodes in [BMIM]BF$_4$ electrolyte at different scan rates and current densities.*

Capacitance from CV curves			
Scan rate (mV s^{-1})	**SAC (mF cm^{-2})**	**SGC (F g^{-1})**	**SVC (F cm^{-3})**
2	23.39	549.56	5044.59
5	11.76	276.37	2536.95
10	6.85	160.82	1476.20
20	4.38	102.92	944.70
50	4.40	103.32	948.41
100	2.83	66.49	610.37
250	1.81	42.49	390.00
500	1.33	31.16	286.0

Table 3.8 (Continued)

Capacitances from discharge curves		
Current density (A g^{-1})	**SGC (F g^{-1})**	**SVC (F cm^{-3})**
1	111.01	1019.11
2	73.12	671.23
5	21.24	195.01
10	12.28	112.75

Performance analysis of the device tested after over 12 hours of rest period

Figure 3.22 presents the analysis results of MXene electrodes tested in [BMIM]BF_4 IL electrolyte after a resting period of over 12 hours. The CV results obtained by varying the voltage window, shown in Figure 3.22(a), indicate that a potential window of 2.2 V is achievable, consistent with the results observed in the immediate testing scenario. Figure 3.22(b) illustrates the CV curves recorded at different scan rates. An SGC of 865.9 F g^{-1} is calculated from the CV curve at a scan rate of 2 mV s^{-1}, representing a substantial 58% increase in capacitance compared to the values obtained from tests conducted immediately after fabrication. The capacitance values corresponding to other scan rates are detailed in Table 3.9. Notably, the cusp observed around 2 V in the CV curve of the immediate test results is absent in the tests conducted after the rest period, suggesting improved electrochemical stability. This improvement highlights the significant impact of the resting period on the electrochemical performance of the supercapacitors.

Figure 3.22(c) displays the Randles-fitted Nyquist curve, from which an ESR of 18.7 Ω is calculated, slightly higher than the 12.8 Ω observed in the immediate test case. The Warburg diffusion element, calculated as 1.7×10^{-4} S $s^{1/2}$, and the CPE, 6×10^{-5} S s^n, remain largely consistent with the previous results. However, a significant increase in charge transfer resistance (R_{ct}) is observed, rising from 52 Ω in the immediate test to 2.5 kΩ after the rest period. The observed increase in ESR may be attributed to minor degradation of the electrolyte or alterations in the electrode-electrolyte interface properties during the resting period, potentially hindering ion-transport, as reported in previous studies [179–181]. Similarly, the significant rise in R_{ct} could be associated with the development of a more stable yet resistive passivation layer on the electrode surface, as highlighted in prior work [182]. This phenomenon likely arises from prolonged

interactions between the MXene and the ionic liquid. Furthermore, extended exposure to ambient conditions may have induced slight oxidation or surface contamination, thereby exacerbating the resistance values.

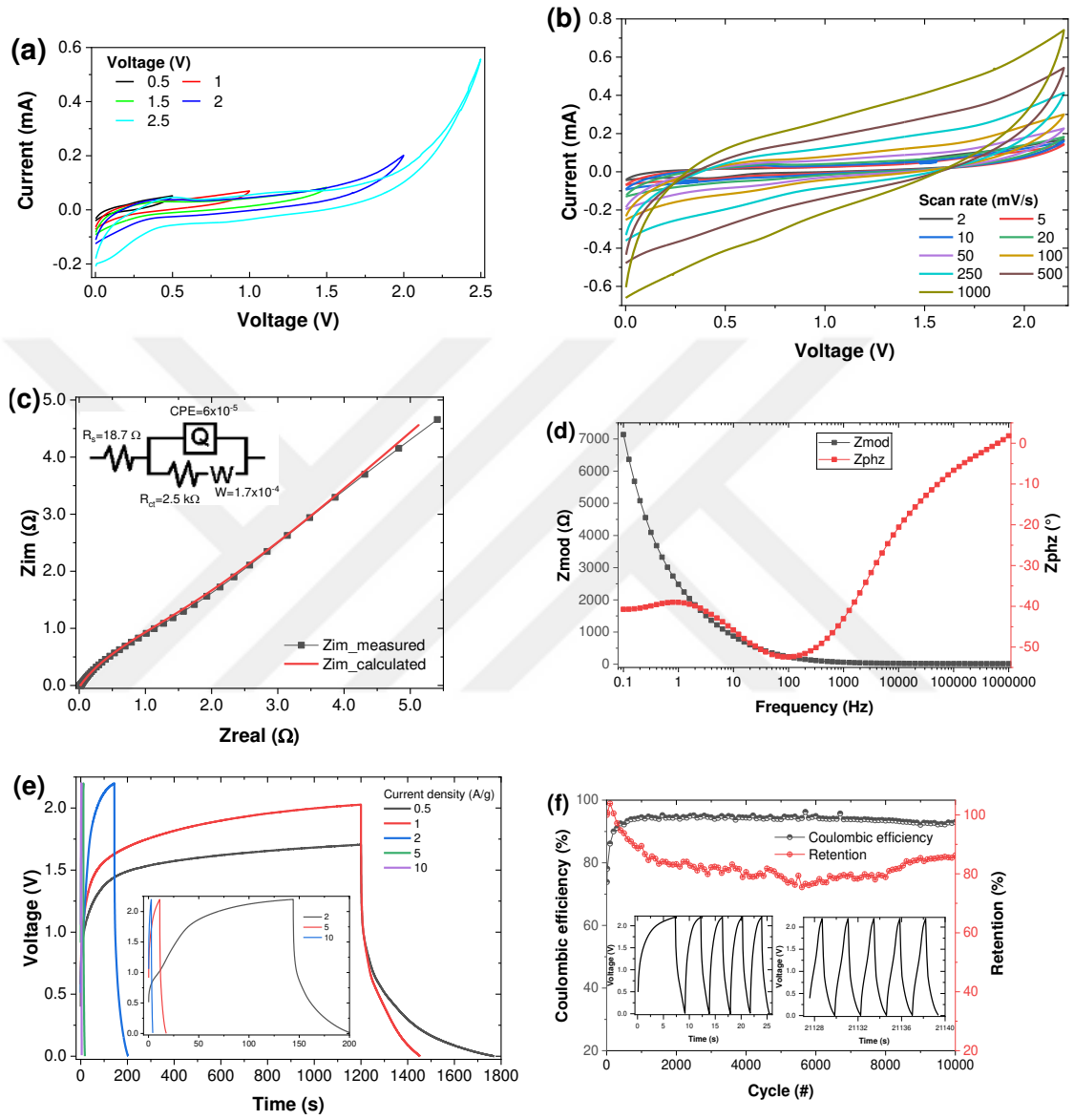

Figure 3.22. *Performance analysis of MXene in [BMIM]BF_4 ionic liquid (IL) after a ~12-hour rest period, including (a) CV results from a voltage sweep, (b) CV curves from a scan rate sweep, (c) Nyquist curves fitted with the Randles equivalent circuit, (d) Bode plot, (e) GCD results at varying current densities, and (f) GCD results showing capacitance retention and coulombic efficiency over 10,000 cycles.*

Figure 3.22(d) presents the Bode plot, illustrating both the impedance and phase behavior of the device. The Bode impedance curve approaches zero at high frequencies, confirming the capacitive nature of the supercapacitor. The Bode phase curve exhibits multiple peaks, indicative of the layered structure of the MXene electrode material. From

the phase curve, a relaxation time of 0.002 s like in the immediate test case is calculated, reflecting the rapid ion-transport and charge storage dynamics within the system.

Figure 3.22(e) shows the GCD analysis results obtained at varying current densities ranging from 0.5 A g^{-1} to 10 A g^{-1}. Like the immediate test case, the charging time is notably longer than the discharging time, resulting in a coulombic efficiency (CE) of 50% at 0.5 A g^{-1}, which improves to 60% at 10 A g^{-1}. The long-term performance of the device, including retention rate and CE over 10,000 GCD cycles, is illustrated in Figure 3.22(f). The MXene electrodes exhibit a retention rate of 86.3%, marking a slight improvement compared to the 85% performance in aqueous electrolytes. The CE starts at 72%, rapidly increases to 93% within the initial cycles, and remains stable near this value throughout the 10,000 cycles, demonstrating robust cycling stability.

Table 3.9. *Capacitances MXene electrodes in [BMIM]BF_4 electrolyte at different scan rates and current densities, as well as Nyquist fit parameters.*

Capacitance from CV analyses			
Scan rate (mV s^{-1})	**SAC (mF cm^{-2})**	**SGC (F g^{-1})**	**SVC (F cm^{-3})**
2	36.86	865.90	7948.39
5	14.37	337.55	3098.46
10	8.82	207.19	1901.84
20	5.66	132.88	1219.80
50	3.34	78.39	719.60
100	2.31	54.25	497.97
250	1.49	34.92	320.57
500	1.10	25.94	238.12
1000	0.84	19.64	180.24

Capacitance from GCD analyses		
Current density (A g^{-1})	**SGC (F g^{-1})**	**SVC (F cm^{-3})**
0.5	179.74	1649.99
1	137.85	1265.50
2	62.09	569.97
5	19.8	181.75
10	7.58	69.59

Nyquist fit parameters			
R_s (Ω)	**R_{ct} (Ω)**	**CPE**	**W_b**
18.7	2520	1.65×10^{-4}	6.04×10^{-5}

3.5.4.2. Using celgard separator

Recognizing the critical role of the separator in influencing supercapacitor performance, we conducted additional tests on the MXene electrodes using a Celgard separator soaked in [BMIM]BF_4 IL electrolyte. These tests were performed both immediately after fabrication and following a rest period of over 12 hours to further validate the significance of resting time in ensuring accurate and reliable measurements.

Electrochemical analysis of devices tested immediately upon fabrication

Figure 3.23 presents the electrochemical performance of supercapacitors fabricated with MXene electrodes and a Celgard separator soaked in [BMIM]BF_4 IL electrolyte. The voltage-sweep CV curves shown in Figure 3.23(a) demonstrate that a stable voltage window of up to 2.2 V is achievable with this configuration. This window aligns with results observed in similar studies [183–186], showcasing the compatibility of the electrode and electrolyte system.

The rate-sweep CV curves in Figure 3.23(b) exhibit leaf-like shapes, characteristic of a hybrid energy storage mechanism combining faradaic and non-faradaic processes. Notably, pseudo capacitive peaks are visible at approximately 1.6 V and 2.1 V at a scan rate of 1 V s^{-1}, indicative of surface redox reactions contributing to charge storage. These peaks suggest the involvement of reversible electrochemical processes in addition to electric double-layer capacitance, emphasizing the hybrid nature of the system.

At a scan rate of 2 mV s^{-1}, a SAC of 10.8 mF cm^{-2}, corresponding to a SGC of 253 F g^{-1}, was achieved. This represents a significant improvement over some aqueous-based systems, highlighting the potential of the ionic liquid electrolyte. Detailed capacitance values at other scan rates are summarized in Table 3.10, providing a comprehensive understanding of the rate-dependent performance.

The EIS analysis results of the devices are presented in Figure 3.23. Specifically, Figure 3.23(c) illustrates the Nyquist curve, while Figure 3.23(d) depicts the Bode plot. The Nyquist curve is fitted using a modified Randles equivalent circuit, as shown in the Inset of Figure 3.23(d). From the fitting, an ESR of 16.5 Ω is calculated, which is slightly higher than the 12.8 Ω obtained when using a filter paper separator. This increase in ESR could be attributed to differences in ionic conductivity and interface resistance associated with the separators. The extracted values for other circuit parameters are summarized in Table 3.10, providing additional insights into the electrochemical behavior of the devices.

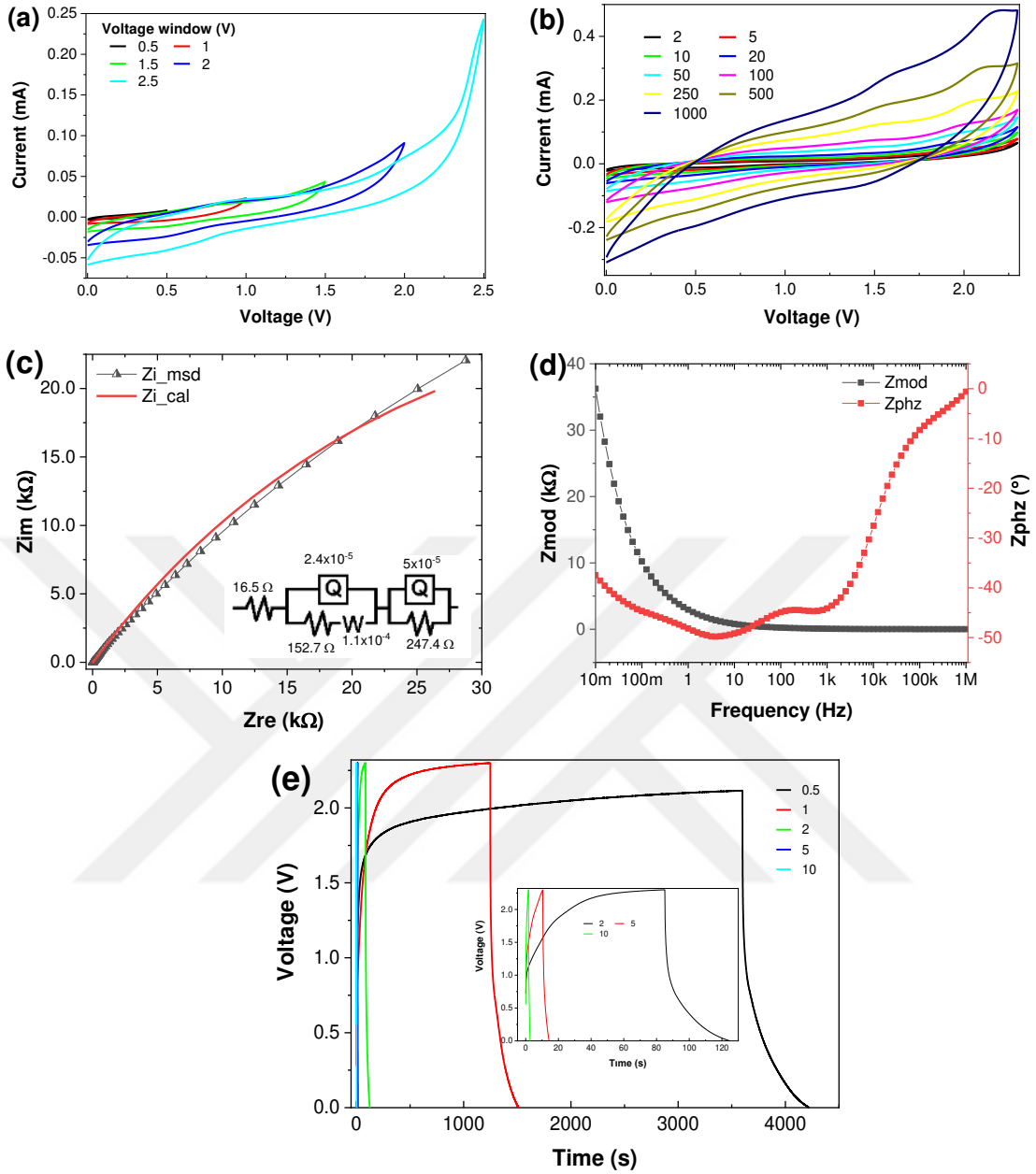

Figure 3.23. *Electrochemical performance of supercapacitors with MXene electrodes and a Celgard separator soaked in [BMIM]BF_4, tested immediately after fabrication, including: (a) CV curves showing the effect of varying the voltage window, (b) CV curves at different scan rates, (c) the Nyquist plot fitted with a modified Randles equivalent circuit model (inset), (d) the Bode plot, and (e) GCD curves at current densities ranging from 0.5 A g^{-1} to 10 A g^{-1}.*

The Bode magnitude plot, also shown in Figure 3.23(d), demonstrates a characteristic behavior of capacitors, with the impedance approaching zero at high frequencies and diverging toward infinity at low frequencies. Such behavior indicates efficient charge storage at varying frequencies. Furthermore, the Bode phase angle plot reveals multiple distinct peaks, suggesting the presence of multiple relaxation processes. This is consistent with the layered morphology and intrinsic properties of the synthesized

MXene structures. From the Bode phase angle plot, two relaxation times were determined: 1.35 s and 1.69 ms, corresponding to frequencies (f_0) of 0.127 Hz and 93.87 Hz, respectively. These relaxation times highlight the dynamic electrochemical response of the material across a wide frequency range. The presence of multiple relaxation times further corroborates the structural complexity and layered configuration of the MXenes, which contribute to their promising capacitive performance.

Table 3.10. *Performance results of supercapacitors utilizing MXene electrodes, a Celgard separator infused with [BMIM]BF_4 ionic liquid electrolyte, tested immediately after assembly. The figure includes capacitance values derived from CV curves, discharge profiles, and parameters obtained from Nyquist curve fitting.*

Capacitance from CV analyses			
Scan rate (mV s^{-1})	**SAC (mF cm^{-2})**	**SGC (F g^{-1})**	**SVC (F cm^{-3})**
2	10.77	253.07	2323.03
5	6.61	155.36	1426.14
10	4.49	105.50	968.46
20	3.09	72.53	665.79
50	1.91	44.95	412.60
100	1.34	31.56	289.66
250	0.86	20.11	184.61
500	0.62	14.62	134.17
1000	0.45	10.62	97.44
Capacitance from GCD analyses			
Current density (A g^{-1})	**SGC (F g^{-1})**	**SVC (F cm^{-3})**	
0.5	157.36	1444.54	
1	125.07	1148.16	
2	39.41	361.74	
5	10.71	98.34	
10	4.80	44.03	
Nyquist fit parameters			
R_s (Ω)	**R_{ct} (Ω)**	**CPE**	**W_b**
16.5	705	2.4×10^{-5}	1.1×10^{-4}

The GCD results at varying current densities are presented in Figure 3.23(e), showcasing the charge-discharge behavior of the device under different conditions. From these results, the SGCs are calculated using the discharge curves. At a low current density

of 0.5 A g^{-1}, the device exhibits an impressive SGC value of 157.4 F g^{-1}, highlighting its potential for energy storage applications. However, as the current density is increased to 10 A g^{-1}, the SGC drops sharply to 4.8 F g^{-1}, reflecting a substantial reduction in charge storage capacity at higher rates. This translates to a rate stability of only 3%, indicating that the device faces significant challenges in retaining performance under rapid charge-discharge cycles.

Such behavior could be attributed to diffusion limitations and increased resistance at higher current densities, which hinder the efficient utilization of the electrode material. Despite this limitation, the initial high capacitance demonstrates the suitability of the MXene-based electrodes for low-rate applications. A comprehensive overview of the device's performance metrics, including capacitance values, rate capability, and other parameters, is provided in Table 3.10 for further analysis and comparison.

Electrochemical analysis of devices tested after over 12 hours of rest time

Figure 3.24 presents the electrochemical analysis results of supercapacitors fabricated with MXene electrodes, a Celgard separator, and [BMIM]BF_4 IL electrolyte, tested after a rest period exceeding 12 hours. The LSV results in Figure 3.24(a) reveal that a potential window of 4 V is achievable, similar to the performance observed with a filter paper separator. The CV curves at varying scan rates, presented in Figure 3.24(b), display characteristic leaf-like morphologies, indicative of a faradaic, non-diffusion-limited energy storage mechanism, as previously demonstrated by Schoetz et al. [74]. From the CV data, a SGC of 428 F g^{-1} is calculated at a scan rate of 2 mV s^{-1}, which demonstrates an improvement compared to the immediate test results. This finding aligns with trends observed in previous rest-period tests, reaffirming the importance of rest time in enhancing capacitance.

However, it is worth noting that the SGC of 866 F g^{-1} achieved using a filter paper separator is more than double the 428 F g^{-1} obtained with the Celgard separator. This significant difference can be attributed to the better compatibility of the filter paper's large pore sizes with the large ionic dimensions of the [BMIM]BF_4 IL, facilitating improved ion-transport and accessibility to the MXene electrode surface.

The EIS analysis was conducted over a frequency range of 10 mHz to 1 MHz. The Nyquist curve, shown in Figure 3.24(c), was fitted using a modified Randles equivalent circuit model. An ESR of 15.4 Ω was calculated, reflecting a slight decrease compared to

the 16.5 Ω observed in the immediate test case. Interestingly, this result contrasts with the behavior observed when using a filter paper separator, where the ESR increased from 12 Ω to 18 Ω after a rest period. A potential explanation for this discrepancy lies in the differing properties of the separators, particularly the lower wettability of Celgard compared to filter paper. Due to its hydrophobic nature, Celgard often requires extended soaking in the electrolyte (at least one day) to ensure thorough impregnation and optimal ionic conduction. In contrast, the highly porous and hydrophilic nature of filter paper facilitates quicker and more uniform electrolyte absorption, potentially leading to a different interaction with the electrode surface and overall device impedance. The diffusion constants are comparable in magnitude-1.7×10^{-7} S $s^{1/2}$ for the filter paper and 1.4×10^{-4} S $s^{1/2}$ for the Celgard separator-indicating that ion diffusion in the electrolyte is similarly efficient in both configurations.

The Bode plot in Figure 3.24(d) displays the magnitude and phase responses across the frequency range 10 mHz – 1 MHz. The Bode magnitude curve trends towards infinity at low frequencies, indicating resistive behavior, and approaches zero at higher frequencies, reflecting capacitive characteristics. The Bode phase plot reveals two distinct relaxation times, calculated as 3.65 s at low frequencies and 0.012 s at high frequencies, corresponding to different time scales of ion diffusion and charge transfer within the system.

Figure 3.24(e) presents the GCD results obtained at varying current densities. The device demonstrates an SGC of 182 F g^{-1} at a current density of 0.5 A g^{-1}, with the results at other current densities summarized in Table 3.11. Figure 3.24(f) illustrates the GCD performance over 10,000 cycles, showing an impressive retention rate of 98% and a CE of 94%. This exceptional retention rate surpasses the 86% observed with the filter paper separator. The likely explanation lies in the contrasting behavior of ESRs, suggesting that the interactions between the MXene electrode, IL electrolyte, and Celgard separator are more stable and inert compared to those involving the filter paper separator.

Overall, a detailed comparison between the devices assembled with filter paper and Celgard separators reveals distinct advantages and drawbacks associated with each configuration. The filter paper-based device demonstrates a significantly higher capacitance compared to the Celgard-based device, highlighting its superior charge storage capacity. However, the Celgard-based device excels in terms of long-term stability, as it shows remarkable durability and outperforms the filter paper device in

terms of performance retention over extended cycles. This suggests that while the filter paper-based device offers better immediate energy storage, the Celgard-based device may provide more reliable performance over time. Notably, the CE for both devices is quite similar, with the filter paper device achieving 93% and the Celgard device slightly outperforming it at 94%, indicating that both configurations maintain high efficiency throughout their operation.

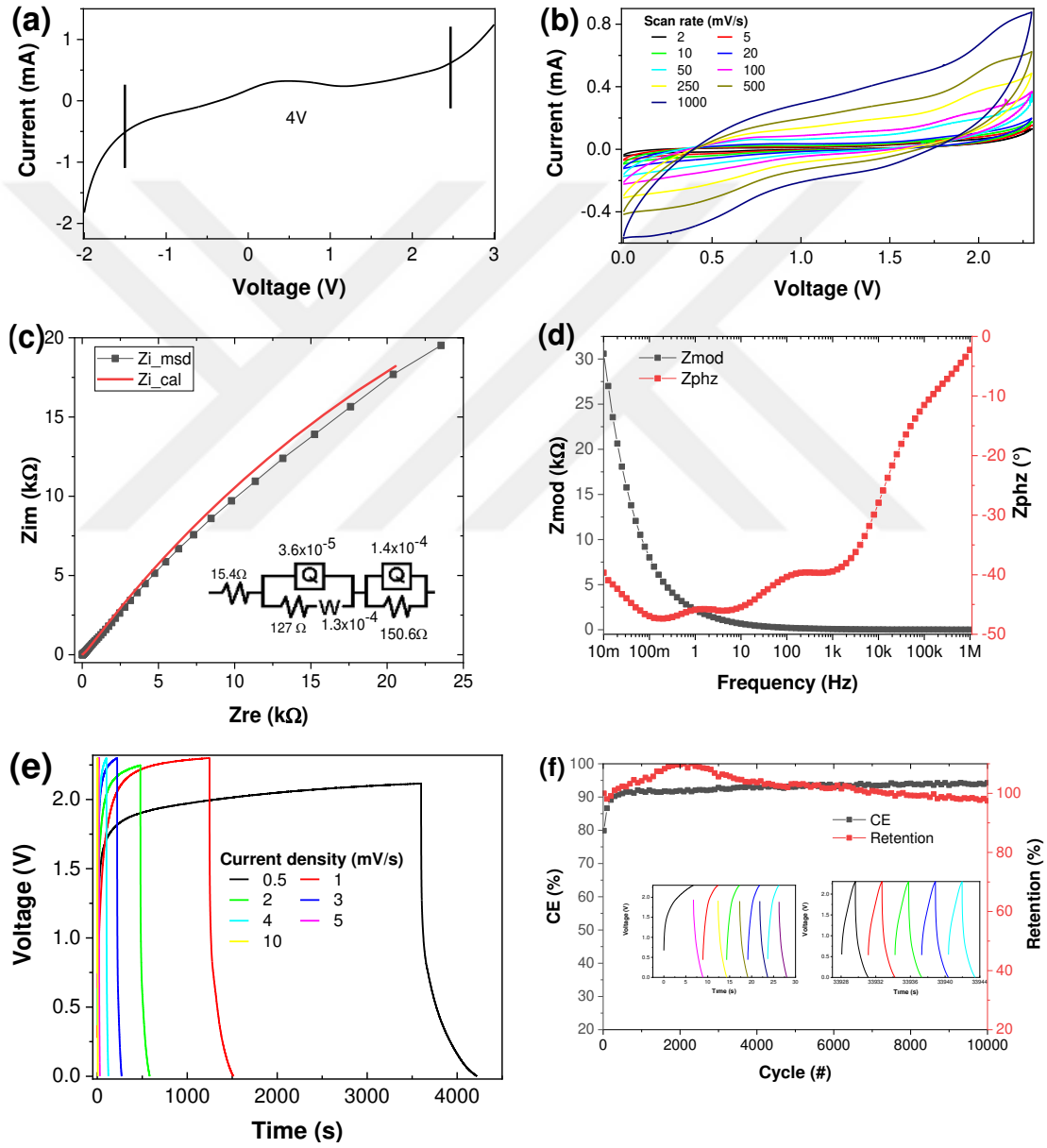

Figure 3.24. *Electrochemical analysis results of supercapacitors with MXene electrodes, a Celgard separator, and [BMIM]BF_4 IL electrolyte, tested after a rest period of over 12 hours. The figure includes: (a) LSV results in the voltage range of -2 to 3 V, (b) CV curves at varying scan rates to evaluate rate-dependent performance, (c) Nyquist plot fitted with a modified Randles equivalent circuit, (d) Bode plot showing impedance and phase angle over a frequency range of 10 mHz to 1 MHz, (e) GCD profiles at different current densities, and (f) coulombic efficiency and capacitance retention over 10,000 GCD cycles.*

Table 3.11. *Calculated results of the supercapacitor with MXene electrodes, a Celgard separator, and [BMIM]BF_4 IL electrolyte, tested after a 12-hour rest period, highlighting capacitance values derived from CV and GCD analyses, along with Nyquist fit parameters.*

Capacitance from CV analyses			
Scan rate (mV s^{-1})	**SAC (mF cm^{-2})**	**SGC (F g^{-1})**	**SVC (F cm^{-3})**
2	18.20	427.60	3925.07
5	10.64	249.98	2294.64
10	7.10	166.87	1531.73
20	4.90	115.05	1056.07
50	3.67	86.22	791.41
100	2.50	58.64	538.23
250	1.61	37.82	347.19
500	1.17	27.53	252.68
1000	0.88	20.63	189.35
Capacitance from GCD analyses			
Current density (A g^{-1})	**SGC (F g^{-1})**	**SVC (F cm^{-3})**	
0.5	181.55	1666.67	
1	125.43	1151.40	
2	100.44	922.03	
3	71.80	659.12	
4	41.18	378.06	
5	24.43	224.28	
Nyquist fit parameters			
R_s (Ω)	**R_{ct} (Ω)**	**CPE (S s^n)**	**W_b (S $s^{1/2}$)**
16.5	705	2.4×10^{-5}	1.1×10^{-4}

3.5.5. MXene supercapacitors in STFSI IL electrolyte

Similar to the results with the [BMIM]BF_4 IL electrolyte, the use of MXene electrodes with the STFSI/AN electrolyte showed a significant limitation in the voltage window, falling short of the expected performance standards for ionic liquid electrolytes. While the [BMIM]BF_4 electrolyte supported an extended voltage window of up to 2.2V, it is plausible that a similar extension could be achieved with the STFSI electrolyte. To explore this possibility, MXene electrodes were tested in STFSI without acetonitrile, using both filter paper and Celgard separators.

3.5.5.1. Using celgard separator

Figure 3.25 presents the electrochemical performance of supercapacitors assembled with MXene electrodes, a Celgard separator, and an STFSI IL electrolyte. The CV curves at varying potential windows, shown in Figure 3.25(a), indicate that a maximum potential window of 2.1 V is achievable. The CV curves at different scan rates, illustrated in Figure 3.25(b), exhibit near-rectangular shapes, suggesting a storage mechanism predominantly governed by EDLC. Unfortunately, measurements at scan rates below 10 mV s^{-1} were unsuccessful, preventing a complete characterization of the device. Nevertheless, specific capacitances were calculated from the obtained CV curves, with results summarized in Table 3.12. At a scan rate of 10 mV s^{-1}, the device demonstrated an SGC of 115 F g^{-1}, which outperformed the immediate test results obtained with Celgard and [BMIM]BF_4 electrolyte. However, the potential window in this case was limited to 1.8 V.

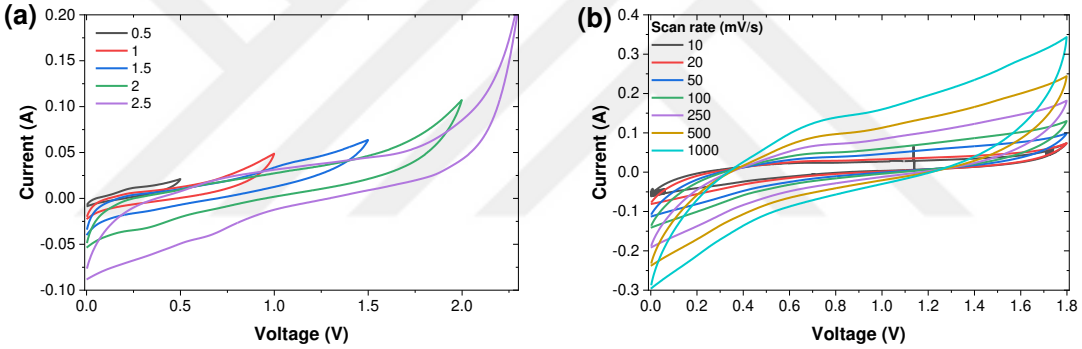

Figure 3.25. *Cyclic voltammetry (CV) results of supercapacitors with MXene electrodes, Celgard separator, and STFSI IL electrolyte, showing (a) CV curves at varied voltage windows and (b) CV curves at varying scan rates.*

Table 3.12. *Capacitances derived from CV curves for supercapacitors using MXene electrodes, STFSI IL electrolyte, and a Celgard separator.*

Scan rate (mV s^{-1})	SAC (mF cm^{-2})	SGC (F g^{-1})	SVC (F cm^{-3})
10	4.90	115.02	1055.84
20	3.06	71.95	660.46
50	1.82	42.83	393.16
100	1.18	27.64	253.73
250	0.68	15.99	146.78
500	0.46	10.79	99.08
1000	0.32	7.52	69.07

3.5.5.2. Using filter paper separator

The electrochemical performance of supercapacitors fabricated with MXene electrodes, a filter paper separator, and STFSI IL electrolyte is shown in Figure 3.26. These results were obtained following a rest period of over 12 hours to ensure stable measurements.

Figure 3.26(a) displays the CV curves at varying potential windows, indicating that a maximum potential window of approximately 2 V is achievable. However, the results also show early signs of electrolyte disintegration starting around 1.8 V, suggesting that 2 V may exceed the stability limit for STFSI in this configuration.

Figure 3.26(b) illustrates the CV curves at different scan rates. The curves exhibit a near-rectangular shape, similar to those obtained with the Celgard separator, indicating that the energy storage mechanism is predominantly EDLC-dominated. However, the potential window limitation observed in this case highlights the challenges associated with electrolyte stability.

At a scan rate of 2 mV s^{-1}, the device demonstrates an SGC of 608 F g^{-1}. This value is notably lower than the 866 F g^{-1} observed with the same configuration but using [BMIM]BF_4 IL electrolyte, underscoring the superior electrochemical performance of [BMIM]BF_4 over STFSI in this context. Detailed capacitance results for other scan rates are provided in Table 3.13.

The EIS results, obtained over a frequency range of 1 mHz to 1 MHz, are presented as the Nyquist plot in Figure 3.26(c) and the Bode plot in Figure 3.26(d). The Nyquist plot was analyzed using a modified Randles equivalent circuit, yielding an ESR of 7.3 Ω. Notably, this represents the lowest ESR recorded among all supercapacitors tested with IL electrolytes in this study, indicating excellent charge transfer and minimal internal resistance for this configuration. Additionally, the Warburg diffusion constant was estimated to be 1.8×10^{-11} S $s^{1/2}$, suggesting minimal ion diffusion limitations within the system.

The Bode magnitude plot demonstrates that impedance increases towards infinity at low frequencies, signifying the dominance of capacitive behavior in this region. Conversely, the impedance approaches zero around 10 kHz and continues to decrease gradually up to 1 MHz. This behavior highlights the transition from capacitive to resistive characteristics as the frequency increases.

The Bode phase angle plot provides further insight into the device's dynamic response. A relaxation time of 1.6 µs, the lowest observed in this study, was calculated, emphasizing the superior frequency response and rapid charge-discharge capability of the supercapacitor. This result underscores the efficiency of the device's energy storage mechanism, particularly when compared to other IL-based supercapacitors analyzed in this work.

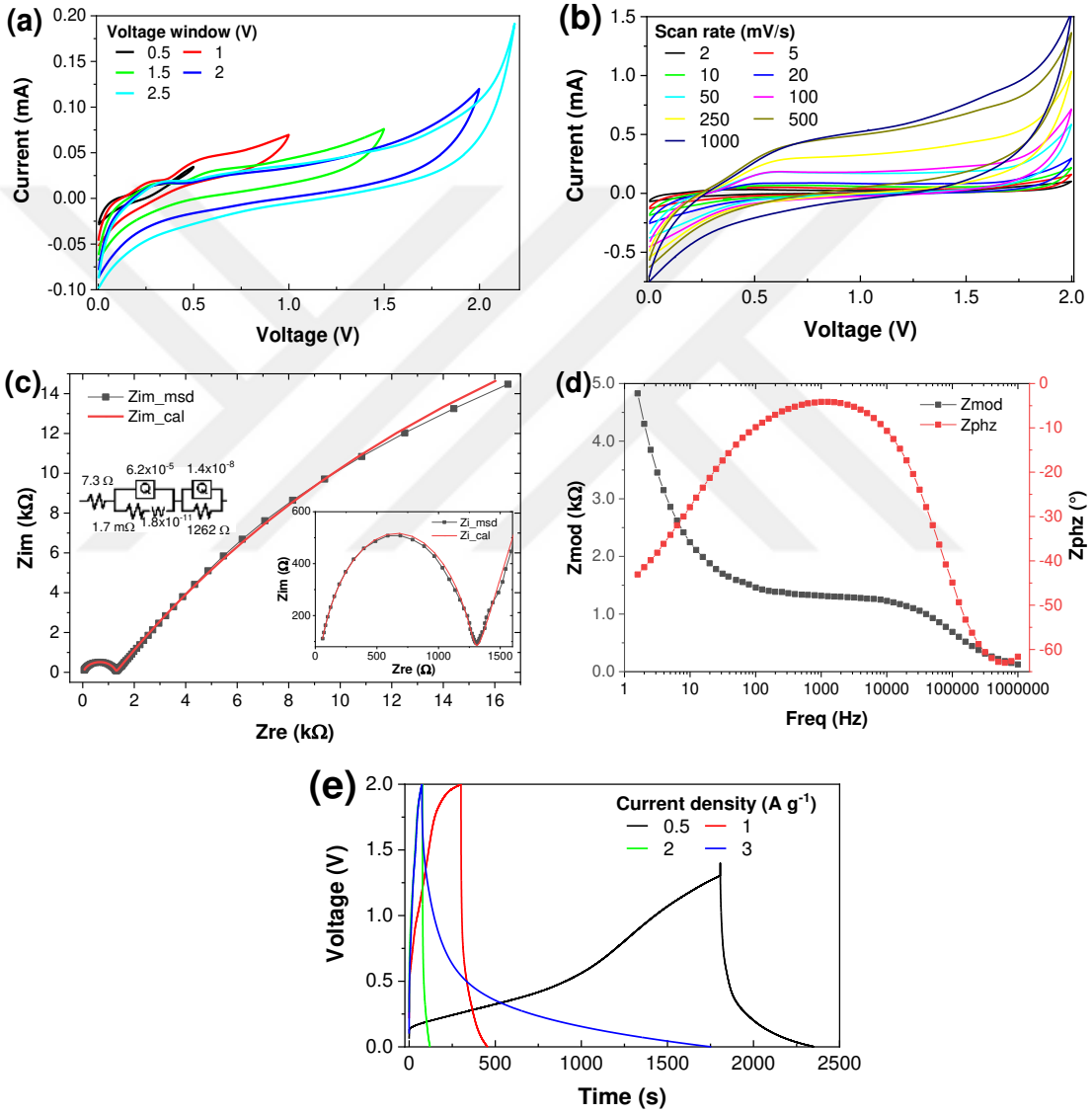

Figure 3.26. *Electrochemical performance of supercapacitors with MXene electrodes, a filter paper separator, and STFSI IL electrolyte, showing: (a) CV curves at different voltage windows, (b) CV curves at varying scan rates, (c) Nyquist plot fitted with a modified Randles equivalent circuit, (d) Bode plot within the 1 Hz to 1 MHz frequency range, and (e) GCD curves at different current densities.*

The GCD analysis performed at varying current densities is depicted in Figure 3.26(e). From the discharge curve at a current density of 0.5 A g^{-1}, an SGC of 197 F g^{-1} is determined, highlighting the device's charge-storage capability under relatively low current conditions. Detailed SGC values at other current densities, reflecting the device's performance under different operational scenarios, are summarized in Table 3.13.

Table 3.13. *Capacitance data and Nyquist fit parameters of supercapacitors made with MXene electrodes, filter paper separator, and STSFI IL electrolyte.*

Capacitance from CV analyses			
Scan rate (mV s^{-1})	**SAC (mF cm^{-2})**	**SGC (F g^{-1})**	**SVC (F cm^{-3})**
2	25.89	608.17	5582.65
5	18.21	427.77	3926.66
10	13.03	306.09	2809.72
20	8.95	210.21	1929.57
50	6.19	145.46	1335.25
100	3.68	86.43	793.41
250	2.20	51.61	473.74
500	1.61	37.75	346.54
1000	1.03	24.27	222.78
Capacitance from GCD analyses			
Current density (A g^{-1})	**SGC (F g^{-1})**	**SVC (F cm^{-3})**	
0.5	195.07	1790.73	
1	86.98	798.49	
2	49.18	451.51	
3	37.04	339.99	
Nyquist fit parameters			
R_s (Ω)	**R_{ct} (Ω)**	**CPE ($S\ s^n$)**	**W_b ($S\ s^{1/2}$)**
7.3	1.7×10^{-3}	6.2×10^{-5}	5.8×10^{-11}

3.5.6. MXene supercapacitors in LiTFSI-VC electrolyte

Lithium bis(trifluoromethanesulfonyl)imide (LiTFSI) is one of the most extensively studied imide-based lithium salts, widely recognized for its advantageous electrochemical properties. At room temperature, LiTFSI typically exists as a white crystalline solid or powder, with the molecular formula $C_2F_6LiNO_4S_2$. A defining characteristic of this salt lies in the $CF_3SO_2^-$ functional group, which exhibits a strong

electron-withdrawing effect. This feature enhances the delocalization of negative charges, effectively reducing ion pairing and significantly increasing the salt's solubility in a broad range of solvents [187]. Furthermore, LiTFSI boasts excellent resistance to hydrolysis, superior ionic conductivity, and outstanding thermal stability, making it a highly versatile candidate for advanced energy storage systems [188,189].

The promising attributes of LiTFSI have been demonstrated in various applications, including lithium-ion batteries. For instance, studies by Buddie Mullins' team reveal that LiTFSI electrolytes provide enhanced cycling stability at high current densities. However, its overall performance in battery systems is constrained by limitations such as substantial overpotential during cycling in lithium-symmetric cells [190]. Moreover, the salt's insufficient passivation capability on positive electrode current collectors often leads to continuous corrosion under high-voltage conditions, further limiting its long-term reliability [191,192].

Despite these challenges in battery applications, the unique properties of LiTFSI—such as its high ionic conductivity and thermal stability—present compelling opportunities for improving supercapacitor performance. Supercapacitors, which rely heavily on the conductivity and stability of their electrolytes, could benefit significantly from the inherent characteristics of LiTFSI. Its ability to maintain electrochemical integrity across a wide temperature range and its resistance to hydrolysis could enhance both the energy density and operational stability of supercapacitors. Additionally, the salt's compatibility with organic solvents and ionic liquids may facilitate the development of electrolytes capable of operating within an extended voltage window, a critical factor in achieving higher energy storage capacities.

Recently, LiTFSI has also shown promise in advanced supercapacitor applications, thanks to its ability to broaden the electrochemical stability window and enhance device performance. For instance, Wang et al. demonstrated the use of an ultrahigh concentration LiTFSI electrolyte in an innovative "water-in-salt" (WIS) configuration, achieving an extended electrochemical stability window with cathodic and anodic potentials of 1.9 V and 4.9 V vs. Li^+/Li, respectively [193]. Inspired by this breakthrough, Zhang et al. utilized a 21 M LiTFSI electrolyte in a hybrid supercapacitor system comprising Fe_3O_4 and MnO_2 electrodes. The resulting device achieved an impressive operating voltage of 2.2 V and a specific energy of 35.5 Wh kg^{-1} [194]. These findings illustrate the potential of LiTFSI to improve energy storage performance, even in challenging configurations.

Moreover, Yu et al. provided a comprehensive overview of supercapacitors employing LiTFSI-based electrolytes, identifying critical strategies to optimize performance in various systems, including those utilizing non-aqueous or hybrid electrolyte setups [195]. These studies collectively underscore the versatility of LiTFSI as an electrolyte for supercapacitors, opening avenues for further exploration in enhancing energy and power densities across different device architectures.

This combination of attributes positions LiTFSI as a promising, albeit underexplored, candidate for supercapacitor applications. The following section explores its potential to address the challenges in current supercapacitor electrolyte systems and highlights its role in advancing the performance of next-generation energy storage devices.

Figure 3.27 presents the electrochemical analysis of supercapacitors fabricated using MXene electrodes, a LiTFSI-vinylene carbonate (LiTFSI-VC) electrolyte, and a filter paper separator. The voltage-sweep cyclic voltammetry (CV) results in Figure 3.27(a) suggest a potential window exceeding 2 V. However, the operational voltage was limited to 1.5 V for the rate-sweep CV analysis, as shown in Figure 3.27(b). At a scan rate of 2 mV s^{-1}, the supercapacitors achieved an outstanding SGC of 5160 F g^{-1}, marking a new benchmark in performance—more than five times higher than the previously reported maximum of 1040 F g^{-1}. Even at a high scan rate of 20 mV s^{-1}, the devices retained an impressive SGC of 1458 F g^{-1}, underscoring the exceptional synergy between the MXene electrodes and the LiTFSI-VC electrolyte. Capacitance values for other scan rates are provided in Table 3.14.

The Nyquist plot in Figure 3.27(c), fitted using a Randles equivalent circuit model, reveals an equivalent ESR of 15.6 Ω, reflecting the low internal resistance of the devices. The Bode plot in Figure 3.27(d) further corroborates the impedance data, with the magnitude curve aligning with prior results. However, the phase angle plot differs significantly, exhibiting a single peak rather than the multiple peaks observed in earlier studies, suggesting a distinct electrochemical behavior in this system.

Despite achieving a record-breaking SGC of 5160 F g^{-1}, the supercapacitors faced stability issues and failed before comprehensive performance testing could be completed. As a result, only CV and EIS data are presented in this section. This highlights the need to further optimize the device architecture and electrolyte compatibility to ensure long-term stability while maintaining exceptional electrochemical performance.

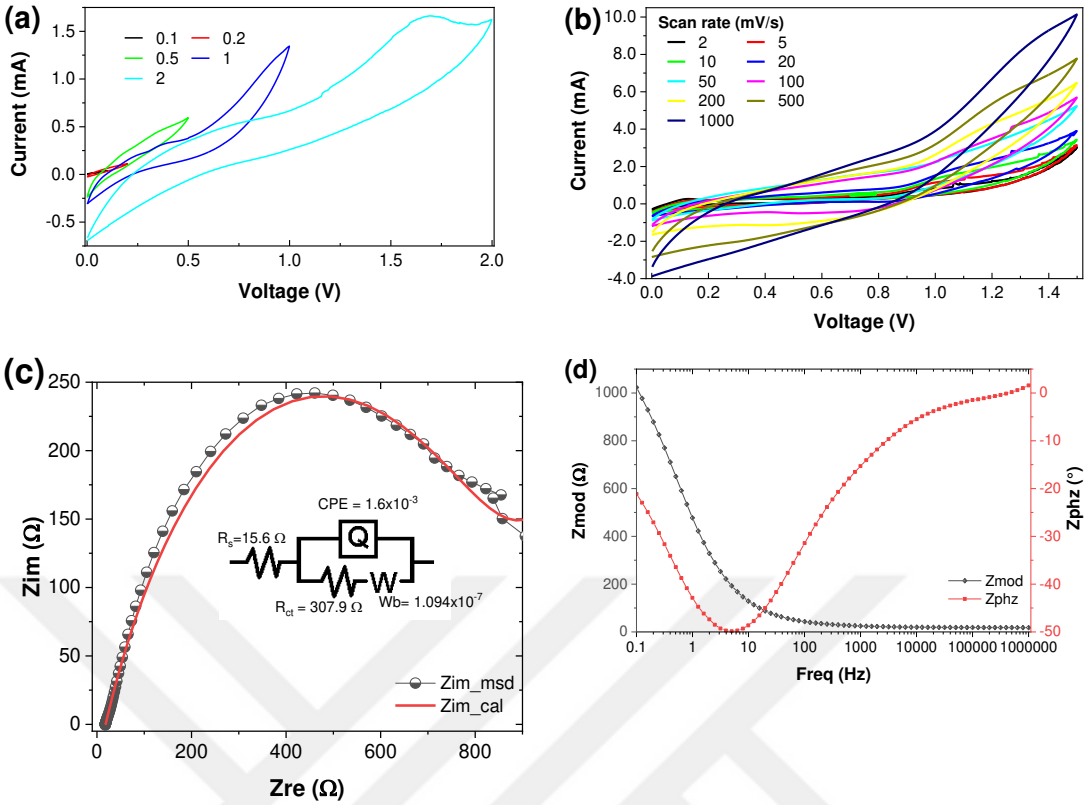

Figure 3.27. *Electrochemical analysis results of supercapacitors fabricated with MXene electrodes, a filter paper separator, and LiTFSI-VC electrolyte, including (a) CV curves at varying voltage windows, (b) CV curves at different scan rates, (c) Nyquist plot fitted using a Randles equivalent circuit model, and (d) Bode plot in the frequency range of 0.1 Hz to 1 MHz.*

Table 3.14. *Capacitance, and Nyquist fit data of supercapacitors fabricated with MXene electrodes, a filter paper separator, and LiTFSI-VC electrolyte.*

Capacitance from CV analyses			
Scan rate (mV s^{-1})	**SAC (mF cm^{-2})**	**SGC (F g^{-1})**	**SVC (F cm^{-3})**
2	219.66	5160.46	47369.84
5	145.00	3406.37	31268.43
10	92.95	2183.70	20045.01
20	62.07	1458.22	13385.59
50	38.35	900.91	8269.81
100	24.64	578.82	5313.19
200	16.33	383.59	3521.12
500	8.08	189.74	1741.66
1000	4.51	105.97	972.75

Nyquist fit parameters			
R_e (Ω)	**R_{ct} (Ω)**	**CPE (S s^n)**	**W_b (S $s^{1/2}$)**
15.6	308	1.55 x 10^{-3}	1.09 x 10^{-7}

Figure 3.28 displays the CV of another supercapacitor using LiTFSI electrolyte at a 20 mV s^{-1} scan rate. The potential window was varied from 0.5 to 4 V, beyond which signs of electrolyte breakdown were observed, suggesting that the device could operate within a 4 V potential window. Notably, it was observed that increasing the voltage window resulted in SGC, with values of 2520 F g^{-1} at 4 V and 1020 F g^{-1} at 3.5 V. However, the analysis was limited to the V-sweep CV, as the device failed before further testing could be completed.

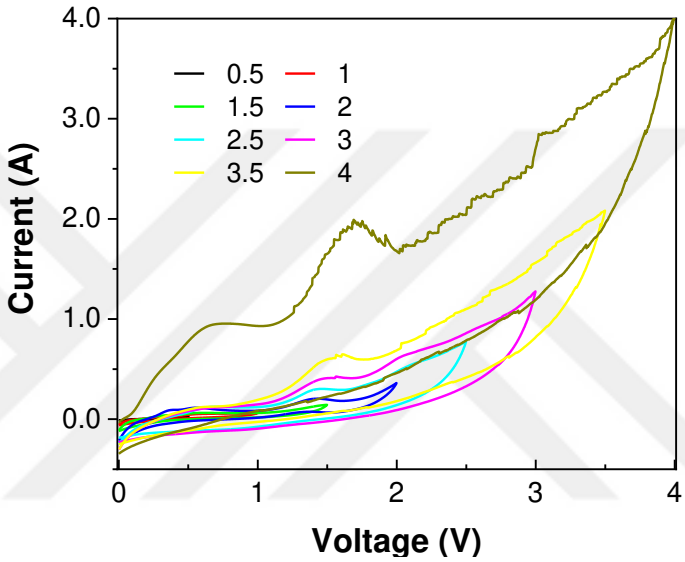

Figure 3.28. *CV of MXene supercapacitor with LiTSFI-VC electrolyte at 20 mV s^{-1} and varying voltage windows.*

3.6. Summary

This chapter provided a comprehensive exploration of MXene-based supercapacitors with different electrolytes, emphasizing the role of non-functionalized MXene electrodes in both aqueous and IL electrolytes. Section 3.2 focused on the synthesis of MXenes via CVD and their characterization through Raman, AFM, SEM, XRD, and XPS techniques. The performance of MXene electrodes was investigated with varying electrode thickness, coverage, and separator types. A key finding was the significant influence of separator selection on the performance of supercapacitors, with the optimal separator varying depending on the electrolyte used. This highlights the need for careful consideration of separator materials for both aqueous and IL electrolytes, as the best match for one electrolyte system may not be suitable for another.

In Section 3.5, the performance of supercapacitors with IL electrolytes was further explored. EMIMBF4 and TSTFI dissolved in AN initially provided a limited voltage window of approximately 0.6 V, which was improved to 2.2 V for the former after removing AN, and to 2 V for the latter. The results also showed that filter paper separators generally outperformed Celgard separators in terms of specific capacitance, while Celgard demonstrated superior cycle stability. Finally, the use of LiTFSI electrolyte yielded groundbreaking SGC values but was accompanied by significant stability issues, limiting the full characterization of the devices.

Together, these findings emphasize the complexity of optimizing MXene-based supercapacitors, where both the electrolyte type and separator material play pivotal roles in determining the overall performance. The chapter highlights the challenges and opportunities in maximizing the energy storage potential of MXenes by tailoring key parameters such as electrolyte, separator, and electrode characteristics.

While graphene demonstrates remarkable stability and power density, addressing the limitations of energy density requires exploring alternative 2D materials. The next chapter focuses on MXenes, a class of materials that exhibit complementary strengths, including high energy density and broader voltage windows, positioning them as a valuable counterpart to graphene in supercapacitor applications.

Having established the performance metrics of graphene and MXene-based supercapacitors, the following chapter undertakes a comparative analysis to identify their respective strengths, limitations, and synergistic potential. This analysis provides a comprehensive framework for selecting and optimizing materials for specific applications.

4. DISCUSSION AND COMPARATIVE ANALYSIS

4.1. Overview of Findings

4.1.1. Summary of main results from chapters 2 and 3

Chapters 2 and 3 of the dissertation detail the exploration of 2D materials—graphene and MXenes-as electrode materials for high-performance supercapacitors. Chapter 2 focuses on graphene-based supercapacitors, highlighting the synthesis of high-quality multilayer graphene via CVD. Two transfer methods, Photoresist-Assisted Transfer (PAT) and PMMA/PDMS-Assisted Transfer (PPAT), were evaluated, with PAT providing continuous films and PPAT achieving cleaner but fractured transfers. The supercapacitors demonstrated dominant EDLC behavior, with minimal pseudo capacitance contributions. In Chapter 3, MXenes, particularly Mo_2C, were synthesized via CVD and characterized using techniques like SEM, Raman, and XRD. Their performance was investigated in both aqueous and ionic liquid (IL) electrolytes. Separator choice and electrolyte type were found to significantly affect the electrochemical behavior, thus emphasizing the importance of tailored configurations.

4.1.2. Key performance metrics

Table 4.1 summarizes the key performance metrics of graphene-based and MXene-based supercapacitors for a clearer understanding of the devices' performance.

Table 4.1. *Key performance metrics of graphene vs. MXene-based supercapacitors.*

Metric	Graphene-based supercapacitors	MXene-based supercapacitors
SGC	Achieved up to 316 F g^{-1}	Recorded a peak of 5160 F g^{-1} with LiTFSI-VC electrolyte.
Cycle Stability	Maintained 100% capacitance retention after 10,000 cycles in Na_2SO_4 electrolyte.	Stability varied with separators between 85% and 98%.
Energy Density	Achieved up to 28.1 Wh kg^{-1} in Na_2SO_4 electrolyte	Achieved up to 144 Wh kg^{-1} in Na_2SO_4, and 391 Wh kg^{-1} with $[BMIM]BF_4$ IL electrolyte.
Voltage Window	Limited to 0.8 V due to the aqueous electrolyte	Up to 2.2 V with IL electrolytes, enabling higher energy densities.
Capacitance Behavior	Predominantly EDLC with minimal pseudo capacitance	A combination of both EDLC and pseudo capacitance

4.1.3. Comparative summary

Graphene-based supercapacitors excelled in cycle stability and reliability, particularly in aqueous electrolytes, but were constrained by their limited voltage window, resulting in moderate energy densities. In contrast, MXenes exhibited exceptional energy density and capacitance in IL electrolytes, leveraging a broader voltage window. However, stability issues, particularly with advanced electrolytes like LiTFSI-VC, highlighted the need for further optimization. This comparative analysis sets the stage for deeper exploration into balancing stability, energy density, and capacitance to harness the full potential of 2D materials in supercapacitor applications.

4.2. Comparative Performance of Graphene- and MXene-Based Supercapacitors in Aqueous Electrolytes

Both graphene- and MXene-based supercapacitors exhibit distinct advantages and limitations when used in aqueous electrolytes. Their performance metrics, including SGC, energy density, and cycle life, are influenced by material properties and device configurations.

4.2.1. Specific gravimetric capacitance (SGC)

Graphene-based supercapacitors: Achieved an SGC of up to 316 F g^{-1}, primarily due to graphene's high surface area (2675 m^2 g^{-1}) and exceptional conductivity. However, aggregation of graphene layers limited ion-accessibility, slightly reducing the practical capacitance.

MXene-Based Supercapacitors: Delivered higher SGC values, particularly with non-functionalized Mo_2C MXenes, where values reached 1041 F g^{-1}. This is attributed to MXenes' intrinsic conductivity, and layered structure, which facilitate charge storage and ion-transport.

4.2.2. Energy density

Graphene-based supercapacitors: Energy densities in aqueous electrolytes remained moderate due to the limited voltage window (~0.8 V). Despite graphene's excellent charge storage capability, the narrow potential range constrained energy output.

MXene-based supercapacitors: While the voltage window was similarly constrained (~1 V in aqueous electrolytes), MXenes demonstrated superior energy

densities compared to graphene due to higher capacitance values and optimized electrode configurations.

4.2.3. Cycle life

Graphene-based supercapacitors: Demonstrated exceptional cycle life, maintaining 100% capacitance retention over 10,000 cycles in Na_2SO_4 electrolyte. This reflects graphene's high chemical stability and robust mechanical properties.

MXene-based supercapacitors: Showed good cycle stability, though slightly less consistent than graphene. Separator choice significantly influenced performance, with Celgard improving cycle life while filter paper enhanced capacitance.

4.2.4. Strengths and weaknesses

Table 4.2 highlights the strengths and weaknesses of the supercapacitors, providing a comparative analysis of their performance.

Table 4.2. *Strengths and Weaknesses of Graphene and MXenes in Aqueous Electrolytes*

Material	Strengths	Weaknesses
Graphene	- Exceptional cycle stability with 100% retention over 10,000 cycles.	- Lower specific gravimetric capacitance (SGC) due to layer aggregation.
	- High conductivity, enabling rapid charge/discharge.	- Limited energy density due to a narrow voltage window (~1 V).
	- Excellent mechanical strength and chemical stability.	- Performance constrained by reduced ion-accessibility in thick electrodes.
MXenes	- Higher SGC (>500 F g^{-1}) compared to graphene.	- Slightly lower cycle stability compared to graphene.
	- Rich surface chemistry enhances charge storage and ion-transport.	- Performance heavily depends on separator type and electrode configuration.
	- Superior energy density in aqueous electrolytes.	- Potential issues with long-term stability under certain conditions.

4.2.5. Factors influencing performance

- **Electrode thickness:**

  Thicker graphene electrodes reduce ion-accessibility due to layer aggregation, while MXene layers, when appropriately optimized, maintain better ion-transport.

- **Separator type:**

  For MXenes, filter paper separators improved capacitance, while Celgard enhanced cycle stability. Graphene performance showed less dependence on separator type, reflecting its stability across configurations.

- **Electrolyte compatibility:**

  Both materials performed well in Na_2SO_4 aqueous electrolytes, but MXenes exhibited a more pronounced benefit from their intrinsic surface chemistry, leading to higher capacitance values.

In summary, graphene offers superior cycle life and reliability, making it ideal for applications requiring durability, while MXenes provide higher SGC and energy densities, better suited for high-performance energy storage where stability can be optimized through device design.

4.3. MXene Performance in IL Electrolytes

MXene-based supercapacitors exhibit significant enhancements in performance when paired with IL electrolytes compared to aqueous systems. These improvements stem from the broader voltage window and superior electrolyte properties of ILs, although challenges such as stability and electrode degradation persist.

4.3.1. Improvements in energy density and voltage window

MXenes paired with [BMIM]BF_4 IL electrolyte achieved an impressive energy density of **391 Wh kg^{-1}**, over twice the 144 Wh kg^{-1} observed in aqueous electrolytes.

The use of ILs such as [BMIM]BF_4 and LiTFSI-VC leveraged their electrochemical stability and low volatility to enhance the energy storage capabilities.

IL electrolytes extended the operational voltage window of the supercapacitors to **2.2 V**, compared to the ~1 V constraint in aqueous systems. This broader voltage range directly contributed to higher energy densities, as energy density scales quadratically with voltage.

4.3.2. Challenges in IL systems

- **Stability issues:**

  Severe stability problems were observed in systems using advanced IL electrolytes like LiTFSI-VC. Despite achieving a record SGC of **5160 F g^{-1}**, rapid degradation limited practical applications.

- **Electrode degradation:**

  Prolonged cycling in ILs can lead to electrode material degradation, potentially due to incompatibilities between the electrolyte and the MXene surface or intercalation-induced stress.

  The structural stability of MXenes under IL operation remains a critical area for improvement.

4.3.3. Role of separators in performance metrics

Separators played a crucial role in determining the electrochemical performance of MXene-based supercapacitors in IL systems:

- **Celgard separator:**

  Improved cycle stability, providing better durability over extended cycling.

  Maintained performance consistency by minimizing ionic resistance.

- **Filter paper separator:**

  Enhanced specific capacitance by facilitating greater ion-accessibility to the MXene surface.

  Demonstrated trade-offs in stability compared to Celgard separators.

4.4. Material and Device-Level Trends

The performance of supercapacitors is influenced by several factors, including the choice of electrode material, electrolyte type, and device configuration. Each of these elements plays a significant role in determining the overall energy density, power density, stability, and efficiency of the device. Below, we explore how each of these factors impacts supercapacitor performance, highlighting key trends that emerge from material-level and device-level considerations.

4.4.1. Impact of electrode material on energy density, power density, and stability

The choice of electrode material is crucial in determining the energy storage performance of supercapacitors. Materials like MXenes and graphene exhibit distinct characteristics, each offering specific advantages and challenges in terms of energy and power density, as well as long-term stability. Understanding these material-specific trends allows for better optimization of supercapacitor performance based on the intended application.

4.4.1.1. Energy density

MXenes outperform graphene in energy density across both aqueous and ionic liquid (IL) systems. This is due to their rich surface chemistry, higher quantum capacitance, and efficient ion-transport through layered structures. For example, MXenes achieved an energy density of **391 Wh kg^{-1}** in IL electrolytes, whereas graphene exhibited lower values constrained by limited voltage windows.

4.4.1.2. Power density

Graphene exhibits superior power density due to its exceptional conductivity and rapid charge/discharge capabilities. Its carrier mobility (~200,000 $cm^2\ V^{-1}{\cdot}s^{-1}$) ensures minimal resistance during operation. MXenes, though conductive, experience slight trade-offs in power density due to their pseudo capacitive contributions and reliance on surface interactions.

4.4.1.3. Stability:

Graphene demonstrates excellent cycle stability, retaining 100% capacitance over 10,000 cycles in aqueous electrolytes. MXenes, while stable under certain conditions, face challenges with structural degradation, particularly in advanced IL systems like LiTFSI-VC. Separator and electrolyte compatibility significantly influence MXene stability.

4.4.2. Influence of electrolyte type on performance

- **Aqueous electrolytes:**

Aqueous systems provide reliable and cost-effective performance with moderate energy density due to a limited voltage window (~1 V). Graphene performs exceptionally well in these systems, offering robust cycle life and minimal degradation. MXenes also perform adequately but are limited by the electrolyte's narrow potential range.

- **Ionic liquid electrolytes:**

  ILs enable broader voltage windows (up to **2.2 V**) and significantly higher energy densities, as observed with MXenes paired with [BMIM]BF_4. These electrolytes also support improved ionic conductivity and electrochemical stability. However, challenges include compatibility with electrode materials and stability issues over prolonged cycling, particularly for MXenes.

4.4.3. Role of device configurations

4.4.3.1. Separator selection:

Separators significantly influence device performance.

- **Celgard** separators enhance cycle stability by reducing ionic resistance and preventing electrode degradation.
- **Filter paper** separators improve specific capacitance by facilitating better ion-accessibility but may compromise stability.

4.4.3.2. Electrode architecture:

Graphene's performance is constrained by aggregation and thickness, which reduces ion-accessibility in multilayer structures. Efforts to decouple graphene layers using novel stacking techniques have shown potential.

MXene architectures leverage their layered structure to enhance ion-transport and surface interaction. Optimizing mass loading and coverage further enhances their performance.

4.4.4. Conclusion

Overarching trends highlight the interplay between material properties, electrolyte types, and device configurations. Graphene offers excellent power density and stability, excelling in aqueous systems, while MXenes demonstrate superior energy density and

versatility, particularly in IL systems. Device configurations, including separator type and electrode architecture, play a critical role in balancing trade-offs between capacitance, stability, and energy output. These insights emphasize the need for integrated design approaches to optimize supercapacitor performance for specific applications.

4.5. Challenges and Opportunities

4.5.1. Challenges observed in the research

- **Stability issues in MXene-based supercapacitors with il electrolytes**

  MXene-based supercapacitors faced severe stability challenges when paired with IL electrolytes, particularly in advanced systems like LiTFSI-VC. While these configurations achieved high SGC and energy densities, rapid degradation limited their practical applications.

  Structural breakdown and loss of performance over extended cycling remain critical obstacles, likely driven by intercalation-induced stress and chemical incompatibility between the electrolyte and MXene surface.

- **Electrode degradation at high voltages**

  Operating at extended voltage windows (e.g., up to 2.2 V in IL systems) introduced stresses that led to electrode degradation. This is particularly problematic for MXenes, where the layered structure and surface chemistry are more susceptible to changes under high electrochemical loads.

  Degradation results in reduced stability, compromised charge storage efficiency, and loss of capacitance over time.

4.5.2. Proposed solutions and future research directions

- **Developing hybrid electrode materials**

  Graphene-MXene composites: Combining graphene's superior conductivity and cycle stability with MXenes' high capacitance and energy density could result in hybrid electrodes that mitigate individual material weaknesses.

  By leveraging graphene's ability to reduce aggregation and enhance mechanical stability, these composites could offer improved performance in both aqueous and IL electrolytes.

- **Improving electrolyte compatibility with MXenes**

Research into surface functionalization of MXenes can enhance compatibility with IL electrolytes, reducing chemical degradation and improving long-term stability.

Developing tailored IL formulations with additives or stabilizers may minimize interactions that compromise MXene structure, enabling more reliable performance at high voltages.

- **Exploring new separators tailored for specific electrolytes**

  Designing separators that are chemically compatible with ILs while maintaining mechanical integrity and ionic conductivity can help address stability issues.

  Advanced materials like nanoporous membranes or polymer composites could provide optimized ion-transport pathways while protecting the electrodes from degradation.

4.5.3. Conclusion

While MXene-based supercapacitors exhibit remarkable potential, challenges related to stability and electrode degradation, particularly in IL systems, must be addressed to unlock their full capabilities. Hybrid electrode materials, enhanced electrolyte formulations, and next-generation separators offer promising pathways for overcoming these obstacles. Future research focusing on these solutions can pave the way for more robust, high-performance supercapacitors.

4.6. Broader Implications

4.6.1. Implications for the energy storage field

The findings in this research highlight the transformative potential of 2D materials like graphene and MXenes in advancing supercapacitor technology. By bridging the gap between energy and power density, these materials address critical limitations in current energy storage systems, offering enhanced performance for applications ranging from portable devices to industrial systems. The ability to tailor device configurations and material properties opens new pathways for designing energy storage systems that meet diverse and evolving needs.

4.6.2. Potential applications of graphene-based supercapacitors

- **Consumer electronics**

Graphene-based supercapacitors, with their excellent cycle stability and high power density, are well-suited for portable electronic devices such as smartphones, tablets, and wearable gadgets.

Their rapid charge-discharge capability and durability make them ideal for applications requiring frequent usage and quick energy replenishment.

- **Biomedical devices**

The chemical stability and biocompatibility of graphene enable its integration into biomedical devices such as implantable sensors, health monitors, and portable diagnostic equipment.

These devices benefit from graphene's ability to provide consistent power delivery with minimal degradation over extended use.

4.6.3. Opportunities for MXene-based supercapacitors

- **High-performance energy systems**

The superior energy density and broader voltage windows achieved by MXene-based supercapacitors make them ideal for high-performance applications, including aerospace, military, and electric vehicles.

Systems requiring compact yet high-capacity energy storage, such as drones, satellites, and hybrid vehicles, can benefit from MXenes' enhanced performance metrics.

- **Renewable energy integration**

MXenes' ability to operate efficiently in ionic liquid electrolytes opens opportunities for integration into renewable energy systems where long-term energy storage and high energy throughput are essential.

For instance, they could play a vital role in stabilizing the energy supply in wind and solar power systems, ensuring consistent output despite intermittent generation.

4.6.4. Conclusion

Advancements in graphene- and MXene-based supercapacitors have far-reaching implications for the field of energy storage. While graphene excels in durability and rapid energy delivery, MXenes offer solutions for applications requiring higher energy densities and voltage windows. These complementary capabilities position 2D materials as pivotal in shaping the future of energy storage technologies, catering to both everyday consumer needs and cutting-edge industrial demands.

4.7. Summary of Comparative Insights

This chapter provides a comprehensive comparison of graphene- and MXene-based supercapacitors, highlighting their strengths and limitations across various performance metrics and applications.

4.7.1. Graphene-based supercapacitors:

Graphene demonstrates exceptional cycle stability, robust power density, and mechanical durability, making it highly suitable for applications requiring frequent charge-discharge cycles and long-term reliability. These include consumer electronics like smartphones and wearables, as well as biomedical devices where consistent performance and biocompatibility are critical.

4.7.2. MXene-based supercapacitors

MXenes outperform graphene in energy density and capacitance, particularly in IL electrolytes, due to their rich surface chemistry and broader voltage windows. This makes MXenes ideal for high-performance applications such as aerospace, electric vehicles, and renewable energy systems where compact, high-capacity energy storage is essential.

4.7.3. Complementary nature of graphene and MXenes

The strengths of graphene and MXenes are complementary, offering unique opportunities for advancing supercapacitor technology. While graphene's stability and conductivity excel in low-to-moderate energy density applications, MXenes provide high energy and voltage performance for demanding systems. Hybrid approaches, such as

graphene-MXene composites, have the potential to synergize these properties, creating versatile energy storage solutions tailored to diverse needs.

In conclusion, both materials play pivotal roles in shaping the future of supercapacitors, with graphene suited for reliability-focused applications and MXenes driving innovation in high-performance energy storage. Their complementary capabilities position them as foundational materials for next-generation energy storage technologies.

4.8. Summary of Chapter

This chapter presented a detailed comparison of graphene and MXene-based supercapacitors, focusing on key metrics such as energy density, power density, and cycle stability. Graphene excelled in durability and power delivery, while MXenes offered superior energy storage capabilities and broader voltage windows. The findings emphasize the complementary nature of these materials and propose hybrid configurations and tailored device designs to maximize performance across diverse applications.

The insights gained from the comparative analysis inform the broader implications of this research and outline future directions for advancing supercapacitor technology. The final chapter consolidates the key contributions of this work and proposes actionable steps to overcome existing challenges.

5. CONCLUSION AND FUTURE PERSPECTIVES

5.1. Conclusion

This dissertation demonstrates the potential of graphene and MXenes as advanced electrode materials for supercapacitors. Graphene supercapacitors, fabricated using rotationally stacked multilayer graphene, exhibited exceptional performance in aqueous electrolytes, achieving high specific gravimetric capacitance and remarkable cycle stability. These results highlight the importance of preserving intrinsic graphene properties through careful layer stacking and material transfer techniques.

MXenes, synthesized via CVD, were evaluated in both aqueous and ionic liquid electrolytes. Their performance was influenced significantly by electrode properties, separator type, and electrolyte configuration. While aqueous electrolytes offered stable cycling performance, ionic liquids like LiTFSI-VC enabled record-breaking specific capacitance but suffered from severe stability issues. Comparative analysis of separators revealed that filter paper excelled in enhancing capacitance, whereas Celgard provided better long-term stability.

5.2. Future Perspectives

This research highlights the critical need to optimize both material properties and device configurations to achieve a balance between energy density, power density, and stability in supercapacitors. By leveraging the unique properties of graphene and MXenes, the findings contribute to bridging the gap between supercapacitors and batteries, advancing the development of versatile energy storage systems. These insights not only demonstrate the potential of 2D materials but also underline the importance of tailoring electrolyte, separator, and electrode configurations for enhanced performance. Future research should address the key challenges of stability, improve the compatibility of MXenes with advanced electrolytes, and develop scalable fabrication techniques to transition these findings into practical, real-world applications.

One significant issue identified during the study was the degradation of the negative electrode material. To mitigate this, future designs could focus on asymmetric supercapacitors, replacing the cathode with more chemically stable materials such as graphene. This approach could enhance the durability and overall efficiency of the device by reducing chemical instability and electrode wear.

Additionally, the thin nature of MXenes synthesized via CVD opens up exciting possibilities for the development of micro or planar supercapacitors. These compact designs would be ideal for integration into portable and wearable electronics, where miniaturization and high performance are critical. Advancing this technology could enable new applications in next-generation electronic devices, further solidifying the role of 2D materials in innovative energy storage solutions.

REFERENCES

[1] Ritchie, H., M. Roser, and P. Rosado. (2022). Energy. https://ourworldindata.org/energy. (Accessed: 09/26/2023).

[2] Mitali, J., S. Dhinakaran, and A.A. Mohamad. (2022). Energy storage systems: a review. *Energy Storage and Saving*, 1 (3), 166–216.

[3] Nocera, D.G. (2008). Living healthy on a dying planet. *Chem Soc Rev*, 38 (1), 13–15.

[4] Robert Fares. (2015). Renewable Energy Intermittency Explained: Challenges, Solutions, and Opportunities - Scientific American Blog Network. https://blogs.scientificamerican.com/plugged-in/renewable-energy-intermittency-explained-challenges-solutions-and-opportunities/. (Accessed: 09/26/2023).

[5] Carla Davis. (2016). Energy Storage: A Limiting Factor for Renewable Energy - Sustainability. https://sustainability.ncsu.edu/blog/changeyourstate/renewable-energy-storage/. (Accessed: 09/26/2023).

[6] Koohi-Fayegh, S., and M.A. Rosen. (2020). A review of energy storage types, applications and recent developments. *J Energy Storage*, 27 101047.

[7] Rahman, M.M., A.O. Oni, E. Gemechu, and A. Kumar. (2020). Assessment of energy storage technologies: A review. *Energy Convers Manag*, 223 113295.

[8] Hall, P.J., and E.J. Bain. (2008). Energy-storage technologies and electricity generation. *Energy Policy*, 36 (12), 4352–4355.

[9] Drummond, R., C. Huang, P.S. Grant, and S.R. Duncan. (2019). Overcoming diffusion limitations in supercapacitors using layered electrodes. *J Power Sources*, 433 126579.

[10] Eredia, M., S. Bellani, M.I. Zappia, L. Gabatel, V. Galli, A. Bagheri, H. Beydaghi, G. Bianca, I. Conticello, V. Pellegrini, and F. Bonaccorso. (2022). High-energy density aqueous supercapacitors: The role of electrolyte pH and KI redox additive. *APL Mater*, 10 (10),.

[11] Pan, S., M. Yao, J. Zhang, B. Li, C. Xing, X. Song, P. Su, and H. Zhang. (2020). Recognition of Ionic Liquids as High-Voltage Electrolytes for Supercapacitors. *Front Chem*, 8 527961.

[12] Najib, S., and E. Erdem. (2019). Current progress achieved in novel materials for supercapacitor electrodes: mini review. *Nanoscale Adv*, 1 (8), 2817–2827.

[13] Ganjoo, R., S. Sharma, A. Kumar, M.M. Areˆmouareˆ, and A. Daouda. (2023). Activated Carbon: Fundamentals, Classification, and Properties. *Activated Carbon*, 1–22.

[14] Karnan, M., A.G.K. Raj, K. Subramani, S. Santhoshkumar, and M. Sathish. (2020). The fascinating supercapacitive performance of activated carbon electrodes with

enhanced energy density in multifarious electrolytes. *Sustain Energy Fuels*, 4 (6), 3029–3041.

[15] Halper Marin S., and Ellenbogen James C. (2006). Supercapacitors: A brief overview. *The MITRE Corporation*, 1.

[16] González, A., E. Goikolea, J.A. Barrena, and R. Mysyk. (2016). Review on supercapacitors: Technologies and materials. *Renewable and Sustainable Energy Reviews*, 58 1189–1206.

[17] Shao, H., Y.C. Wu, Z. Lin, P.L. Taberna, and P. Simon. (2020). Nanoporous carbon for electrochemical capacitive energy storage. *Chem Soc Rev*, 49 (10), 3005–3039.

[18] Zhang, Y., H. Feng, X. Wu, L. Wang, A. Zhang, T. Xia, H. Dong, X. Li, and L. Zhang. (2009). Progress of electrochemical capacitor electrode materials: A review. *Int J Hydrogen Energy*, 34 (11), 4889–4899.

[19] Arbizzani, C., M. Mastragostino, and F. Soavi. (2001). New trends in electrochemical supercapacitors. *J Power Sources*, 100 (1–2), 164–170.

[20] Mastragostino, M., C. Arbizzani, and F. Soavi. (2002). Conducting polymers as electrode materials in supercapacitors. *Solid State Ion*, 148 (3–4), 493–498.

[21] Peng, C., S. Zhang, D. Jewell, and G.Z. Chen. (2008). Carbon nanotube and conducting polymer composites for supercapacitors. *Progress in Natural Science*, 18 (7), 777–788.

[22] Frackowiak, E., V. Khomenko, K. Jurewicz, K. Lota, and F. Béguin. (2006). Supercapacitors based on conducting polymers/nanotubes composites. *J Power Sources*, 153 (2), 413–418.

[23] Zuo, W., R. Li, C. Zhou, Y. Li, J. Xia, and J. Liu. (2017). Battery-Supercapacitor Hybrid Devices: Recent Progress and Future Prospects. *Adv Sci (Weinh)*, 4 (7),.

[24] Li, H., L. Cheng, and Y. Xia. (2005). A hybrid electrochemical supercapacitor based on a 5 V Li-ion battery cathode and active carbon. *Electrochemical and Solid-State Letters*, 8 (9), A433.

[25] Novoselov, K.S., A.K. Geim, S. V. Morozov, D. Jiang, Y. Zhang, S. V. Dubonos, I. V. Grigorieva, and A.A. Firsov. (2004). Electric field in atomically thin carbon films. *Science (1979)*, 306 (5696), 666–669.

[26] Lemme, M.C., D. Akinwande, C. Huyghebaert, and C. Stampfer. (2022). 2D materials for future heterogeneous electronics. *Nature Communications 2022 13:1*, 13 (1), 1–5.

[27] Liu, Y., and X. Peng. (2017). Recent advances of supercapacitors based on two-dimensional materials. *Appl Mater Today*, 8 104–115.

[28] Philip, A., and A. Ruban Kumar. (2023). Recent advancements and developments employing 2D-materials in enhancing the performance of electrochemical supercapacitors: A review. *Renewable and Sustainable Energy Reviews*, 182 113423.

[29] Tomy, M., A. Ambika Rajappan, V. VM, and X. Thankappan Suryabai. (2021). Emergence of Novel 2D Materials for High-Performance Supercapacitor Electrode Applications: A Brief Review. *Energy and Fuels*, 35 (24), 19881–19900.

[30] Cherusseri, J., D. Pandey, and J. Thomas. (2020). Symmetric, Asymmetric, and Battery-Type Supercapacitors Using Two-Dimensional Nanomaterials and Composites. *Batter Supercaps*, 3 (9), 860–875.

[31] Stoller, M.D., C.W. Magnuson, Y. Zhu, S. Murali, J.W. Suk, R. Piner, and R.S. Ruoff. (2011). Interfacial capacitance of single layer graphene. *Energy Environ Sci*, 4 (11), 4685–4689.

[32] Xia, J., F. Chen, J. Li, and N. Tao. (2009). Measurement of the quantum capacitance of graphene. *Nature Nanotechnology 2009 4:8*, 4 (8), 505–509.

[33] Ke, Q., and J. Wang. (2016). Graphene-based materials for supercapacitor electrodes – A review. *Journal of Materiomics*, 2 (1), 37–54.

[34] Bolotin, K.I., K.J. Sikes, Z. Jiang, M. Klima, G. Fudenberg, J. Hone, P. Kim, and H.L. Stormer. (2008). Ultrahigh electron mobility in suspended graphene. *Solid State Commun*, 146 (9–10), 351–355.

[35] Lee, C., X. Wei, J.W. Kysar, and J. Hone. (2008). Measurement of the elastic properties and intrinsic strength of monolayer graphene. *Science*, 321 (5887), 385–388.

[36] Lemine, A.S., M.M. Zagho, T.M. Altahtamouni, and N. Bensalah. (2018). Graphene a promising electrode material for supercapacitors—A review. *Int J Energy Res*, 42 (14), 4284–4300.

[37] Zhong, Y., X. Xia, F. Shi, J. Zhan, J. Tu, and H.J. Fan. (2016). Transition Metal Carbides and Nitrides in Energy Storage and Conversion. 3 (5), 1500286.

[38] Lukatskaya, M.R., O. Mashtalir, C.E. Ren, Y. Dall'Agnese, P. Rozier, P.L. Taberna, M. Naguib, P. Simon, M.W. Barsoum, and Y. Gogotsi. (2013). Cation Intercalation and High Volumetric Capacitance of Two-Dimensional Titanium Carbide. 341 (6153), 1502–1505.

[39] Bharti, Y. Kumar, M. Gupta, and S. Sharma. (2023). Study of pristine and functionalized V2C and Mo2C MXenes as novel electrode material for supercapacitors. *J Mol Graph Model*, 118 108366.

[40] Wu, J., J. Su, T. Wu, L. Huang, Q. Li, Y. Luo, H. Jin, J. Zhou, T. Zhai, D. Wang, Y. Gogotsi, and Y. Li. (n.d.). Scalable Synthesis of 2D Mo2C and Thickness-Dependent Hydrogen Evolution on Its Basal Plane and Edges. *Advanced Materials*, n/a (n/a), 2209954.

[41] Zhang, C., Z. Peng, C. Huang, B. Zhang, C. Xing, H. Chen, H. Cheng, J. Wang, and S. Tang. (2021). High-energy all-in-one stretchable micro-supercapacitor arrays based on 3D laser-induced graphene foams decorated with mesoporous ZnP nanosheets for self-powered stretchable systems. *Nano Energy*, 81 105609.

[42] Stretchable Micro-Supercapacitors to Self-Power Wearable Devices. https://passive-components.eu/stretchable-micro-supercapacitors-to-self-power-wearable-devices/. (Accessed: 12/25/2024).

[43] SPEL | Railway Supercapacitor, High speed train, Module, Metro, Train, Support, Lithium Ion Battery, Graphene, Supercapacitors, super capacitors, Ultracapacitors, EDLC, BMS, UPS, Back-up, Signalling. https://www.capacitorsite.com/railway.html. (Accessed: 12/25/2024).

[44] Regenerative Braking in EVs: Harnessing Energy for a Greener Drive - ElectricPe. https://electricpe.com/blogs/regenerative-braking-in-evs-harnessing-energy-for-a-greener-drive/. (Accessed: 12/25/2024).

[45] 12 Vdc UPS - DC2412-UPS - Bicker Elektronik GmbH - with supercapacitor / compact / custom. https://www.directindustry.com/prod/bicker-elektronik-gmbh/product-232966-2327413.html. (Accessed: 12/25/2024).

[46] Qu, X., Y.W. Kwon, S. Jeon, J. Jeong, W. Kang, Z. Jiang, C. Zhang, and S.W. Hong. (2023). Foldable and wearable supercapacitors for powering healthcare monitoring applications with improved performance based on hierarchically co-assembled CoO/NiCo networks. *J Colloid Interface Sci*, 634 715–729.

[47] Lu, Y., Z. Lou, K. Jiang, D. Chen, and G. Shen. (2019). Recent progress of self-powered wearable monitoring systems integrated with microsupercapacitors. *Mater Today Nano*, 8 100050.

[48] Iravani, S., and R.S. Varma. (2023). MXene-based wearable supercapacitors and their transformative impact on healthcare. *Mater Adv*, 4 (19), 4317–4332.

[49] Şahin, M.E., F. Blaabjerg, and A. Sangwongwanich. (2022). A Comprehensive Review on Supercapacitor Applications and Developments. *Energies 2022, Vol. 15, Page 674*, 15 (3), 674.

[50] Tecate Group - Ultracapacitor and Capacitor Markets. https://www.tecategroup.com/markets/?market=Military-Aerospace. (Accessed: 12/25/2024).

[51] Ke, Q., and J. Wang. (2016). Graphene-based materials for supercapacitor electrodes – A review. *Journal of Materiomics*, 2 (1), 37–54.

[52] Novoselov, K.S., A.K. Geim, S. V. Morozov, D. Jiang, Y. Zhang, S. V. Dubonos, I. V. Grigorieva, and A.A. Firsov. (2004). Electric field in atomically thin carbon films. *Science (1979)*, 306 (5696), 666–669.

[53] Stoller, M.D., C.W. Magnuson, Y. Zhu, S. Murali, J.W. Suk, R. Piner, and R.S. Ruoff. (2011). Interfacial capacitance of single layer graphene. *Energy Environ Sci*, 4 (11), 4685–4689.

[54] Xia, J., F. Chen, J. Li, and N. Tao. (2009). Measurement of the quantum capacitance of graphene. *Nature Nanotechnology 2009 4:8*, 4 (8), 505–509.

[55] Bolotin, K.I., K.J. Sikes, Z. Jiang, M. Klima, G. Fudenberg, J. Hone, P. Kim, and H.L. Stormer. (2008). Ultrahigh electron mobility in suspended graphene. *Solid State Commun*, 146 (9–10), 351–355.

[56] Lee, C., X. Wei, J.W. Kysar, and J. Hone. (2008). Measurement of the elastic properties and intrinsic strength of monolayer graphene. *Science (1979)*, 321 (5887), 385–388.

[57] Lemine, A.S., M.M. Zagho, T.M. Altahtamouni, and N. Bensalah. (2018). Graphene a promising electrode material for supercapacitors—A review. *Int J Energy Res*, 42 (14), 4284–4300.

[58] Prekodravac, J.R., D.P. Kepić, J.C. Colmenares, D.A. Giannakoudakis, and S.P. Jovanović. (2021). A comprehensive review on selected graphene synthesis methods: from electrochemical exfoliation through rapid thermal annealing towards biomass pyrolysis. *J Mater Chem C Mater*, 9 (21), 6722–6748.

[59] Gutiérrez-Cruz, A., A.R. Ruiz-Hernández, J.F. Vega-Clemente, D.G. Luna-Gazcón, and J. Campos-Delgado. (2022). A review of top-down and bottom-up synthesis methods for the production of graphene, graphene oxide and reduced graphene oxide. *Journal of Materials Science 2022 57:31*, 57 (31), 14543–14578.

[60] Mbayachi, V.B., E. Ndayiragije, T. Sammani, S. Taj, E.R. Mbuta, and A. ullah khan. (2021). Graphene synthesis, characterization and its applications: A review. *Results Chem*, 3 100163.

[61] Yi, M., and Z. Shen. (2015). A review on mechanical exfoliation for the scalable production of graphene. *J Mater Chem A Mater*, 3 (22), 11700–11715.

[62] Bhuyan, M.S.A., M.N. Uddin, M.M. Islam, F.A. Bipasha, and S.S. Hossain. (2016). Synthesis of graphene. *International Nano Letters 2016 6:2*, 6 (2), 65–83.

[63] Li, X., W. Cai, J. An, S. Kim, J. Nah, D. Yang, R. Piner, A. Velamakanni, I. Jung, E. Tutuc, S.K. Banerjee, L. Colombo, and R.S. Ruoff. (2009). Large-area synthesis of high-quality and uniform graphene films on copper foils. *Science (1979)*, 324 (5932), 1312–1314.

[64] Suk, J.W., A. Kitt, C.W. Magnuson, Y. Hao, S. Ahmed, J. An, A.K. Swan, B.B. Goldberg, and R.S. Ruoff. (2011). Transfer of CVD-grown monolayer graphene onto arbitrary substrates. *ACS Nano*, 5 (9), 6916–6924.

[65] Malard, L.M., M.A. Pimenta, G. Dresselhaus, and M.S. Dresselhaus. (2009). Raman spectroscopy in graphene. *Phys Rep*, 473 (5–6), 51–87.

[66] Malard, L.M., M.A. Pimenta, G. Dresselhaus, and M.S. Dresselhaus. (2009). Raman spectroscopy in graphene. *Phys Rep*, 473 (5–6), 51–87.

[67] Shioyama, H. (2000). The interactions of two chemical species in the interlayer spacing of graphite. *Synth Met*, 114 (1), 1–15.

[68] Novoselov, K.S., D. Jiang, F. Schedin, T.J. Booth, V. V. Khotkevich, S. V. Morozov, and A.K. Geim. (2005). Two-dimensional atomic crystals. *Proceedings of the National Academy of Sciences*, 102 (30), 10451–10453.

[69] Shioyama, H. (2000). The interactions of two chemical species in the interlayer spacing of graphite. *Synth Met*, 114 (1), 1–15.

[70] Gupta, A., G. Chen, P. Joshi, S. Tadigadapa, and P.C. Eklund. (2006). Raman scattering from high-frequency phonons in supported n-graphene layer films. *Nano Lett*, 6 (12), 2667–2673.

[71] Ferrari, A.C., J.C. Meyer, V. Scardaci, C. Casiraghi, M. Lazzeri, F. Mauri, S. Piscanec, D. Jiang, K.S. Novoselov, S. Roth, and A.K. Geim. (2006). Raman spectrum of graphene and graphene layers. *Phys Rev Lett*, 97 (18), 187401.

[72] Kumar, S., M.A. Rehman, S. Lee, M. Kim, H. Hong, J.Y. Park, and Y. Seo. (2021). Supercapacitors based on Ti3C2Tx MXene extracted from supernatant and current collectors passivated by CVD-graphene. *Scientific Reports 2021 11:1*, 11 (1), 1–9.

[73] Allagui, A., T.J. Freeborn, A.S. Elwakil, and B.J. Maundy. (2016). Reevaluation of Performance of Electric Double-layer Capacitors from Constant-current Charge/Discharge and Cyclic Voltammetry. *Scientific Reports 2016 6:1*, 6 (1), 1–8.

[74] Schoetz, T., L.W. Gordon, S. Ivanov, A. Bund, D. Mandler, and R.J. Messinger. (2022). Disentangling faradaic, pseudocapacitive, and capacitive charge storage: A tutorial for the characterization of batteries, supercapacitors, and hybrid systems. *Electrochim Acta*, 412 140072.

[75] Simon, P., and Y. Gogotsi. (2020). Perspectives for electrochemical capacitors and related devices. *Nature Materials 2020 19:11*, 19 (11), 1151–1163.

[76] Zhu, Y., S. Murali, M.D. Stoller, K.J. Ganesh, W. Cai, P.J. Ferreira, A. Pirkle, R.M. Wallace, K.A. Cychosz, M. Thommes, D. Su, E.A. Stach, and R.S. Ruoff. (2011). Carbon-based supercapacitors produced by activation of graphene. *Science (1979)*, 332 (6037), 1537–1541.

[77] El-Kady, M.F., V. Strong, S. Dubin, and R.B. Kaner. (2012). Laser scribing of high-performance and flexible graphene-based electrochemical capacitors. *Science (1979)*, 335 (6074), 1326–1330.

[78] Yang, X., C. Cheng, Y. Wang, L. Qiu, and D. Li. (2013). Liquid-mediated dense integration of graphene materials for compact capacitive energy storage. *Science (1979)*, 341 (6145), 534–537.

[79] Naguib, M., M. Kurtoglu, V. Presser, J. Lu, J. Niu, M. Heon, L. Hultman, Y. Gogotsi, and M.W. Barsoum. (2011). Two-Dimensional Nanocrystals Produced by Exfoliation of Ti3AlC2. 23 (37), 4248–4253.

[80] Naguib, M., and Y. Gogotsi. (2015). Synthesis of two-dimensional materials by selective extraction. *Acc Chem Res*, 48 (1), 128–135.

[81] Rakhi, R.B., B. Ahmed, M.N. Hedhili, D.H. Anjum, and H.N. Alshareef. (2015). Effect of Postetch Annealing Gas Composition on the Structural and Electrochemical Properties of Ti2CTx MXene Electrodes for Supercapacitor Applications. *Chemistry of Materials*, 27 (15), 5314–5323.

[82] Ghidiu, M., M.R. Lukatskaya, M.-Q. Zhao, Y. Gogotsi, and M.W. Barsoum. (2014). Conductive two-dimensional titanium carbide 'clay' with high volumetric capacitance. *Nature*, 516 (7529), 78–81.

[83] Urbankowski, P., B. Anasori, T. Makaryan, D. Er, S. Kota, P.L. Walsh, M. Zhao, V.B. Shenoy, M.W. Barsoum, and Y. Gogotsi. (2016). Synthesis of two-dimensional titanium nitride Ti4N3 (MXene). *Nanoscale*, 8 (22), 11385–11391.

[84] Yang, S., P. Zhang, F. Wang, A.G. Ricciardulli, M.R. Lohe, P.W.M. Blom, and X. Feng. (2018). Fluoride-Free Synthesis of Two-Dimensional Titanium Carbide (MXene) Using A Binary Aqueous System. *Angewandte Chemie International Edition*, 57 (47), 15491–15495.

[85] Kumar, Y.A., C.J. Raorane, H.H. Hegazy, T. Ramachandran, S.C. Kim, and M. Moniruzzaman. (2023). 2D MXene-based supercapacitors: A promising path towards high-performance energy storage. *J Energy Storage*, 72 108433.

[86] Verger, L., C. Xu, V. Natu, H.M. Cheng, W. Ren, and M.W. Barsoum. (2019). Overview of the synthesis of MXenes and other ultrathin 2D transition metal carbides and nitrides. *Curr Opin Solid State Mater Sci*, 23 (3), 149–163.

[87] Naguib, M., V.N. Mochalin, M.W. Barsoum, Y. Gogotsi, M. Naguib, V.N. Mochalin, M.W. Barsoum, and Y. Gogotsi. (2014). 25th Anniversary Article: MXenes: A New Family of Two-Dimensional Materials. *Advanced Materials*, 26 (7), 992–1005.

[88] Sokol, M., V. Natu, S. Kota, and M.W. Barsoum. (2019). On the Chemical Diversity of the MAX Phases. *Trends Chem*, 1 (2), 210–223.

[89] Kumar, K.S., N. Choudhary, Y. Jung, and J. Thomas. (2018). Recent advances in two-dimensional nanomaterials for supercapacitor electrode applications. *ACS Energy Lett*, 3 (2), 482–495.

[90] Okubo, M., A. Sugahara, S. Kajiyama, and A. Yamada. (2018). MXene as a Charge Storage Host. *Acc Chem Res*, 51 (3), 591–599.

[91] Hart, J.L., K. Hantanasirisakul, A.C. Lang, B. Anasori, D. Pinto, Y. Pivak, J.T. van Omme, S.J. May, Y. Gogotsi, and M.L. Taheri. (2019). Control of MXenes'

electronic properties through termination and intercalation. *Nature Communications 2019 10:1*, 10 (1), 1–10.

[92] Schultz, T., N.C. Frey, K. Hantanasirisakul, S. Park, S.J. May, V.B. Shenoy, Y. Gogotsi, and N. Koch. (2019). Surface Termination Dependent Work Function and Electronic Properties of Ti3C2Tx MXene. *Chemistry of Materials*, 31 (17), 6590–6597.

[93] Sinha, A., Dhanjai, H. Zhao, Y. Huang, X. Lu, J. Chen, and R. Jain. (2018). MXene: An emerging material for sensing and biosensing. *TrAC Trends in Analytical Chemistry*, 105 424–435.

[94] Liu, Z., L. Zheng, L. Sun, Y. Qian, J. Wang, and M. Li. (2014). (Cr2/3Ti1/3)3AlC2 and (Cr5/8Ti3/8)4AlC3: New MAX-phase Compounds in Ti–Cr–Al–C System. *Journal of the American Ceramic Society*, 97 (1), 67–69.

[95] Naguib, M., G.W. Bentzel, J. Shah, J. Halim, E.N. Caspi, J. Lu, L. Hultman, and M.W. Barsoum. (2014). New Solid Solution MAX Phases: (Ti0.5, V0.5)3AlC2, (Nb0.5, V0.5)2AlC, (Nb0.5, V0.5)4AlC3 and (Nb0.8, Zr0.2)2AlC. *Mater Res Lett*, 2 (4), 233–240.

[96] Xu, C., L. Wang, Z. Liu, L. Chen, J. Guo, N. Kang, X.-L. Ma, H.-M. Cheng, and W. Ren. (2015). Large-area high-quality 2D ultrathin Mo2C superconducting crystals. *Nat Mater*, 14 (11), 1135–1141.

[97] Turker, F., O.R. Caylan, N. Mehmood, T.S. Kasirga, C. Sevik, and G. Cambaz Buke. (2020). CVD synthesis and characterization of thin Mo2C crystals. *Journal of the American Ceramic Society*, 103 (10), 5586–5593.

[98] Öper, M., U. Yorulmaz, C. Sevik, F. Ay, and N.K. Perkgöz. (2022). Controlled CVD growth of ultrathin Mo2C (MXene) flakes. 131 (2), 25304.

[99] Gogotsi, Y. (2015). Transition metal carbides go 2D. *Nature Materials 2015 14:11*, 14 (11), 1079–1080.

[100] Xu, S., L. Zhang, B. Wang, and R.S. Ruoff. (2021). Chemical vapor deposition of graphene on thin-metal films. *Cell Rep Phys Sci*, 2 (3), 100372.

[101] Ibrahim, W.L., H. Şar, F. Ay, and N. Kosku Perkgöz. (2022). Enhanced performance of supercapacitors based on rotationally stacked CVD graphene. *J Appl Phys*, 131 (16),.

[102] Anasori, B., M.R. Lukatskaya, and Y. Gogotsi. (2017). 2D metal carbides and nitrides (MXenes) for energy storage. *Nature Reviews Materials 2017 2:2*, 2 (2), 1–17.

[103] Salim, O., K.A. Mahmoud, K.K. Pant, and R.K. Joshi. (2019). Introduction to MXenes: synthesis and characteristics. *Mater Today Chem*, 14 100191.

[104] Paul, J.T., A.K. Singh, Z. Dong, H. Zhuang, B.C. Revard, B. Rijal, M. Ashton, A. Linscheid, M. Blonsky, D. Gluhovic, J. Guo, and R.G. Hennig. (2017).

Computational methods for 2D materials: Discovery, property characterization, and application design. *Journal of Physics Condensed Matter*, 29 (47), 473001.

[105] Naguib, M., M. Kurtoglu, V. Presser, J. Lu, J. Niu, M. Heon, L. Hultman, Y. Gogotsi, and M.W. Barsoum. (2011). Two-Dimensional Nanocrystals Produced by Exfoliation of Ti3AlC2. *Advanced Materials*, 23 (37), 4248–4253.

[106] Anasori, B., Y. Xie, M. Beidaghi, J. Lu, B.C. Hosler, L. Hultman, P.R.C. Kent, Y. Gogotsi, and M.W. Barsoum. (2015). Two-Dimensional, Ordered, Double Transition Metals Carbides (MXenes). *ACS Nano*, 9 (10), 9507–9516.

[107] Halim, J., J. Palisaitis, J. Lu, J. Thörnberg, E.J. Moon, M. Precner, P. Eklund, P.O.A. Persson, M.W. Barsoum, and J. Rosen. (2018). Synthesis of two-dimensional nb1.33c (mxene) with randomly distributed vacancies by etching of the quaternary solid solution (nb2/3sc1/3)2alc max phase. *ACS Appl Nano Mater*, 1 (6), 2455–2460.

[108] Tao, Q., M. Dahlqvist, J. Lu, S. Kota, R. Meshkian, J. Halim, J. Palisaitis, L. Hultman, M.W. Barsoum, P.O.Å. Persson, and J. Rosen. (2017). Two-dimensional Mo1.33C MXene with divacancy ordering prepared from parent 3D laminate with in-plane chemical ordering. *Nat Commun*, 8 14949.

[109] Meshkian, R., M. Dahlqvist, J. Lu, B. Wickman, J. Halim, J. Thörnberg, Q. Tao, S. Li, S. Intikhab, J. Snyder, M.W. Barsoum, M. Yildizhan, J. Palisaitis, L. Hultman, P.O.Å. Persson, and J. Rosen. (2018). W-Based Atomic Laminates and Their 2D Derivative W1.33C MXene with Vacancy Ordering. *Advanced Materials*, 30 (21), 1706409.

[110] Ronchi, R.M., J.T. Arantes, and S.F. Santos. (2019). Synthesis, structure, properties and applications of MXenes: Current status and perspectives. *Ceram Int*, 45 (15), 18167–18188.

[111] Mu, X., D. Wang, F. Du, G. Chen, C. Wang, Y. Wei, Y. Gogotsi, Y. Gao, and Y. Dall'Agnese. (2019). Revealing the Pseudo-Intercalation Charge Storage Mechanism of MXenes in Acidic Electrolyte. 29 (29), 1902953.

[112] Liu, Y., S.P. Jiang, and Z. Shao. (2020). Intercalation pseudocapacitance in electrochemical energy storage: recent advances in fundamental understanding and materials development. *Mater Today Adv*, 7 100072.

[113] Otgonbayar, Z., S. Yang, I.J. Kim, and W.C. Oh. (2023). Recent Advances in Two-Dimensional MXene for Supercapacitor Applications: Progress, Challenges, and Perspectives. *Nanomaterials 2023, Vol. 13, Page 919*, 13 (5), 919.

[114] Li, X., Z. Huang, C.E. Shuck, G. Liang, Y. Gogotsi, and C. Zhi. (2022). MXene chemistry, electrochemistry and energy storage applications. *Nature Reviews Chemistry 2022 6:6*, 6 (6), 389–404.

[115] Khazaei, M., A. Ranjbar, M. Arai, T. Sasaki, and S. Yunoki. (2017). Electronic properties and applications of MXenes: a theoretical review. *J Mater Chem C Mater*, 5 (10), 2488–2503.

[116] Huang, K., Z. Li, J. Lin, G. Han, and P. Huang. (2018). Two-dimensional transition metal carbides and nitrides (MXenes) for biomedical applications. *Chem Soc Rev*, 47 (14), 5109–5124.

[117] Maleski, K., V.N. Mochalin, and Y. Gogotsi. (2017). Dispersions of Two-Dimensional Titanium Carbide MXene in Organic Solvents. *Chemistry of Materials*, 29 (4), 1632–1640.

[118] Dillon, A.D., M.J. Ghidiu, A.L. Krick, J. Griggs, S.J. May, Y. Gogotsi, M.W. Barsoum, and A.T. Fafarman. (2016). Highly Conductive Optical Quality Solution-Processed Films of 2D Titanium Carbide. *Adv Funct Mater*, 26 (23), 4162–4168.

[119] Verger, L., V. Natu, M. Carey, and M.W. Barsoum. (2019). MXenes: An Introduction of Their Synthesis, Select Properties, and Applications. *Trends Chem*, 1 (7), 656–669.

[120] Akhter, R., and S.S. Maktedar. (2023). MXenes: A comprehensive review of synthesis, properties, and progress in supercapacitor applications. *Journal of Materiomics*, 9 (6), 1196–1241.

[121] Li, T., W. Luo, H. Kitadai, X. Wang, and X. Ling. (2019). Probing the Domain Architecture in 2D α-Mo2C via Polarized Raman Spectroscopy. *Advanced Materials*, 31 (8), 1807160.

[122] Kang, Z., Z. Zheng, H. Wei, Z. Zhang, X. Tan, L. Xiong, T. Zhai, and Y. Gao. (2019). Controlled Growth of an Mo2C—Graphene Hybrid Film as an Electrode in Self-Powered Two-Sided Mo2C—Graphene/Sb2S0.42Se2.58/TiO2 Photodetectors. *Sensors*, 19 (5), 1099.

[123] Dresselhaus, M.S., G. Dresselhaus, and A. Jorio. (2007). *Group theory: application to the physics of condensed matter*. Springer Science & Business Media .

[124] Caylan, O.R., and G. Cambaz Buke. (2021). Low-temperature synthesis and growth model of thin Mo2C crystals on indium. *Sci Rep*, 11 (1), 8247.

[125] Geng, D., X. Zhao, L. Li, P. Song, B. Tian, W. Liu, J. Chen, D. Shi, M. Lin, W. Zhou, and K.P. Loh. (2016). Controlled growth of ultrathin Mo 2 C superconducting crystals on liquid Cu surface. *2d Mater*, 4 (1), 11012.

[126] Kumar, S., M.A. Rehman, S. Lee, M. Kim, H. Hong, J.-Y. Park, and Y. Seo. (2021). Supercapacitors based on Ti3C2Tx MXene extracted from supernatant and current collectors passivated by CVD-graphene. *Sci Rep*, 11 (1), 649.

[127] Allagui, A., T.J. Freeborn, A.S. Elwakil, and B.J. Maundy. (2016). Reevaluation of performance of electric double-layer capacitors from constant-current charge/discharge and cyclic voltammetry. *Sci Rep*, 6 (1), 1–8.

[128] Huang, X. (2011). Separator technologies for lithium-ion batteries. *Journal of Solid State Electrochemistry*, 15 (4), 649–662.

[129] Zhao, C., J. Niu, C. Xiao, Z. Qin, X. Jin, W. Wang, and Z. Zhu. (2022). Separator with high ionic conductivity and good stability prepared from keratin fibers for supercapacitor applications. *Chemical Engineering Journal*, 444 136537.

[130] Sun, X.Z., X. Zhang, B. Huang, and Y.W. Ma. (2014). Effects of Separator on the Electrochemical Performance of Electrical Double-Layer Capacitor and Hybrid Battery-Supercapacitor. *Wuli Huaxue Xuebao/ Acta Physico - Chimica Sinica*, 30 (3), 485–491.

[131] Poonam, K. Sharma, A. Arora, and S.K. Tripathi. (2019). Review of supercapacitors: Materials and devices. *J Energy Storage*, 21 801–825.

[132] Raza, W., F. Ali, N. Raza, Y. Luo, K.-H. Kim, J. Yang, S. Kumar, A. Mehmood, and E.E. Kwon. (2018). Recent advancements in supercapacitor technology. *Nano Energy*, 52 441–473.

[133] Şahin, M.E., F. Blaabjerg, and A. Sangwongwanich. (2022). A Comprehensive Review on Supercapacitor Applications and Developments. *Energies (Basel)*, 15 (3), 674.

[134] Musolino, V., E. Tironi, and P. di Milano. A comparison of supercapacitor and high-power lithium batteries, in: Electrical Systems for Aircraft, Railway and Ship Propulsion, : pp. 1–6.

[135] Wang, F., C. Yang, M. Duan, Y. Tang, and J. Zhu. (2015). TiO2 nanoparticle modified organ-like Ti3C2 MXene nanocomposite encapsulating hemoglobin for a mediator-free biosensor with excellent performances. *Biosens Bioelectron*, 74 1022–1028.

[136] Naguib, M., O. Mashtalir, J. Carle, V. Presser, J. Lu, L. Hultman, Y. Gogotsi, and M.W. Barsoum. (2012). Two-Dimensional Transition Metal Carbides. *ACS Nano*, 6 (2), 1322–1331.

[137] Mashtalir, O., M. Naguib, V.N. Mochalin, Y. Dall'Agnese, M. Heon, M.W. Barsoum, and Y. Gogotsi. (2013). Intercalation and delamination of layered carbides and carbonitrides. *Nat Commun*, 4.

[138] Aravind, A.M., M. Tomy, A. Kuttapan, A.M. Kakkassery Aippunny, and X.T. Suryabai. (2023). Progress of 2D MXene as an Electrode Architecture for Advanced Supercapacitors: A Comprehensive Review. *ACS Omega*,.

[139] Hu, M., H. Zhang, T. Hu, B. Fan, X. Wang, and Z. Li. (2020). Emerging 2D MXenes for supercapacitors: status, challenges and prospects. *Chem Soc Rev*, 49 (18), 6666–6693.

[140] Li, J., X. Yuan, C. Lin, Y. Yang, L. Xu, X. Du, J. Xie, J. Lin, and J. Sun. (2017). Achieving high pseudocapacitance of 2D titanium carbide (MXene) by cation intercalation and surface modification. *Adv Energy Mater*, 7 (15), 1602725.

[141] Yamada, H., K. Yoshii, M. Asahi, M. Chiku, and Y. Kitazumi. (2022). Cyclic Voltammetry Part 2: Surface Adsorption, Electric Double Layer, and Diffusion Layer. *Electrochemistry*, 90 (10), 102006.

[142] Azman, N.H.N., M.S. Mamat @ Mat Nazir, L.H. Ngee, and Y. Sulaiman. (2018). Graphene-based ternary composites for supercapacitors. *Int J Energy Res*, 42 (6), 2104–2116.

[143] Zhang, J., Z. Li, C. Zhang, B. Feng, Z. Zhou, and H. Liu. (2012). Graphite-Coated Paper as Substrate for High Sensitivity Analysis in Ambient Surface-Assisted Laser Desorption/Ionization Mass Spectrometry. *Anal Chem*, 84 3296–3301.

[144] Zhao, Y., Z. Zhang, Y. Ren, W. Ran, X. Chen, J. Wu, and F. Gao. (2015). Vapor deposition polymerization of aniline on 3D hierarchical porous carbon with enhanced cycling stability as supercapacitor electrode. *J Power Sources*, 286 1–9.

[145] Jyothibasu, J.P., D.-W. Kuo, and R.-H. Lee. (2019). Flexible and freestanding electrodes based on polypyrrole/carbon nanotube/cellulose composites for supercapacitor application. *Cellulose*, 26 (7), 4495–4513.

[146] Liu, T. Ph.D. Dissertation: Exploration of Carbonaceous Materials for Supercapacitors, 2017.

[147] Mariappan, V.K., K. Krishnamoorthy, P. Pazhamalai, S. Sahoo, and S.-J. Kim. (2018). Electrodeposited molybdenum selenide sheets on nickel foam as a binder-free electrode for supercapacitor application. *Electrochim Acta*, 265 514–522.

[148] Laschuk, N.O., E.B. Easton, and O. V Zenkina. (2021). Reducing the resistance for the use of electrochemical impedance spectroscopy analysis in materials chemistry. *RSC Adv*, 11 (45), 27925–27936.

[149] Nkosi, D., J. Pillay, K.I. Ozoemena, K. Nouneh, and M. Oyama. (2010). Heterogeneous electron transfer kinetics and electrocatalytic behaviour of mixed self-assembled ferrocenes and SWCNT layers. *Physical Chemistry Chemical Physics*, 12 (3), 604–613.

[150] Simi, V.S., and N. Rajendran. (2017). Influence of tunable diameter on the electrochemical behavior and antibacterial activity of titania nanotube arrays for biomedical applications. *Mater Charact*, 129 67–79.

[151] Schoetz, T., L.W. Gordon, S. Ivanov, A. Bund, D. Mandler, and R.J. Messinger. (2022). Disentangling faradaic, pseudocapacitive, and capacitive charge storage: A tutorial for the characterization of batteries, supercapacitors, and hybrid systems. *Electrochim Acta*, 412 140072.

[152] Wang, J., J. Polleux, J. Lim, and B. Dunn. (2007). Pseudocapacitive contributions to electrochemical energy storage in TiO 2 (anatase) nanoparticles. *Journal of Physical Chemistry C*, 111 (40), 14925–14931.

[153] Pholauyphon, W., P. Charoen-amornkitt, T. Suzuki, and S. Tsushima. (2024). Perspectives on accurately analyzing cyclic voltammograms for surface- and diffusion-controlled contributions. *Electrochem Commun*, 159 107654.

[154] Ardizzone, S., G. Fregonara, and S. Trasatti. (1990). "Inner" and "outer" active surface of RuO2 electrodes. *Electrochim Acta*, 35 (1), 263–267.

[155] Deviprasath, C., K. Pandi, S.-M. Chen, H.-J. Kim, and P. Kandasamy. (2019). Metal-Free Multi-Porous Carbon for Electrochemical energy storage and Electrocatalysis Applications. *New Journal of Chemistry*, 43.

[156] Manjakkal, L., E. Djurdjic, K. Cvejin, J. Kulawik, K. Zaraska, and D. Szwagierczak. (2015). Electrochemical Impedance Spectroscopic Analysis of RuO2 Based Thick Film pH Sensors. *Electrochim Acta*, 168 246–255.

[157] Shan, Q., X. Mu, M. Alhabeb, C.E. Shuck, D. Pang, X. Zhao, X.-F. Chu, Y. Wei, F. Du, and G. Chen. (2018). Two-dimensional vanadium carbide (V2C) MXene as electrode for supercapacitors with aqueous electrolytes. *Electrochem Commun*, 96 103–107.

[158] Tao, Q., M. Dahlqvist, J. Lu, S. Kota, R. Meshkian, J. Halim, J. Palisaitis, L. Hultman, M.W. Barsoum, and P.O.Å. Persson. (2017). Two-dimensional Mo1. 33C MXene with divacancy ordering prepared from parent 3D laminate with in-plane chemical ordering. *Nat Commun*, 8 (1), 14949.

[159] Brandt, A., S. Pohlmann, A. Varzi, A. Balducci, and S. Passerini. (2013). Ionic liquids in supercapacitors. *MRS Bull*, 38 (7), 554–559.

[160] Eftekhari, A. (2017). Supercapacitors utilising ionic liquids. *Energy Storage Mater*, 9 47–69.

[161] Johnson, K.E. (2007). What's an ionic liquid? *Electrochemical Society Interface*, 16 (1), 38–41.

[162] Balducci, A., R. Dugas, P.L. Taberna, P. Simon, D. Plée, M. Mastragostino, and S. Passerini. (2007). High temperature carbon–carbon supercapacitor using ionic liquid as electrolyte. *J Power Sources*, 165 (2), 922–927.

[163] Zhang, S., S. Brahim, and S. Maat. (2018). High-voltage operation of binder-free CNT supercapacitors using ionic liquid electrolytes. *J Mater Res*, 33 (9), 1179–1188.

[164] Sugizaki, T., N. Takami, and K. Hoshina. (2023). Triethyl sulfonium bis(trifluoromethylsulfonyl)imide ionic liquids with highly concentrated LiFSI as electrolytes for Li metal batteries. *J Power Sources*, 571 233024.

[165] Şahin, M.E., F. Blaabjerg, and A. Sangwongwanich. (2022). A Comprehensive Review on Supercapacitor Applications and Developments. *Energies 2022, Vol. 15, Page 674*, 15 (3), 674.

[166] Kumar, Y.A., N. Roy, T. Ramachandran, M. Hussien, M. Moniruzzaman, and S.W. Joo. (2024). Shaping the future of energy: The rise of supercapacitors progress in the last five years. *J Energy Storage*, 98 113040.

[167] Dissanayake, K., and D. Kularatna-Abeywardana. (2024). A review of supercapacitors: Materials, technology, challenges, and renewable energy applications. *J Energy Storage*, 96 112563.

[168] Panda, S., K. Deshmukh, S.K. Khadheer Pasha, J. Theerthagiri, S. Manickam, and M.Y. Choi. (2022). MXene based emerging materials for supercapacitor applications: Recent advances, challenges, and future perspectives. *Coord Chem Rev*, 462 214518.

[169] Jayakumar, S., P.C. Santhosh, S. Ramakrishna, and A. V. Radhamani. (2024). 2D (Ti3C2Tx) MXene: A comprehensive review of advancements in synthesis protocols, applications in supercapacitors, sustainability targets and future prospects. *J Energy Storage*, 97 112741.

[170] Nidhi, N. Tyagi, V. Bhardwaj, S. Moka, M.K. Singh, M. Khanuja, and G. Sharma. (2024). An overview on synthesis of MXene and MXene based nanocomposites for supercapacitors. *Mater Today Commun*, 41 110223.

[171] Singh, U.K., H. Kaur, P. Kaur, and R. Rastogi. (2024). Unlocking potential: Recent advances in MXene supercapacitors for flexible energy storage devices. *Nano-Structures & Nano-Objects*, 39 101290.

[172] Saha, M., A. Kumar, R. Kanaoujiya, K. Behera, and S. Trivedi. (2024). A Comprehensive Review of Novel Emerging Electrolytes for Supercapacitors: Aqueous and Organic Electrolytes Versus Ionic Liquid-Based Electrolytes. *Energy and Fuels*, 38 (10), 8528–8552.

[173] Choudhary, G., J. Dhariwal, M. Saha, S. Trivedi, M.K. Banjare, R. Kanaoujiya, and K. Behera. (2024). Ionic liquids: environmentally sustainable materials for energy conversion and storage applications. *Environmental Science and Pollution Research*, 31 (7), 10296–10316.

[174] Brandt, A., S. Pohlmann, A. Varzi, A. Balducci, and S. Passerini. (2013). Ionic liquids in supercapacitors. *MRS Bull*, 38 (7), 554–559.

[175] Lin, Z., D. Barbara, P.L. Taberna, K.L. Van Aken, B. Anasori, Y. Gogotsi, and P. Simon. (2016). Capacitance of Ti3C2Tx MXene in ionic liquid electrolyte. *J Power Sources*, 326 575–579.

[176] Sun, L., L. Chai, L. Jing, Y. Chen, K. Zhuo, and J. Wang. (2024). 2,6-Diaminoanthraquinone modified MXene (Ti3C2Tx)/graphene as the negative electrode materials for ionic liquid-based asymmetric supercapacitors. *Green Energy & Environment*,.

[177] Osti, N.C., K. Liang, K. Prenger, B.P. Thapaliya, M. Tyagi, S. Dai, M. Naguib, and E. Mamontov. (2024). Optimizing protic ionic liquid electrolyte for pre-intercalated Ti3C2Tx MXene supercapacitor electrodes. *APL Energy*, 2 (4),.

[178] Gandla, D., F. Zhang, and D.Q. Tan. (2022). Advantage of Larger Interlayer Spacing of a Mo2Ti2C3 MXene Free-Standing Film Electrode toward an Excellent Performance Supercapacitor in a Binary Ionic Liquid-Organic Electrolyte. *ACS Omega*, 7 (8), 7190–7198.

[179] Hayek, A. El, P. Venet, R. Mitova, M.-X. Wang, G. Clerc, and A. Sari. (2018). Aging laws of electrolytic capacitors. 16–17.

[180] Harada, K., A. Katsuki, and M. Fujiwara. (1993). Use of ESR for Deterioration Diagnosis of Electrolytic Capacitor. *IEEE Trans Power Electron*, 8 (4), 355–361.

[181] Andrade, J.M. (2019). Electrolytic capacitor degradation monitoring using an on-line parameter estimation scheme involving sliding mode differentiators and a kalman filter. *2019 21st European Conference on Power Electronics and Applications, EPE 2019 ECCE Europe*,.

[182] Pohl, M., I. Tallo, A. Jänes, T. Romann, and E. Lust. (2018). Increasing the stability of very high potential electrical double layer capacitors by operando passivation. *J Power Sources*, 402 53–61.

[183] Jiang, X., X. Wu, Y. Xie, Z. Wang, J. Huang, Y. Qu, D. Mu, X. Zhang, W. Yang, and H. Zhang. (2023). Additive Engineering Enables Ionic-Liquid Electrolyte-Based Supercapacitors To Deliver Simultaneously High Energy and Power Density. *ACS Sustain Chem Eng*, 11 (14), 5685–5695.

[184] Gibertini, E., F. Lissandrello, L. Bertoli, P. Viviani, and L. Magagnin. (2023). All-Inkjet-Printed Ti3C2 MXene Capacitor for Textile Energy Storage. *Coatings*, 13 (2), 230.

[185] Shamsuri, N.A., M.H. Hamsan, M.F. Shukur, Y. Alias, S.N.A. Halim, S.B. Aziz, A.H. Jahidin, M. Sulaiman, L. Yuwana, S.O.J. Siong, N.M. Sarih, and M.F.Z. Kadir. (2024). Enhancing EDLC applications with [BMIM]BF4-integrated cellulose gel electrolyte for sustainable energy storage. *J Energy Storage*, 75 109559.

[186] Yu, L., L. Hu, B. Anasori, Y.T. Liu, Q. Zhu, P. Zhang, Y. Gogotsi, and B. Xu. (2018). MXene-Bonded Activated Carbon as a Flexible Electrode for High-Performance Supercapacitors. *ACS Energy Lett*, 3 (7), 1597–1603.

[187] Li, Z., L. Wang, X. Huang, and X. He. (2024). Lithium Bis(Trifluoromethanesulfonyl)Imide (LiTFSI): A Prominent Lithium Salt in Lithium-Ion Battery Electrolytes – Fundamentals, Progress, and Future Perspectives. *Adv Funct Mater*, 34 (48), 2408319.

[188] Zhang, H., C. Shen, Y. Huang, and Z. Liu. (2021). Spontaneously formation of SEI layers on lithium metal from LiFSI/DME and LiTFSI/DME electrolytes. *Appl Surf Sci*, 537 147983.

[189] Núñez-Rojas, E., I. González, G. Guzmán-González, and J. Alejandre. (2023). Molecular dynamics simulations for liquid electrolytes of propylene carbonate with LiTFSI, LiPF6, and LiBF4 salts. *J Mol Liq*, 390 122983.

[190] Weeks, J.A., J.N. Burrow, J. Diao, A.G. Paul-Orecchio, H.S. Srinivasan, R.R. Vaidyula, A. Dolocan, G. Henkelman, and C.B. Mullins. (2024). In Situ Engineering of Inorganic-Rich Solid Electrolyte Interphases via Anion Choice Enables Stable, Lithium Anodes. *Advanced Materials*, 36 (9), 2305645.

[191] Xu, Q., X. Lai, G. Zhang, T. Li, and Y. Qiu. (2024). Tailoring the passivation layer on lithium metal anode and aluminum collector by regulating the solvation structure to enhance the long-term cycling of lithium metal batteries. *Chemical Engineering Journal*, 480 148021.

[192] Yen, C.H., A.R. Neale, J. Lim, D. Bresser, L.J. Hardwick, and C.C. Hu. (2022). Corrosion suppression of aluminium current collectors within Li-ion cells using 3-methoxypropionitrile-based electrolytes. *Electrochim Acta*, 431 141105.

[193] Suo, L., O. Borodin, T. Gao, M. Olguin, J. Ho, X. Fan, C. Luo, C. Wang, and K. Xu. (2015). "Water-in-salt" electrolyte enables high-voltage aqueous lithium-ion chemistries. *Science (1979)*, 350 (6263), 938–943.

[194] Zhang, M., Y. Li, and Z. Shen. (2019). "Water-in-salt" electrolyte enhanced high voltage aqueous supercapacitor with all-pseudocapacitive metal-oxide electrodes. *J Power Sources*, 414 479–485.

[195] Yu, M., Y. Lu, H. Zheng, and X. Lu. (2018). New Insights into the Operating Voltage of Aqueous Supercapacitors. *Chemistry – A European Journal*, 24 (15), 3639–3649.

CURRICULUM VITAE

ORCID ID: 0000-0001-5823-6487

Name Surname : Ibrahim Wonge Lisheshar

Foreign Language : English, French, Turkish

Education and Professional Background:

- 2025, PhD, Eskisehir Technical University, Institute of graduate programs, Department of Electrical and electronic engineering
- 2020, Masters, Eskisehir Technical University, Institute of graduate programs, Department of Electrical and electronic engineering

Publications and/or Scientific/Artistic Activities:

- Lisheshar, I.W., S. Rouhi, F. Ay, and N. Kosku Perkgöz, (2024) "High-Performance Supercapacitors Based on Nonfunctionalized Mxenes," Journal of Power Sources, 628, 235894.
- Sar, H., N. Taghipour, I.W. Lisheshar, S. Delikanli, M. Demirtaş, H.V. Demir, F. Ay, and N. Kosku Perkgöz, (2020), "Mos2 Phototransistor Sensitized by Colloidal Semiconductor Quantum Wells," Advanced Optical Materials, 8, 2001198.
- Ibrahim, W.L., H. Şar, F. Ay, and N. Kosku Perkgöz, (2022), "Enhanced Performance of Supercapacitors Based on Rotationally Stacked Cvd Graphene," Journal of Applied Physics, 131.
- Ibrahim, W.L., M. Öper, H. Şar, F. Ay, and N.K. Perkgöz, (2022), "Evolution of Raman and Photoluminescence Spectral Characteristics of Monolayer Cvd-Mos2 over a Wide Temperature Range," Vibrational Spectroscopy, 123, 103443.
- Esen, M.Y., W.L. Ibrahim, M. Nacar, A. Kayahan, F. Ay, and N. Kosku Perkgoz, (2024), "Exploring Channel Length Effects in 2d Mos2-Based Memtransistors and Their Synaptic Behavior," Materials Science in Semiconductor Processing, 179, 108490.
- Bay, M., F. Dirisağlık, S. Çınal, S. Rouhi, I.W. Lisheshar, S.B. Ay, N.K. Perkgöz, and F. Ay, (2025), "Borophene Growth Via Chemical Vapor Deposition for Supercapacitor Applications," New Journal of Chemistry, 49, 464-474.